Cleveland State University
EngagedScholarship@CSU

ETD Archive

2011

Fabrication and Testing of a Nonstandard Thin-Film Heat Flux Sensor for Power System Applications

Scott D. Wilson
Cleveland State University

Follow this and additional works at: https://engagedscholarship.csuohio.edu/etdarchive

 Part of the Mechanical Engineering Commons

How does access to this work benefit you? Let us know!

Recommended Citation

Wilson, Scott D., "Fabrication and Testing of a Nonstandard Thin-Film Heat Flux Sensor for Power System Applications" (2011). *ETD Archive*. 488.
https://engagedscholarship.csuohio.edu/etdarchive/488

This Thesis is brought to you for free and open access by EngagedScholarship@CSU. It has been accepted for inclusion in ETD Archive by an authorized administrator of EngagedScholarship@CSU. For more information, please contact library.es@csuohio.edu.

FABRICATION AND TESTING OF A NONSTANDARD THIN-FILM HEAT FLUX SENSOR FOR POWER SYSTEM APPLICATIONS

SCOTT D. WILSON

Bachelor of Mechanical Engineering

Cleveland State University

May 2003

submitted in partial fulfillment of requirements for the degree

MASTER OF SCIENCE IN MECHANICAL ENGINEERING

at the

CLEVELAND STATE UNIVERSITY

December 2011

This thesis has been approved

for the Department of MECHANICAL ENGINEERING

and the College of Graduate Studies by

Thesis Committee Chairperson, Dr. Mounir B. Ibrahim

Department/Date

Dr. Asuquo B. Ebiana

Department/Date

Dr. Ralph J. Volino

Department/Date

United States Naval Academy

Dr. Roy C. Tew

Department/Date

ACKNOWLEDGEMENT

I thank my amazing wife, Viviana, for making this possible. Without her, I would not have been able to make it through (or eat). I also thank Helina and Everett for being my favorite kids. They will be happy to learn later that we don't go to school forever.

Special thanks to Dr. Mounir Ibrahim for keeping me in mind many years ago (almost a decade) when suggesting that I think about doing my senior design project on something called a Stirling engine. He has been exceptionally patient with my progress. Also, thanks to Dr. Roy Tew for tutoring me in all things Stirling over the years.

Thanks to Gus Fralick, John Wrbanek, & Chuck Blaha for persevering in their quest to find the right formula for adequate film adhesion and wire connections. Also, thanks to Ali Sayir and Tom Sabo for working so hard on getting ceramic disks fabricated within schedule. Thanks to Art Atherton, Terrell Jansen, and Nissim Lugasy who all helped perform key tasks enabling successful implementation.

Thanks to Jeff Schreiber who envisioned how this sensor might work, who made me believe I could eventually provide a measurement of heat flux, and who continually urged me to perform this work in a timely manner by repeating, "Don't make this a thesis project."

This work is funded through the National Aeronautics and Space Administration (NASA) Science Mission Directorate and was supported by the NASA Glenn Research Center. Any opinions, findings, and conclusions or recommendations expressed in this document are those of the author and do not necessarily reflect the views of the NASA.

FABRICATION AND TESTING OF A NONSTANDARD THIN-FILM HEAT FLUX SENSOR FOR POWER SYSTEM APPLICATIONS

ABSTRACT

Stirling convertors are being operated by NASA Glenn Research Center for many years to demonstrate a Radioisotope Power System (RPS) capable of providing reliable power for potential multi-year space missions. Techniques used to monitor Stirling convertors for change in performance include measurements of temperature, pressure, energy addition, and power output. It is difficult to measure energy addition to Stirling convertors due to the complex geometries of the hot components, temperature limits of sensor materials, and invasive integration of sensors. A thin-film heat flux sensor was used to directly measure heat energy addition to a Stirling convertor. The one micron thick, Gold vs. Platinum thermocouples were designed to make a noninvasive temperature measurement on the surface of an Alumina ceramic disk located between the heat source and Stirling convertor. Fabrication techniques included creation of ceramic substrates, which hold the thermocouples, using the slipcasting technique and creation of the thin metallic film thermocouples using Physical Vapor Deposition (PVD).

The effort succeeded in designing and fabricating unique sensors which, for the first time, were integrated into a Stirling convertor ground test and exposed to test temperatures exceeding 700 °C in air for 10,000 hours. The heat transfer measurements are discussed. Also, the sensors were examined after being removed when the test was completed.

TABLE OF CONTENTS

LIST OF FIGURES

LIST OF TABLES

Table Page

NOMENCLATURE

Alumina	Aluminum Oxide
ASC	Advanced Stirling Convertor
ASC-E	Advanced Stirling Convertor Engineering Unit
ASC-E2	Advanced Stirling Convertor Engineering Unit, 2nd generation
Au vs. Pt	Gold Verses Platinum
CAD	Computer-Aided Design
DAS	Data acquisition system
emf	Electromotive Force
FEA	Finite Element Analysis
FEM	Finite Element Model
GRC	Glenn Research Center
LabVIEW	Commercially available data acquisition software
Pt	Platinum
PVD	Physical Vapor Deposition
Pt-13% Rh	Platinum–Rhodium Alloy containing 13% Rhodium
Pt vs. Pd	Platinum Verses Palladium
RTD	Resistance-Temperature Detector

CHAPTER I

INTRODUCTION

Stirling convertors are being operated by NASA Glenn Research Center for many years to demonstrate a Radioisotope Power System (RPS) capable of providing reliable power for potential multi-year space missions. Techniques used to monitor Stirling convertors for change in performance include measurements of temperature, pressure, energy addition, and power output.[1,2,3] It is difficult to directly measure energy addition to Stirling convertors due to the complex geometries of the hot components, temperature limits of sensor materials, and invasive implementation. A heat flux sensor was conceptualized to directly measure heat energy addition from the electric heat sources, used in in-air ground tests, to a Stirling convertor. Figure 1 depicts a Stirling convertor inside an insulation enclosure typically used in Stirling applications. The heat flow is shown with red arrows and the indicated power generated by the pressure wave acting on

the piston is shown in the green arrow. Not shown is the electrical power output from the alternator or alternator losses which are usually 8 to 9 % of the indicated power.

The insulation is designed to minimize heat lost from the heat source to the environment and, therefore, maximize the amount of heat reaching the convertor. For most in-air ground tests, from 20 to 30% of the electric heat is lost through the insulation package and the remaining heat energy is absorbed by the convertor. Not shown, is the small fraction of the gross heat input, usually from 1 to 2%, that is lost back out of the heater head to the insulation after it has been absorbed by the Stirling heat collector. To quantify net heat input to the Stirling convertor, that small amount of heat energy must be determined either experimentally or analytically, but was not in scope for this task.

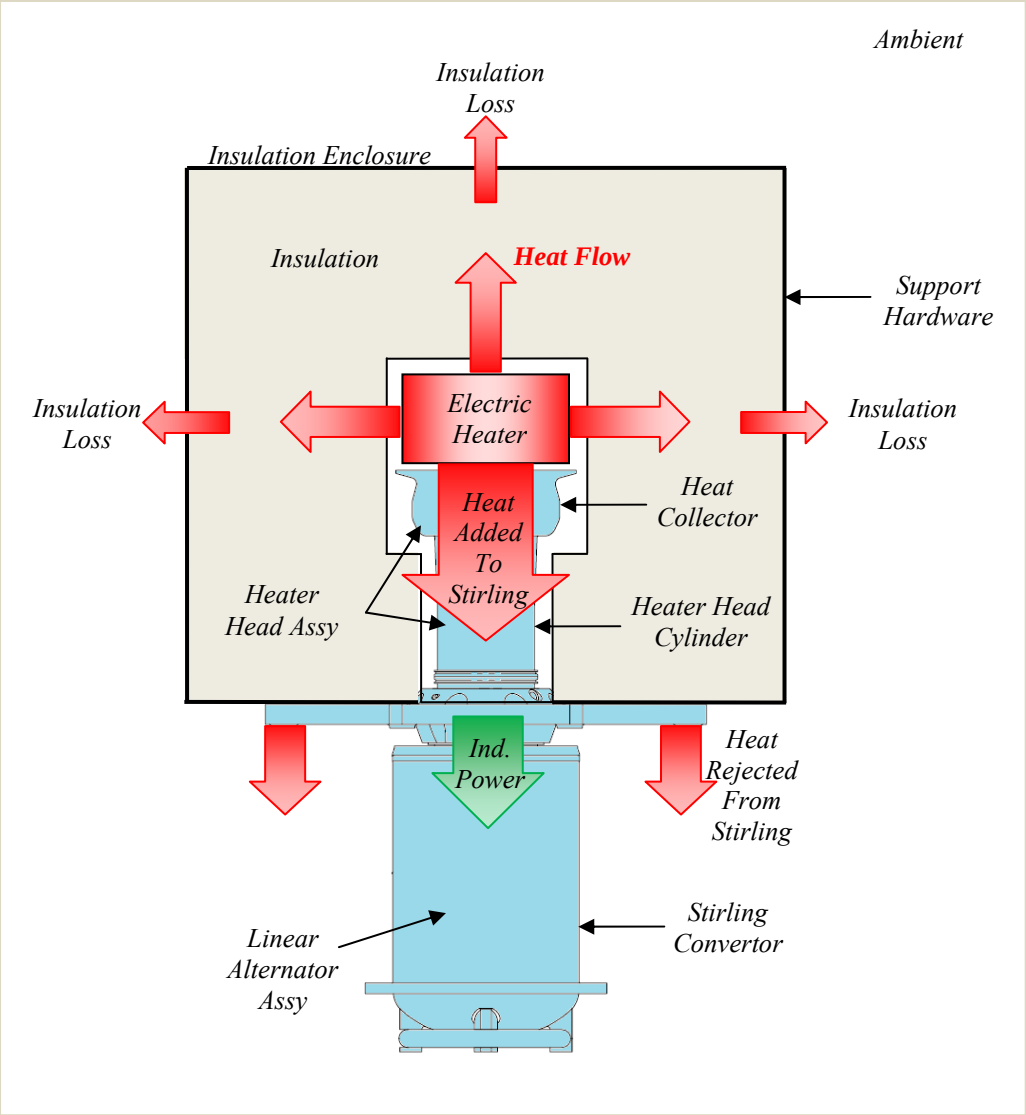

Figure 1. Description of Stirling Convertor Test Setup and Heat Flow.

This effort focused on enabling direct measurement of heat energy into the heat collector plate of the Stirling convertor heater head. Design requirements included sensor implementation without significantly diminishing available margin in heat source temperature limit or life and in a way that did not prevent the convertor from operating as expected. To make a noninvasive heat flux measurement between the heat source and Stirling convertor, a temperature difference and a way to measure it was needed. The

proposed solution was to measure the surface temperature on each side of a solid disk, located between the heat source and Stirling convertor. The disk needed to introduce a thermal resistance, imposing a temperature drop from the heat source to the heat collector.

The sensor design included thin-film thermocouples adhered to a ceramic substrate intended to be robust enough to carry the application load and survive thermally induced stresses from temperature transients during start up and shutdown, and impose the desired temperature drop to make such a measurement possible. Fabrication techniques included creation of ceramic substrates using the slipcasting technique and creation of the thin metallic film thermocouples using Physical Vapor Deposition (PVD). The effort succeeded in designing and fabricating unique sensors which, for the first time, were integrated into a Stirling convertor ground test.

1.1 Background

Heat flux sensors are devices that measure the amount of heat energy transferred through a finite thickness. This can be achieved by measuring the temperature difference across that finite thickness using thermocouples, which generates an electrical signal that is proportional to temperature. Heat flux sensors have been used in numerous areas, including industrial and engineering applications, building heating and cooling assessments, physics and medical studies, agriculture and others. Commercially available heat flux sensors are typically available for operating temperatures below 500 °C. Some products, marketed as “high-temperature” heat flux sensors, can operate above 800 °C but are generally produced in shapes and sizes suitable for particular large scale industrial applications. For aeronautics and aerospace harsh environment applications, thin films

have been deposited on complex geometries such as turbo pump and fan blades and engine injector valves.[4]

There are various designs of heat flux sensors, such as Gardon gauges, plug gauges, and thin film thermocouple arrays.[5,6,7] The thin film types have the advantage of high frequency response and minimal flow and thermal disturbance.[8] All heat flux sensors operate by measuring the temperature difference across a thermal resistance, based on Fourier's law of heat conduction, or just Fourier's Law, seen in Eq. (1).

$$Q = -k\frac{\partial T}{\partial x} \tag{1}$$

The heat flux (Q) is in W/m^2, thermal conductivity (k) is in W/(m-°C), and the temperature gradient across a given distance ($\partial T/\partial x$) is in °C/m. In practice, Eq. (1) is implemented by measuring the finite temperature difference (ΔT) across a thermal resistance of the finite thickness (Δx). The practical use of Fourier's Law is shown in Eq. (2), where the heat flux (Q) has been converted to heat flow (q) by moving the heat transfer area (A) to the right hand side.

$$q \approx -k * A * \frac{\Delta T}{\Delta x} \tag{2}$$

The temperature difference can be measured by thermocouples or a Resistance-Temperature Detector (RTD) arranged as a Wheatstone bridge.[9] In any case, it is desirable that the temperature sensors themselves be in as good thermal contact as possible with the substrate, and at the same time not interfere with the transfer.

1.2 Stirling Application

The sensors were planned for use in testing the Advanced Stirling Convertor Engineering Unit (ASC-E) serial numbers #1 and #4.[10] The convertors were planned for extended operation testing used to accumulate hours of operation for life and reliability purposes. The test setup is shown in Figure 2 along with the author. Each Stirling laboratory test setup is supported using an electronics rack which records performance data, enables fault protection against anomalous operation, and provides control over the convertor operating parameters such as temperatures, operating frequency, and piston stoke. The white boxes, shown in Figure 2, house the insulation, the hot end of the convertor, and electric heater. One heat flux sensor is installed in each white box.

Figure 2. Test Setup for Advanced Stirling Convertor Engineering Unit (ASC-E).

Historically, heat addition to the Stirling convertor has been quantified during operation by reducing static test data into a form that can be used during dynamic testing. A new method for measuring dynamic heat transfer was desired in Stirling tests that could quantify heat flux during thermal transients, is insensitive to changes in the test setup, and unaffected by modeling errors. Changes in test setup can be caused by aging insulation during long duration testing. Such changes in insulation thermophysical properties make it difficult to distinguish between slow drift in a convertor's operating point and a slow degradation in the convertor's performance. Modeling errors are possible when assumptions made for an initial test condition do not necessarily apply to a final test configuration, as is the case with the static assumptions applied to a dynamic condition. Model validation is necessary when such possibility exist. Direct measurement of heat addition to the Stirling was desired to provide a higher confidence to the value for heat input to the Stirling convertor.

CHAPTER II

DESIGN & FABRICATION

The heat flux sensor is fabricated by depositing micro layers of noble metals onto a ceramic substrate. The substrates are casted by curing a slurry then machining the final dimensions. The disks are then characterized by measuring the thermal conductivity. The thin-film thermocouples are deposited onto the ceramic disks in a pattern designed for a particular application. Wires are attached to the thin-film thermocouple patterns and the electromotive force (*emf*) voltage generated by the two dissimilar metals of the thermocouple is measured across the wires. The emf voltage increases with temperature in a very predictable and repeatable manner. In most cases, the noble metal wires coming from the thin-films need to transition to a less expensive, more durable wire used to interface the data acquisition system. This transition contains what is commonly referred to as the cold junction, the location where the noble metal wires are soldered to the

extension wire. The cold junction represents an additional offset of junction emf voltage, which must be accounted for in the final calculation of junction temperature. After cold junction compensation is performed, the hot junction temperature can be determined.

The heat energy enters the Stirling test setup through electric resistance heaters located in a nickel block. This assembly is referred to as the heat source assembly, or just the heat source. The nickel block, shown in Figure 3, shows the position of the (6x) resistance cartridge heaters. The thermocouple pattern was designed to measure three radial temperature locations under a heater and between heaters. Figure 4 shows the heater locations superimposed over the thermocouple pattern eventually chosen in the final design.

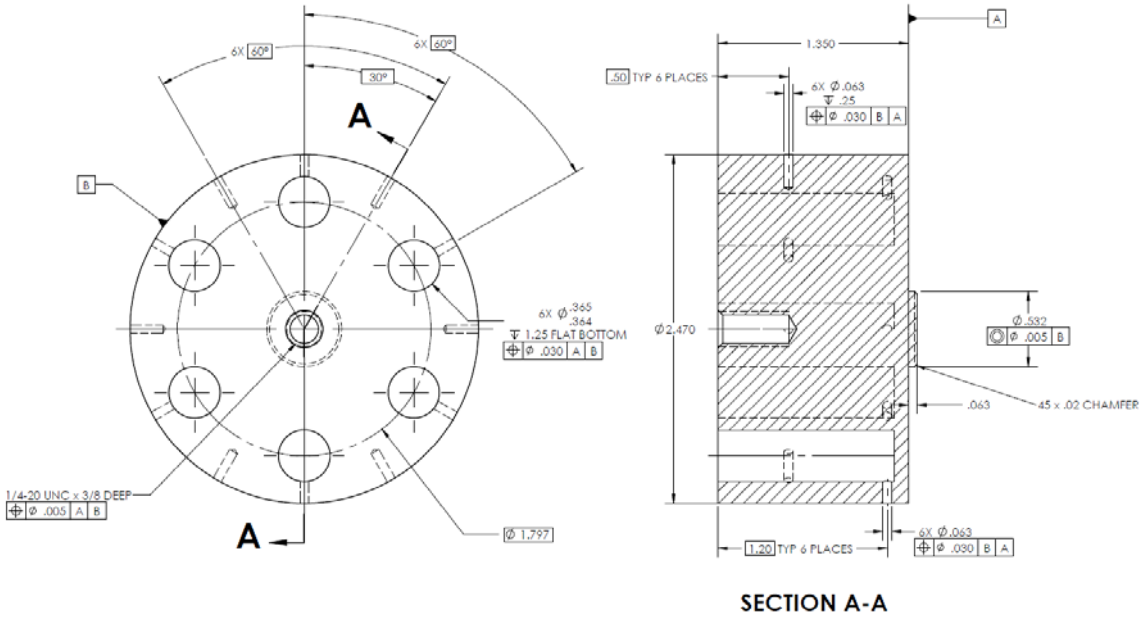

Figure 3. Heat Source Dimensions and Cartridge Heater Locations.

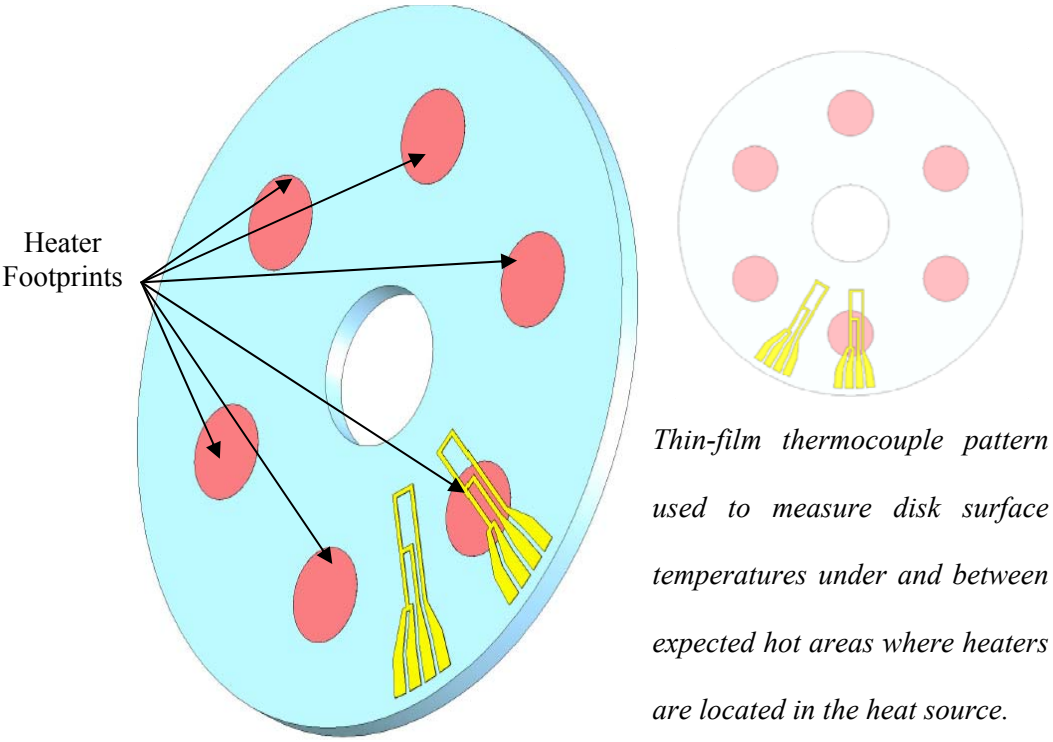

Figure 4. Thermocouple Arrangement.

2.1 Analytical and FEA Predictions

Analytical calculations and Finite Element Analysis (FEA) results were used to determine how invasive using a heat flux sensor might be to the Stirling test. The simulation results provided an approximate temperature difference across the sensor assembly based on heat input to the system from the heat source. This was used to assess how using a heat flux sensor might limit the life of the cartridge heaters located inside the heat source, which were expected to last thousands of hours.

Analytical calculations were performed by the author using Eq. (1) for 1-D heat transfer through the ceramic disk (3 mm thick) and through the two nickel spacers (sum to 6.5 mm). Predictions were made for heat flow values ranging from 180 to 300 W. At that time, only a constant thermal conductivity was available for the Alumina ceramic

disk. To simplify the calculation further, a constant value of nickel thermal conductivity was used. Perfect heat transfer was assumed at all internal interfaces so these results do not account for contact resistance between each of the mating parts.

Figure 5 shows the individual temperature difference across the Alumina ceramic disk and the both nickel spacers used in the heat flux sensor assembly for the 220 W heat flow case (nominal value expected in application). Figure 6 shows the resulting axial temperature profile through the heat flux sensor assembly. The resulting temperature drop through the thick spacer, ceramic disk, and thin spacer were 3 °C, 40 °C, and 5 °C, respectively.

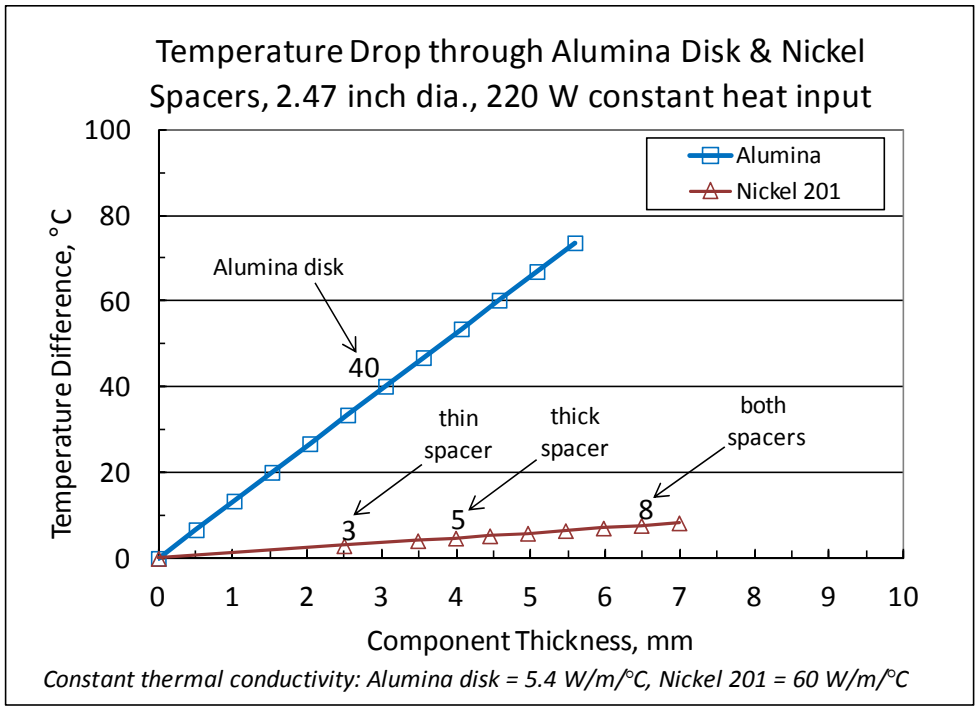

Figure 5. Analytical Results for Axial Temperature Drop.

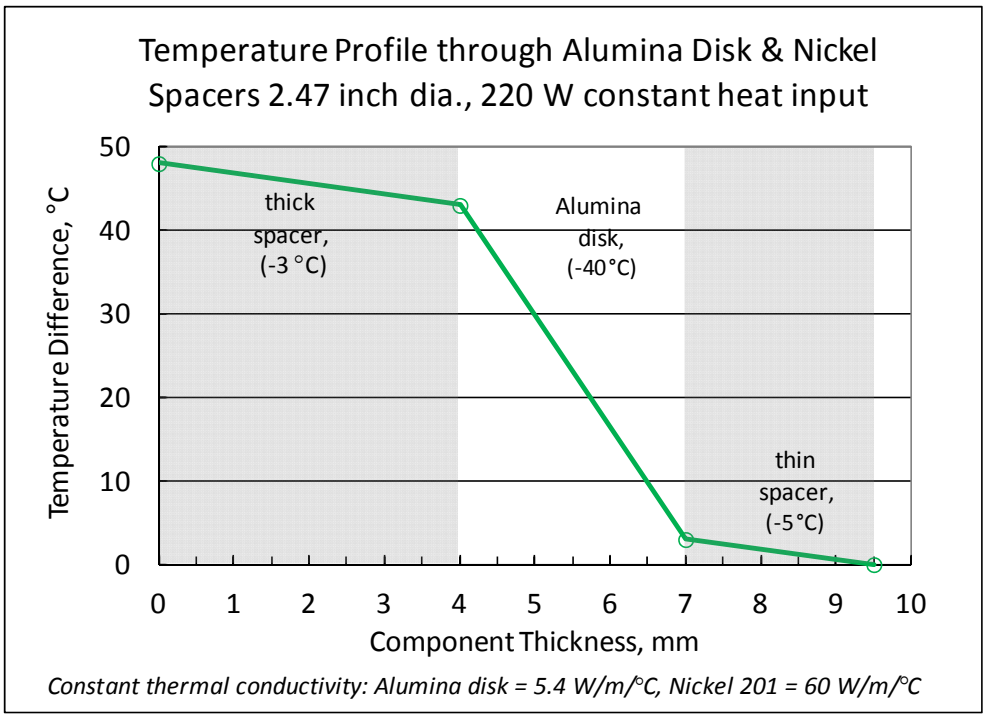

Figure 6. Analytical Results for Axial Temperature Profile.

To add confidence to the analytical prediction and study radial temperature variation, it was decided to use a Finite Element Model (FEM) to simulate the heat flux sensor assembly. Thermal analysis was performed by Art Atherton (Analex Corporation under contract to GRC) and the author using a commercial finite element analysis code (Ansys Workbench). Figure 7 shows the components modeled including the heat source, nickel spacers planned for each side of the heat flux sensor (Alumina ceramic disk), and a representative heat collector based on the Stirling convertor design. The resistance cartridge heaters, present in the nickel block heat source, would eventually be electrically powered using a variable direct current power supply and PID controller. The cartridge heaters mounted in the nickel block would also be preloaded against the ASC-E heat collector. The mechanical load applied to the heat source is discussed in Chapter IV.

Similar to the analytical calculations, constant thermal conductivity for the ceramic and nickel components were used. Also, perfect heat transfer was assumed at all internal interfaces so these results do not account for contact resistance between each of the mating parts.

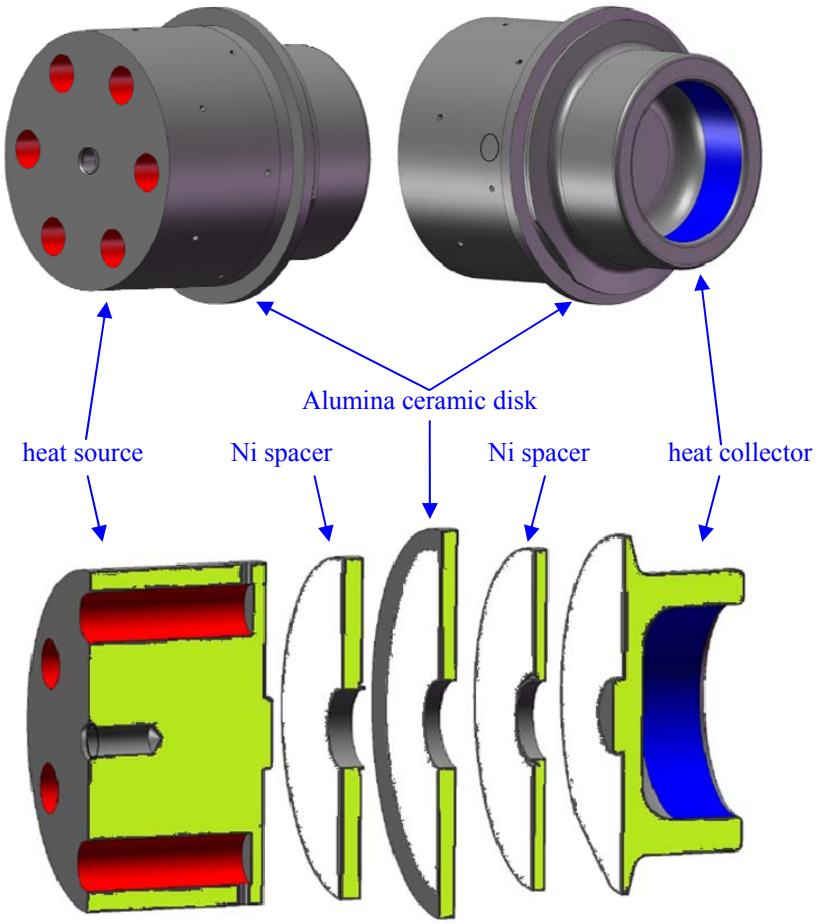

Boundary Conditions

Grey	Adiabatic
Red	Constant Surface Heat Input (Varied from 300 to 360 W)
Blue	Constant Surface Temperature (630 °C for all cases)
White	Internal interface of computational domain
Green	Cross-section used to clarify geometry

Figure 7. Modeled Components in FEM of Heat Flux Sensor Assembly.

The purpose of this analysis was to provide results for comparison to the analytical results and to provide an estimate for radial temperature variation on the face of the disk. Because it not used for accurate modeling of the test setup, approximate values were used to boundary conditions and some heat transfer paths that would normally be modeled were neglected.

The boundary conditions, shown in Figure 7, were applied to the surfaces of the model to simulate an expected range of steady state operating conditions for the Stirling test. A constant heat input was applied to the red surfaces shown on the heat source to represent heat input from the six cartridge heaters. A constant temperature was applied to the blue surface in the heat collector to represent the hot end temperature of the convertor and the energy lost to the Stirling cycle. The insulation loss was not modeled with the expectation that the resulting heat source temperature would likely be higher compared to tested values. Adiabatic conditions were applied to the remaining exterior surfaces, shown in grey.

The analysis was performed for five different values of gross heat input ranging from a lower than expected value of 300 W to an unlikely 360 W. Table I shows the resulting minimum, maximum, and average temperatures for each side of the heat flux sensor for each of the five cases. The heat transfer through the heat flux sensor was calculated based on the resulting integral-average temperatures for each side of the ceramic disk, geometry of the conduction path, and the thermal conductivity of the ceramic disk.

Table I. Thermal Analysis Results for Heat Flux Sensor Assembly

Boundary Conditions			Model Results							
Red surface	Blue surface	Orange surface	HFS face (Heat Source side)			HFS face (Stirling side)			Ceramic disk	
Gross heat input	Constant temp	Heat rejected (30 % of heat input)	Max temp	Min temp	Ave temp	Max temp	Min temp	Ave temp	Axial Temp. Diff. (ΔT)	Heat Transfer* (q)
(W)	(°C)	(W)	(°C)	(°C)	(°C)	(°C)	(°C)	(°C)	(°C)	(W)
300	630	90	746	715	737	721	689	698	39	209
315	**630**	**95**	**751**	**720**	**743**	**725**	**692**	**702**	**41**	**220**
330	630	99	758	724	749	730	695	705	44	236
345	630	104	764	728	754	735	698	708	46	247
360	630	108	770	733	760	739	700	712	48	257

** $q = k*(A/\Delta x)*\Delta T$; constant thermal conductivity (k) = 5.4 W/(m-°C); Constant $(A/\Delta x)$ = 0.993 m*

The results suggested the axial temperature difference across the thickness of the ceramic disk could range from 39 to 48 °C, depending on the heat input. The 220 W case resulted in an axial temperature drop of 41 °C, which agreed well with the predicted 40 °C from the analytical calculations. The maximum radial temperature difference across the face of the ceramic disk could range from 30 to 39 °C. However, most of the change in temperature on a face resulted away from the heat transfer area near the outer edge of the disk which is not in contact with the spacers. The sensor has a slightly larger outer diameter than the nickel spacers that surround it to enable wire connections. That outer portion of the disk accounts for about 84% of the difference in face temperature while the larger heat transfer area, having a relatively uniform temperature across the face of the disk, accounts for about 16% of the difference in face temperature. The thin-film thermocouples are located in the mostly uniform temperature distribution, seen in Figures 9 and 10. The integral average temperatures available from the model were thought to be a reasonable way to report temperature due to the relatively small temperature gradient across the heat transfer area of the ceramic disk.

The FEA generated temperature gradients shown in Figures 8, 9, and 10 are results from the unlikely case of 360 W heat input. The exploded view of the assembly and both sides of the heat flux sensor are shown. The proposed implementation used Alumina coated spacers to protect the thin metallic films from diffusing into the nickel ASC-E heat collector and heat source. One disk was made to be thicker in an attempt to better distribute nonuniform temperature gradients expected from the locally heated zones directly under the heaters. The FEA results, seen in Figure 8, did show local heat zones in a cartridge heater pattern on the thicker nickel spacer and a relatively uniform circular temperature profile on the mating face of the ceramic disk itself, suggesting that the spacer thickness was sufficient for achieving an significantly improved temperature distribution.

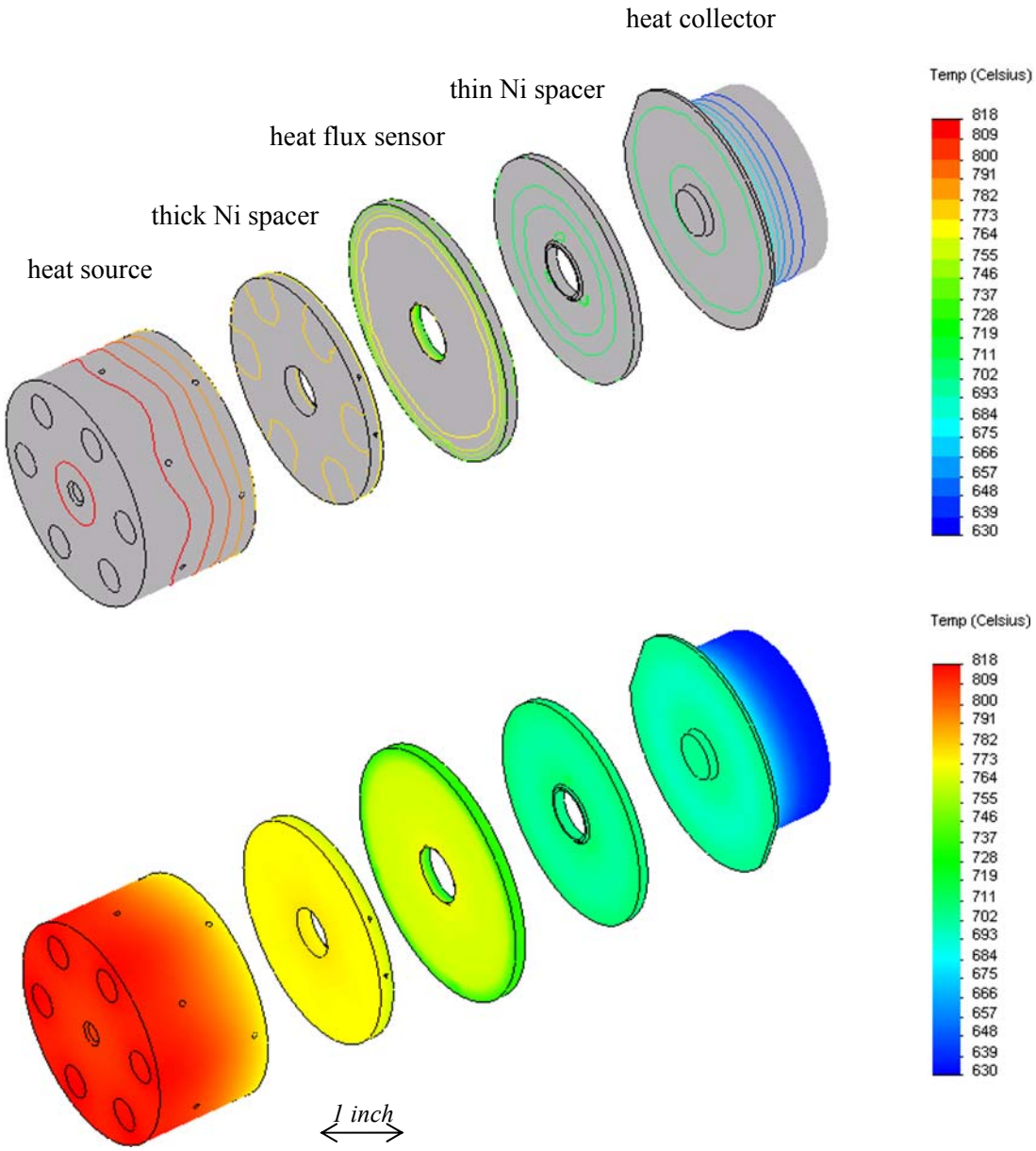

Figure 8. Thermal Analysis Temperature Results for Heat Flux Sensor Assembly.

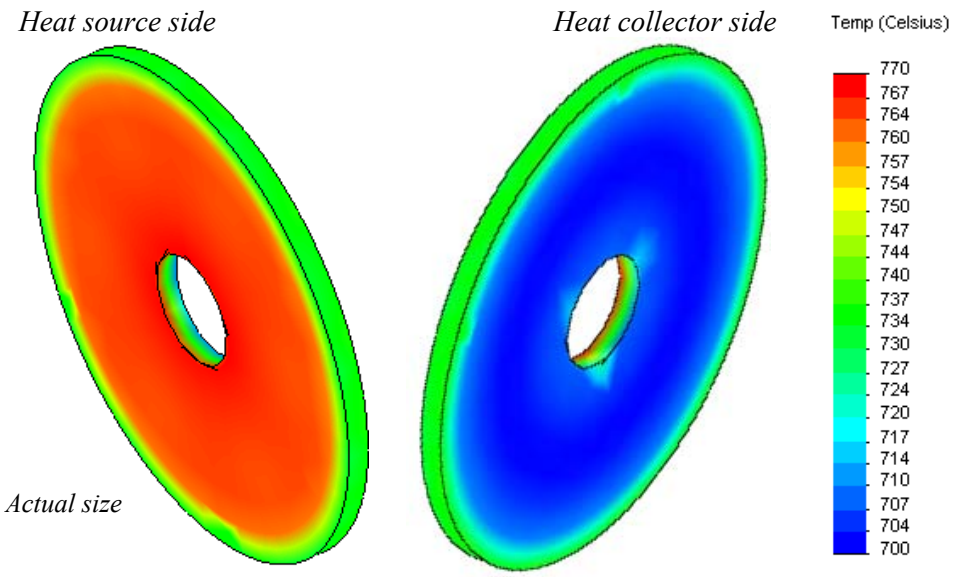

Figure 9. FEA Temperature Results for Alumina Ceramic Disk, *Both Sides Shown*.

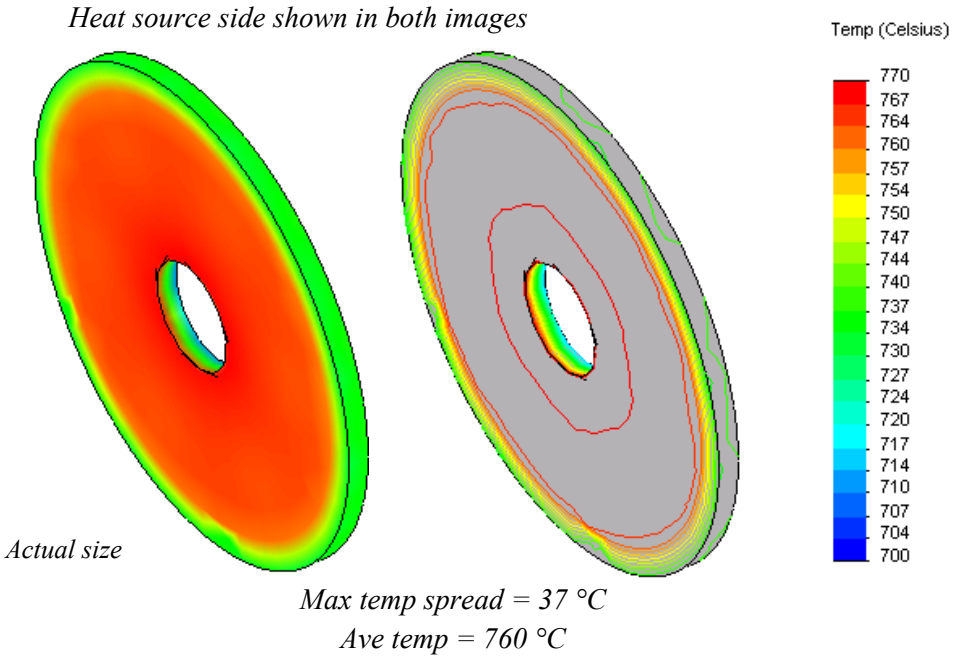

Figure 10. FEA Temperature Results for Alumina Ceramic Disk, *Hot Side Only*.

Mesh independence was studied by running the 315 W case using different tetrahedral mesh densities available in Ansys Workbench. The mesh density was varied and the resulting temperatures were documented. For this geometry, the Ansys Workbench mesh tool was not able to resolve mesh densities less than or equal to 0.100 inches or greater than or equal to 0.190 inches. However, three mesh densities between those limits were resolved and used to inspect the results for changes and gross errors. The resulting temperatures did not very significantly for each of the mesh densities used. The greatest change observed was a 1.2% decrease in the maximum temperature observed on the colder side of the ceramic disk face. Table II shows the resulting minimum, maximum, and average temperatures for each side of the ceramic disk.

Table II. Thermal Analysis Results for Heat Flux Sensor Assembly

	Boundary Conditions			Model Results						
	Red surface	Blue surface	Orange surface	HFS face (heater side)			HFS face (Stirling side)			Ceramic disk
Ansys Workbench Mesh Size	Constant heat input	Constant temp	Heat rejected (30 % of heat input)	Max temp	Min temp	Ave temp	Max temp	Min temp	Ave temp	Heat Transfer* (q)
Inch	(W)	(°C)	(W)	(°C)	(°C)	(°C)	(W)	(°C)	(°C)	(W)
0.100	Mesh creation failed									
0.150	315	630	95	754	720	744	734	692	701	231
0.179	**315**	**630**	**95**	**751**	**720**	**743**	**725**	**692**	**702**	**220**
0.185	315	630	95	751	719	743	725	691	701	225
0.190	Mesh creation failed									

** $q = k*(A/\Delta x)*\Delta T$; constant thermal conductivity (k) = 5.4 W/(m-°C); Constant ($A/\Delta x$) = 0.993 m*

2.2 Ceramic Substrates

The ceramic substrate thickness was chosen for the Stirling application based on an assumed robustness of a roughly 1/8 inch thick disk and the desire to maximize the temperature difference and sensor output. The Alumina substrates shown in Figure 11

were made via slipcasting, in which the powder was ball-milled in an aqueous solution, binders and dispersants were added, and castings were bisque fired and fully sintered. The bisque fired and fully sintered heat treatment is provided.

Bisque fire: Ramp to 300 °C at 1 °C/min and soak 1 hr, Ramp to 600 °C at 1 °C/min and soak 1 hr, soak for 1 hr, Ramp to 1,200 °C at 1 °C/min and cool down at 3 °C/min

Fully Sinter: Ramp to 1,500 °C at 1 °C/min and soak 2 hr and cool down at 3 °C/min

The disks were then machined to a thickness of 0.120 ±.0005 inches with a near mirror surface finish. Earlier attempts resulted in disks containing voids and cracks, shown in Figure 12. These disks were tested during Robustness Testing trials covered later in this document. Despite having cracks and voids, the disks survived hour long tests with ramp rates of over 1 °C / min and reaching axial loads of over 400 lbs at temperatures above 700 °C.

The thermophysical properties were then measured for the lot of ceramic disks fabricated. Thermal conductivity tests were performed by Ali Sayir of GRC's Ceramics Branch according to the specifications of ASTM E1461 test method. The Flash-LineTM 300 System (Anter Corporation) was used to perform the measurements with an expanded uncertainty of ±2.1 % for 95 % confidence limit. These measurements were made in flowing nitrogen at GRC. Five samples were randomly selected from Alumina substrates fabricated by Tom Sabo (Ohio Aerospace Institute) in GRC's Ceramics Branch. The test process involved taking laser measurements, during which three consecutive laser pulses were used to obtain an average thermal diffusivity. For each temperature, up to 13 measurements were repeated to obtain the statistical confidence level. The results for thermal conductivity are shown in Figure 13 and in Table A-1. The

value of mean thermal conductivity was used for all heat flux calculations on sensors made from the same lot of Alumina.

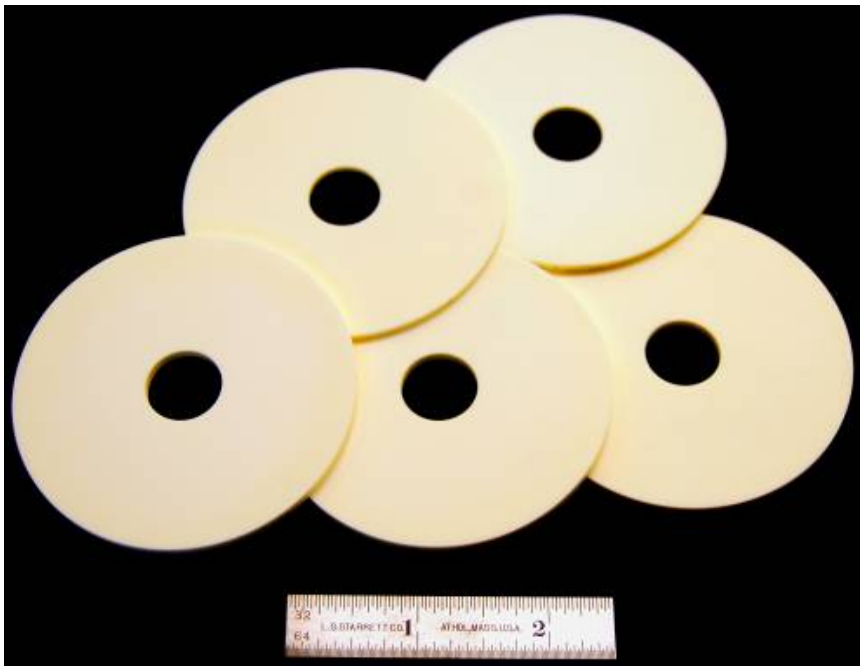

Figure 11. Production Alumina Ceramic Substrates.

Figure 12. Prototypical Mullite and Alumina Ceramic Substrates.

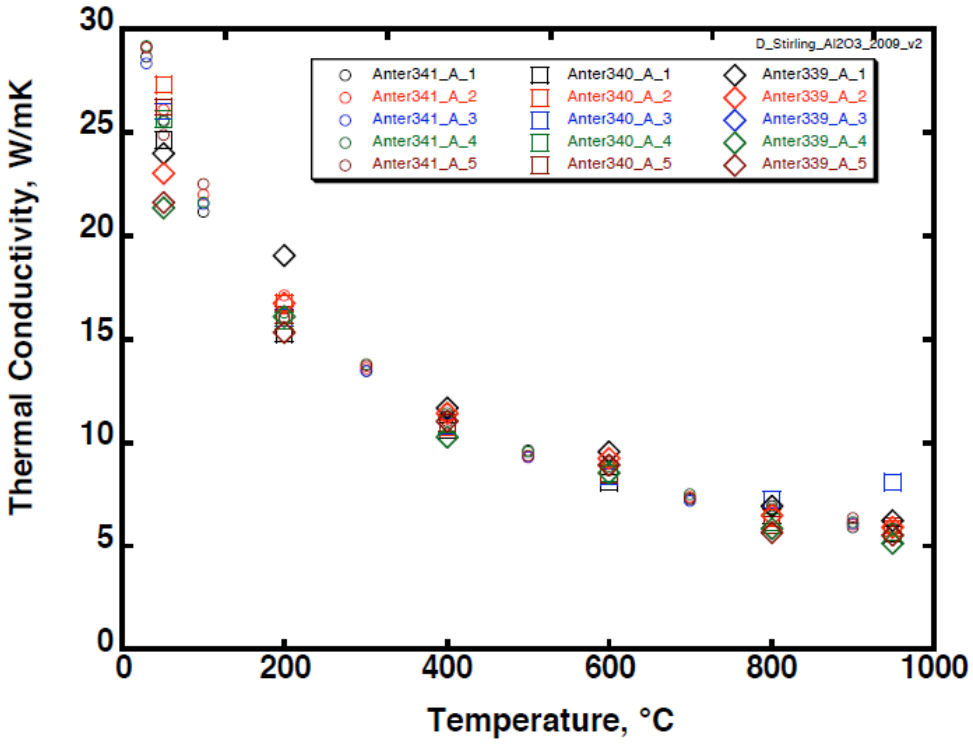

Figure 13. Alumina Thermal Conductivity Test Results.

2.3 Thin-Film Deposition

The sensors were designed to measure temperatures that could vary on the face of the sensor due to local heating of the cartridge heaters located in the heat source. To adequately capture radial and circumferential variations in temperature, and therefore heat flux, sensors were spaced out in the radial direction and placed under and between heaters. Figure 14 shows the thermocouple arrays present on both sides of the disk. The negative and positive legs of the photolithography pattern are shown. For the Type-R thermocouples, the positive leg, used as the common ground for all junctions, was made from Pt-13% Rh while the negative leg was made from pure Pt. Similarly, for the nonstandard Au versus Pt thermocouples, the positive leg was made from pure Au while the negative leg was made from pure Pt. The pattern shown in Figure 14 was deposited

on one side of a disk and its mirror image on the opposite side. This enables a calculation of heat flux at the various radial and circumferential locations.

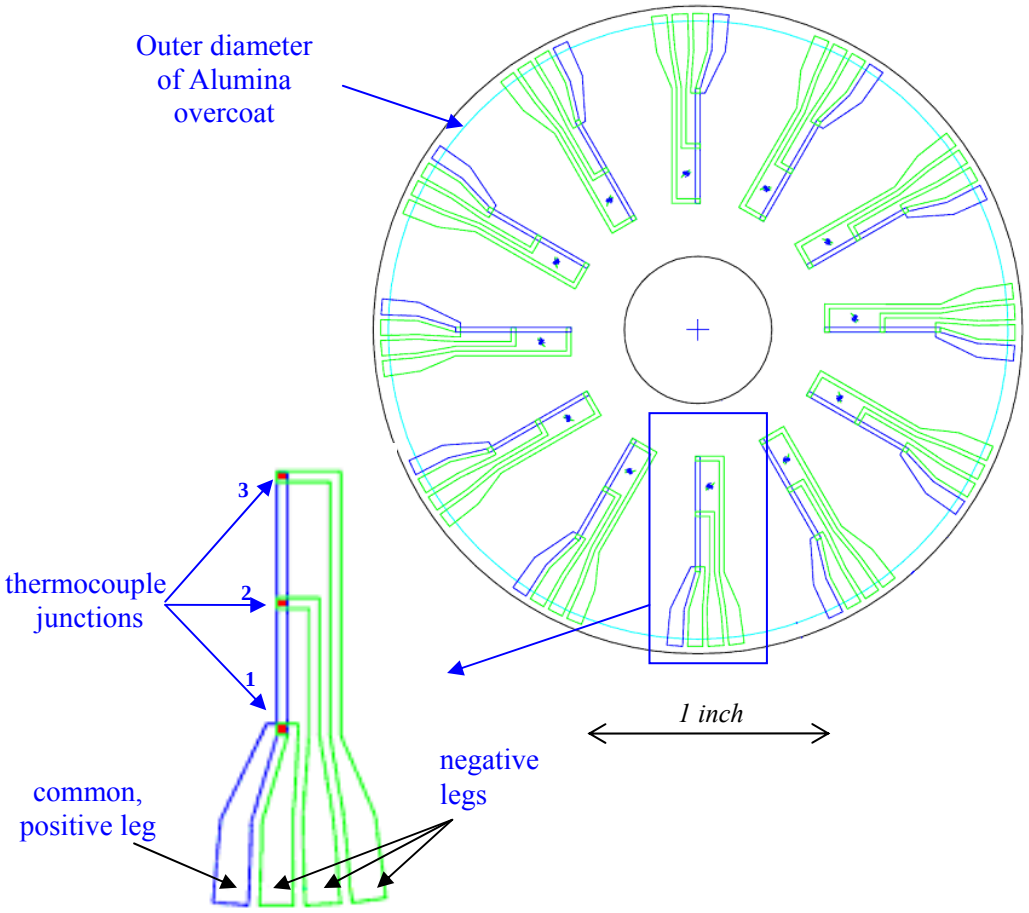

Figure 14. Photolithography Pattern.

Figure 15 shows the patterns on each side of the disk. The figure also shows the pattern of thermocouple junctions located under the footprint of each heater. Three thermocouple junctions are present in every array. It was originally planned to locate Junction 1 toward the outer diameter of the disk, Junction 2 directly under a heater, and Junction 3 closer to the inner diameter of the disk. The design for the sensor was locked

and the stencils were purchased. The heat source design was later modified slightly to suit other design needs which misaligned the center junction from the center of the cartridge heater. The change was thought to be relatively low impact to the overall goal of demonstrating successful implementation into the Stirling application and the decision was made to continue with the existing masks.

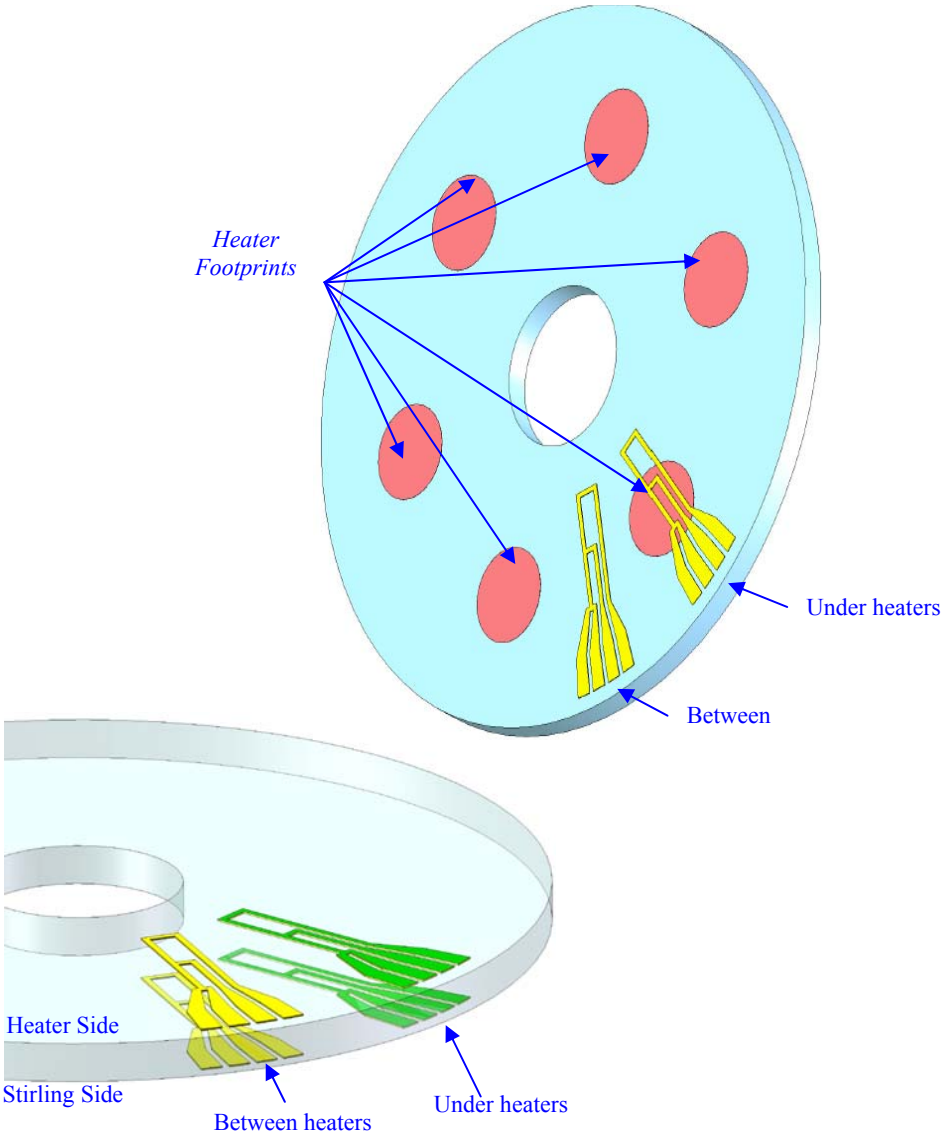

Figure 15. Thermocouple Arrangement.

Each side of the sensor has an arrangement of (12x) thermocouple arrays although only two arrays are wired and the other 10 serve as spares in case wire connections were not successful or some of the films were damaged during fabrication.

The first heat flux sensor trial pieces were fabricated using Mullite ceramic substrates and thin-film Type-R thermocouples and wires. The thin-film deposition was also performed at GRC using the Physical Vapor Deposition method. Films of ultra high purity (99.99+%) were sputtered in vacuum. The deposition process went as planned until contamination issues, thought to be caused by a photo-resist reaction, prevented successful photolithography deposition. After several unsuccessful attempts to find the root cause, the deposition method was switched from photolithography to using shadow masks. Figure 16 shows the first shadow mask Type-R thermocouple sensor.

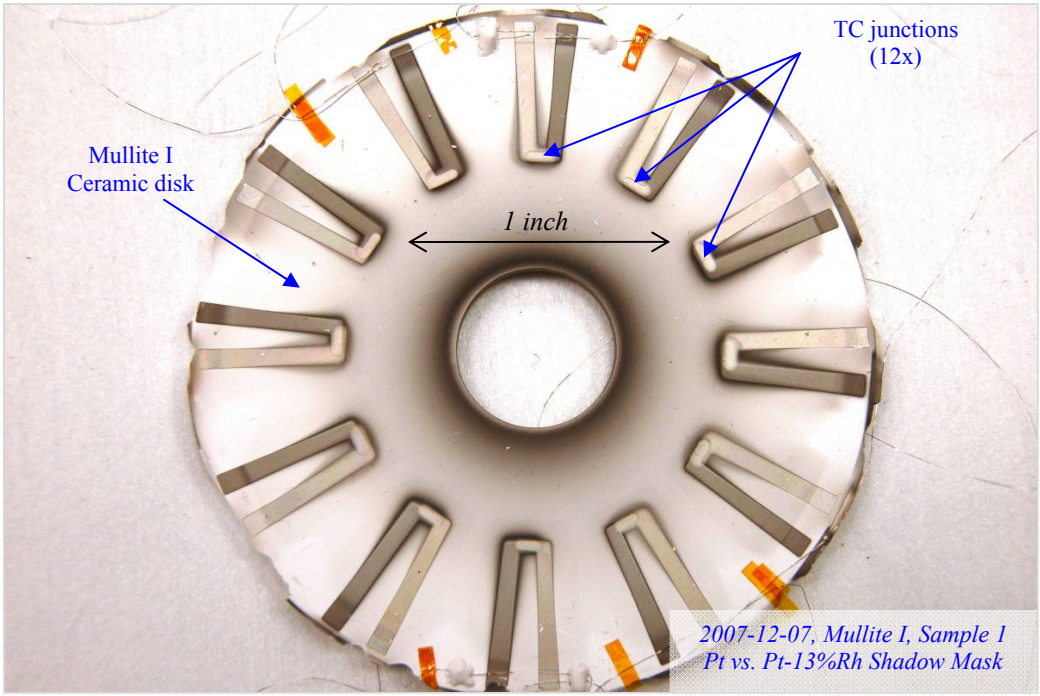

Figure 16. Type-R Thermocouple Shadow Mask Patterns on Mullite.

The pattern contains a single radial junction, again located under the heater. After the successful deposition of two shadow mask sensors, wire attachments were attempted. Figure 17 shows a close up view of the sensor with bare platinum and rhodium wires attached. Attaching 76 µm diameter wires using the laser bonding method was unsuccessful for the common legs only. The problem was resolved by using 25µm diameter wire. The initial version of Mullite (version I) was a relatively low density ceramic. Both sensors were damaged around the edges from normal handling and processing. A higher density version of Mullite (version II) disks were also being fabricated to improve robustness. With the high risk of wires being damaging during handling and the low reliability of the Mullite I, an additional set of sensors would be fabricated using the Mullite II disks. At this time, it was decided to fabricate the sensors using photolithography patterns on the Mullite II (and eventually a nearly full dense version called Mullite III).

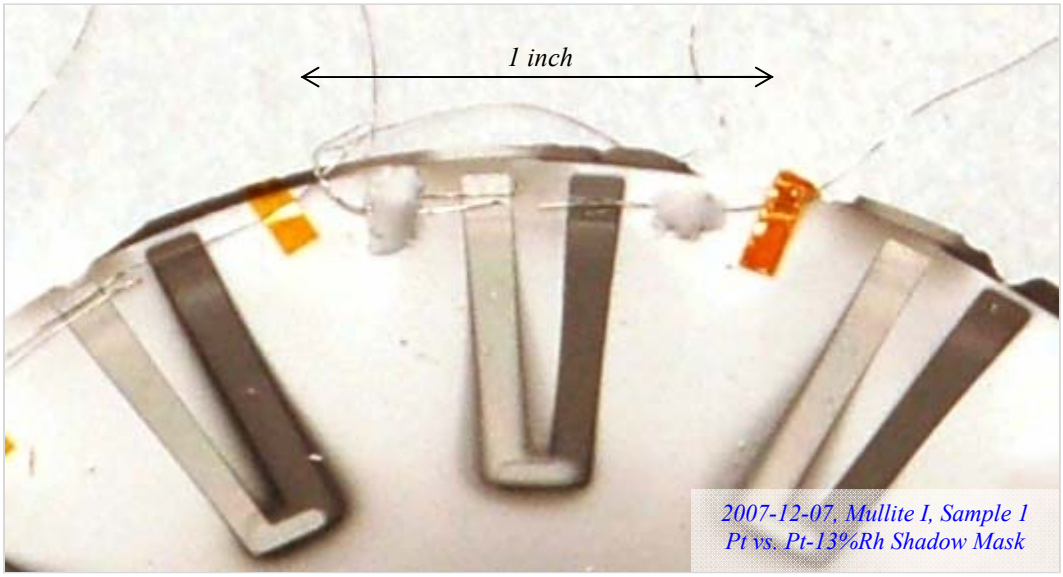

Figure 17. Type-R Shadow Mask Pattern, *Damage To Outer Edges*.

Type-R photolithography patterns were attempted again with more focus on solving the contamination issue, which was traced back to contamination of the vacuum furnace used to anneal the sensors after the patterns were sputtered. In initial trials, the bond strength of the positive leg (Pt-13% Rh) of the Type-R thermocouple films was inadequate on the Mullite III disks, as shown in Figure 18. The top images show each side of one disk where many of the patterned legs have failed. The bottom image shows the common legs that were found to have lifted off of the substrate. To improve the bond strength, the decision was made to replace the Mullite substrates with Alumina substrates and photolithography was attempted once again.

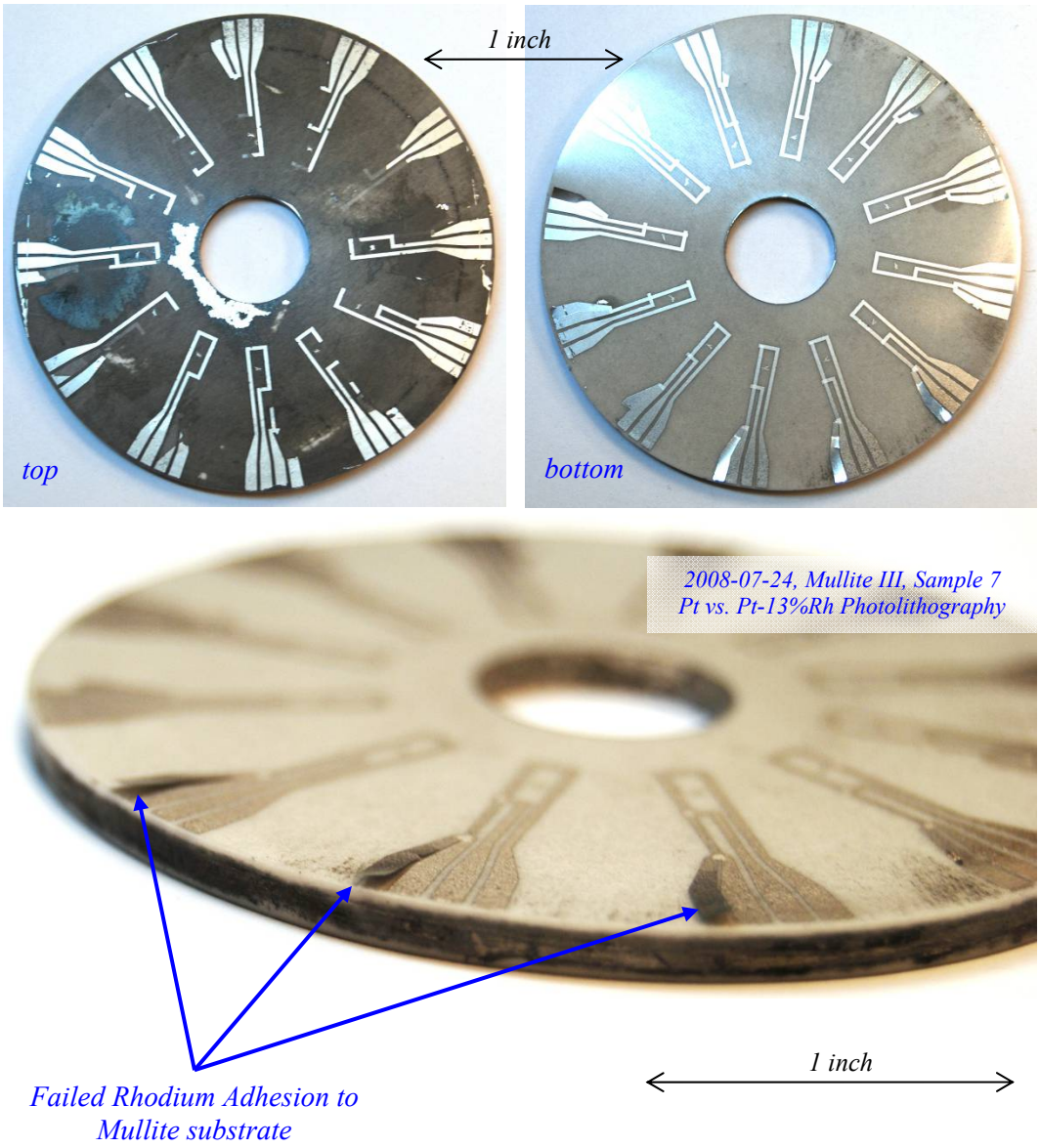

Figure 18. Type-R Photolithography Pattern on Mullite.

Using the Alumina substrates resulted in increased bond strength over that of Mullite. Figure 19 shows the Alumina sample 12 at several stages of development. After it was successfully deposited, shown in (A), it underwent vacuum anneal, shown in (B). Oil back streaming into the vacuum chamber was believed to have caused the discoloration. That belief was strengthened after air anneal, shown in (C), essentially cleaned the sensor. However, it was a temporary success as the additional ultrasonic cleaning step damaged the Type-R photolithography pattern on Alumina.

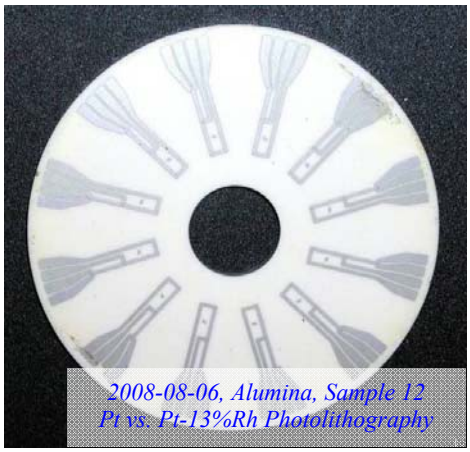

(A) Sample 12 before vacuum anneal.

(B) Sample 12 after vacuum anneal.

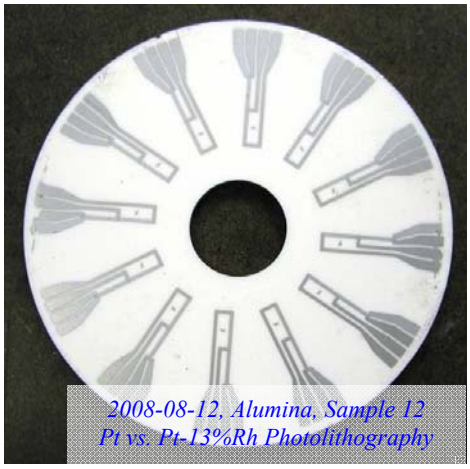

(C) Sample 12 after air anneal.

(D) Sample 12 after ultrasonic cleaning.

Figure 19. Continued Type-R Photolithography Sensor Development.

To increase the deposition bond strength, it was decided to pursue a new combination of noble metals for use on the photolithography pattern. The use of gold versus platinum was suggested because of gold's resistance to corrosion in oxidizing environments, its notable stability, and the *emf* voltage output was expected to be 5 times higher than that of the Type-R thermocouples reducing the chance of electrical noise interference (Type-R ~6 μV/°C, Au vs. Pt ~30 μV/°C). One known obstacles to using gold would be the necessity to program all of the NIST calibration tables into LabVIEW due to it being a nonstandard and unsupported thermocouple type. Another assumed risk was damage to the less robust 76 μm diameter gold wire.

Before the decision had been made to use gold as the common leg, the concept of using a wire support arm had been suggested as a way to provide the, at the time, 25 μm diameter wires with a safe path to exit the test setup and protect the bonds of small diameter noble metal wires to 1 μm thick films. Sample 12 was used to test the concept of the wire arm support arm. The arm, machined from Foam 50 board, appeared to be a suitable means for protecting bonds made by either laser bonding or parallel gap welding. However, getting the support arm to bond to the ceramic disk was difficult and a couple of different ceramic pastes were attempted. Even after the bond was successfully made using the Aremco 503 Alumina paste, the arm/bond was damaged during the vacuum anneal. Figure 20 shows the arm before and after the heat treatment, where the blackened portion of the arm is apparent. Additionally, an arm became disconnected from a ceramic disk during Robustness Testing, discussed in Section 2.5. The test subjected the test specimen to a moderate temperature of around 550 °C. After both experiences, the

concept was abandoned. By that time, the wire diameter had already been increased to 76 μm due to the parallel gap welding process and was considerably more robust.

One interesting aspect of the wire support arm is that it did, in a way, provide safe travel for the delicate wires. To prepare for the presence of the support arm, a pocket was designed into the micro-porous insulation, planned for use in the test setup. By the time the concept of the support arm had been abandoned, the pocket had already been designed and produced as part of the insulation for the setup. The wires nested comfortably into the pocket and exited the insulation, seen later in Chapter IV.

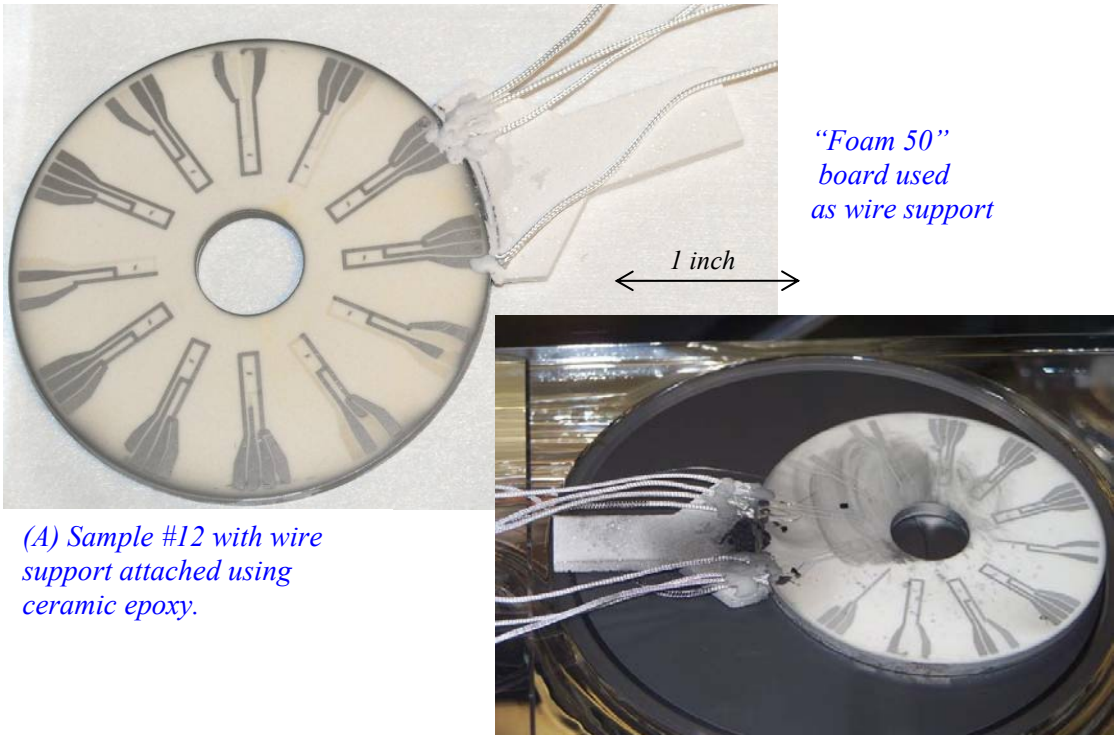

(A) Sample #12 with wire support attached using ceramic epoxy.

(B) Sample #12 after air anneal, arm detached after removal from furnace.

Figure 20. Wire Support Arm Failure.

Gold films were substituted for the Pt-13% Rh films. The gold versus platinum thermocouples have very good stability, a slightly higher output and lead wire attachment was less problematic.[11,12] One concern was that the melting point of gold (1,064 °C) precluded using this design on other tests with a hot-end temperature of 850 °C and anticipated heat source temperature of 1,000 °C because the expected sensor temperature would meet or exceed the recommended application temperature of 950 °C. Still suitable for tests with a hot-end temperature of 650 °C and anticipated heat source temperature of 750 °C, fabrication continued for use on ASC-E #1 and #4. The fabrication process was successful using Au vs. Pt thermocouples deposited onto Alumina substrates in December 2008. Figure 21 shows Sample 13 which was used in Robustness Testing and Sample 14 which progressed on to become one of the first sensors delivered.

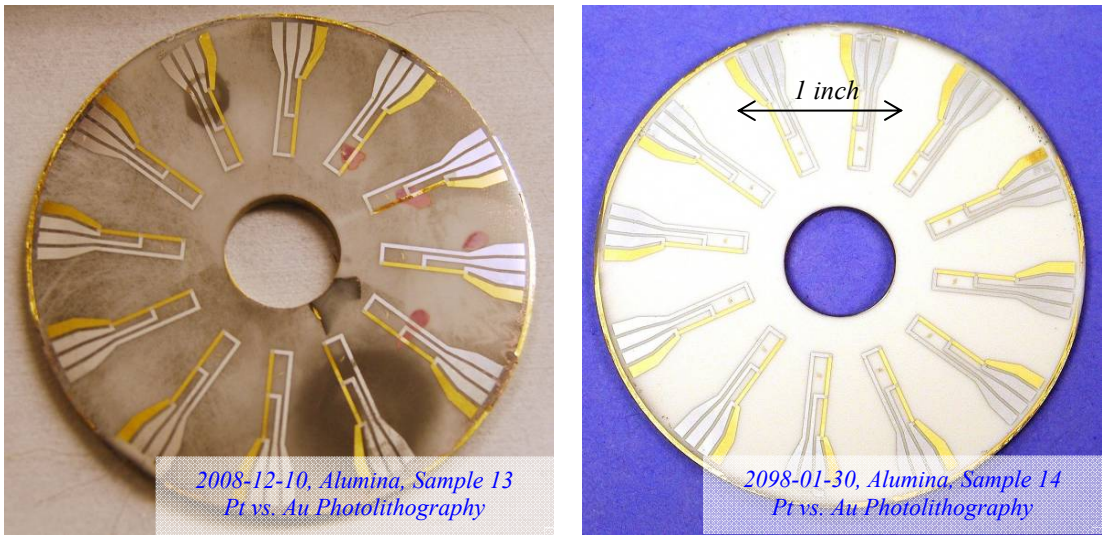

(A) Sample #13 used in Robustness Testing. *(B) Sample #14 after vacuum anneal.*

Figure 21. Continued Type-R Photolithography Sensor Development.

Before attachments were attempted, the gold and platinum wires were pre-insulated using an Alumina-fiber wire insulation with an inner diameter of 0.3 mm and a maximum operating temperature around 1,250 °C. The wire insulation is described more in the next section. The wire connections, discussed in the next section as well, were made successfully using parallel gap welding and Aremco 503 Alumina paste. Figure 22 shows the sensors delivered during February 2009.

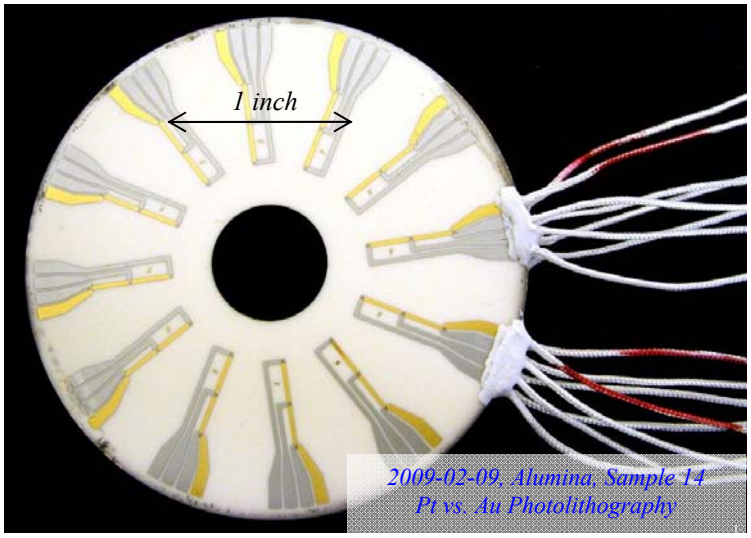

(A) Sensor 1 after wire installation.

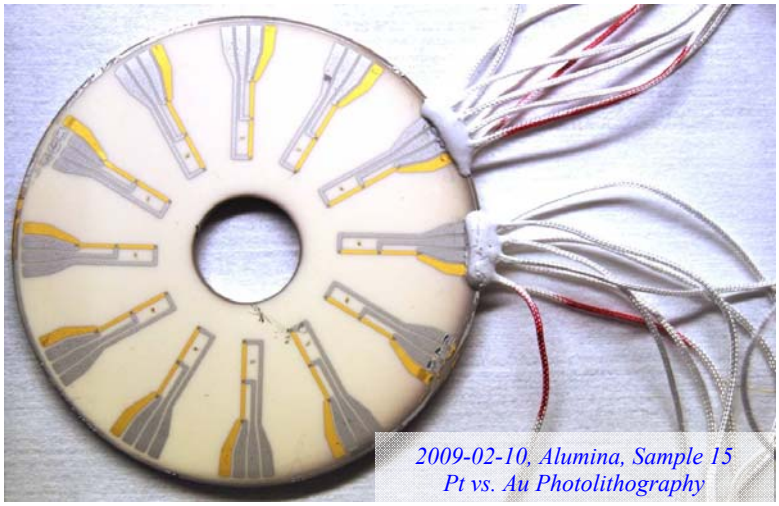

(B) Sensor 2 after wire installation.

Figure 22. Delivered Gold Verses Platinum Sensors.

The sensors were checked out by measuring the emf voltage on the loose wires, soldering the wires to the custom-made wire feed through, and repeating the emf voltage measurement using an Agilent multimeter. Sensor 1 was delivered with one failed platinum junction, Junction 8, which meant that the sensor still had 11 out 12 temperature measurements available. Sensor 2 had been delivered with one failed gold junction, common leg to Junctions 7, 8, and 9, which meant that the sensor only had 9 out 12 temperature measurements available. During the last step of checkout, an additional gold leg was found to have failed. This identified the issue of low bond strength between the gold films and Alumina substrate. Because the process was well known, a replacement sensor, shown in Figure 23, was fabricated in under 3 weeks.

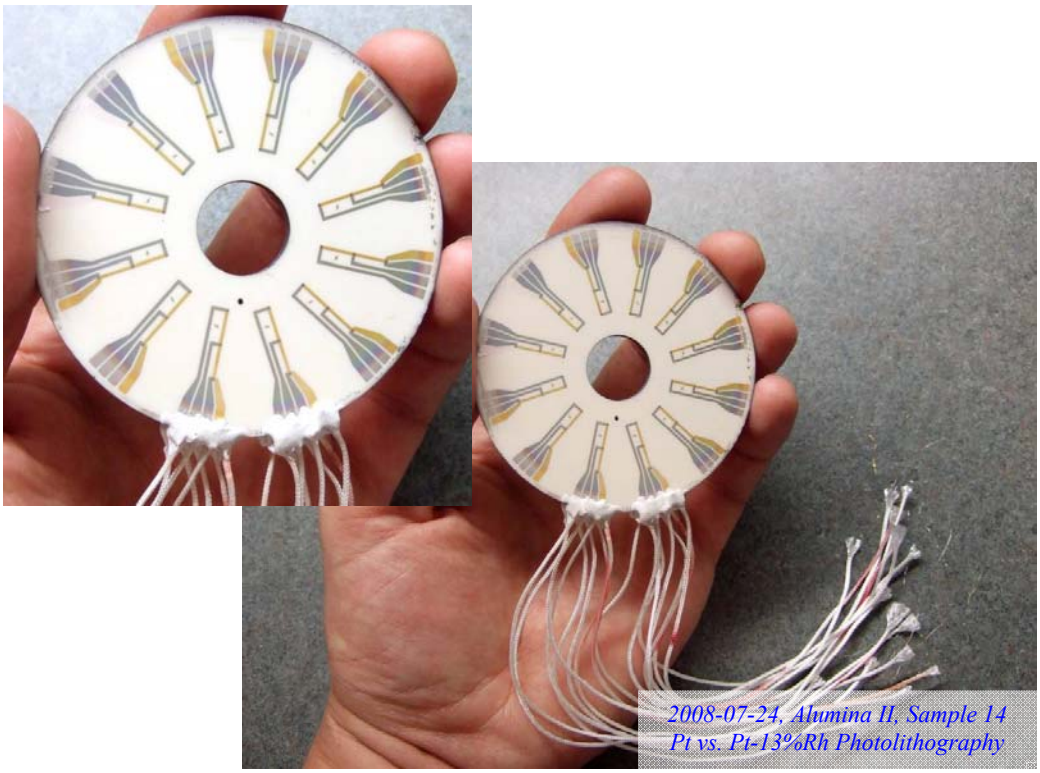

Figure 23. Sensor 3, Au vs. Pt Thin-Film Thermocouples on Alumina.

2.4 Wire connections and Custom-made Wire Feed Through

Parallel gap welding was performed by Chuck Blaha (Jacobs Technology) in GRC's Sensors and Electronics Branch. The 76 μm diameter wires were connected to the 1 μm films using parallel gap welding. The process was achieved by making an attempt at connecting the wire with a pulse of energy in the parallel gap welding apparatus. This process was repeated until a successful connection was made. Each additional attempt put the film at risk to permanent damage but ultimately resulted in successful attachment of all wires, making this a fairly repeatable process. Once the wires were attached to the thin films, the disks were delivered to Scott Wilson (author) of GRC's Thermal Energy Conversion Branch where the remaining connections were made. Terry Jansen, an electrical technician in GRC's In-Space Power and Propulsion Division, soldered the 76 μm diameter noble metal wires to much larger copper extension wires. The extension wires were potted in a custom-made wire feed designed and fabricated by the author. The non-hermetic wire feed through, shown in Figure 24, were potted using an electrically insulating, thermally conductive epoxy, 3M's Scotch-Weld Epoxy Adhesive 2216 B/A Gray. The diameter of a single copper wire (multi-wire twisted group, not single solid) measured roughly 0.6 mm and the diameter of a three-wire twisted bundle measured roughly 2.0 mm. Figure 25 shows the relative size difference between the noble metal wire and the extensions wires, a factor of 26 times. A two step method was used to successfully connect all (4x) gold wires and a single step method was used on the (12x) platinum wires. The gold wires were first pre-tinned with SN63PB37 at 500 °F. They were then soldered to the three-wire twisted bundle at 600 °F using Kester 951 Flux and Kester Solder (SN63PB37, #50/245, 0.38 mm, 24-6337-8806, ANSI-J-STD-006A, DOM:

APR/09/08, Lot# N800694). The platinum solder connections were made in a single step using the same flux paste and solder wire but at 700 °C.

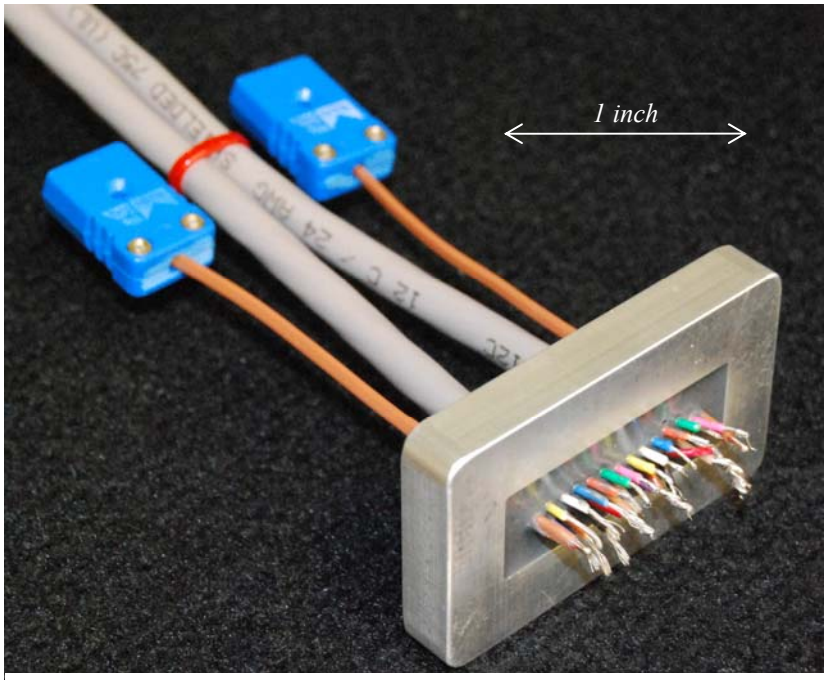

(A) Custom-made wire feed through contains copper extension wire potted in aluminum mounting plate.

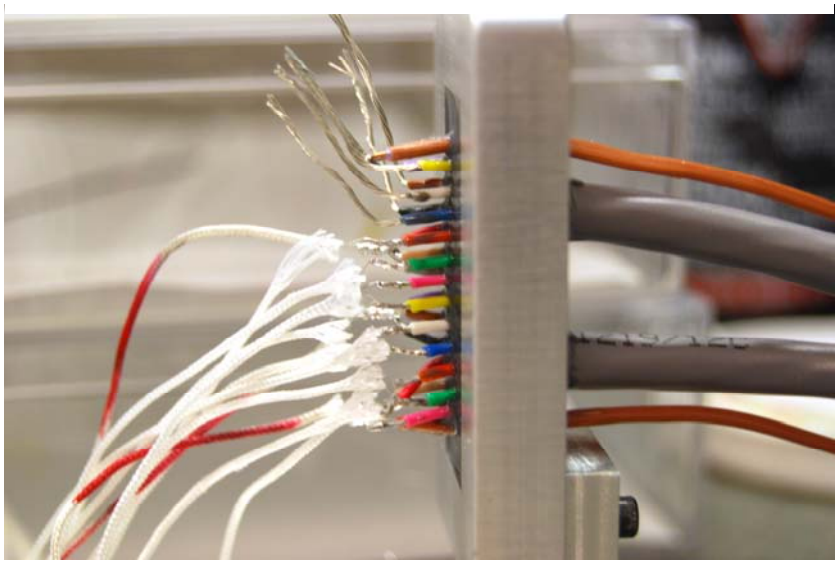

(B) Nobel metal wires (Ø 0.003 inch) soldered to copper extension wire (potted in wire feed through).

Figure 24. Custom-made Wire Feed Through.

Wire insulation was used to protect the noble metal wires from touching each other or the neighboring thermocouple wires present in the spacers. The wires were hand fed, by Chuck Blaha, through the small diameter fiber insulation by gluing the end to a larger wire, feeding the larger wire through, then cutting the larger wire off. Nitivy Boria-Free Continuous Alumina-Silica Fiber "Nitivy ALF^{TM}" (Nitivy ALF SV-1-XP, 0.3 mm ID) was ordered from Nitivy Co., LTD. through Armil CFS, Inc., a certified vendor located in the USA. It had an advertised temperature limit of 1,250 °C and was relatively flexible before and after heating. The recommended "heat cleaning" procedure was performed to drive out carbon monoxide. The insulation was air-annealed at 850 °C for 2 hours.

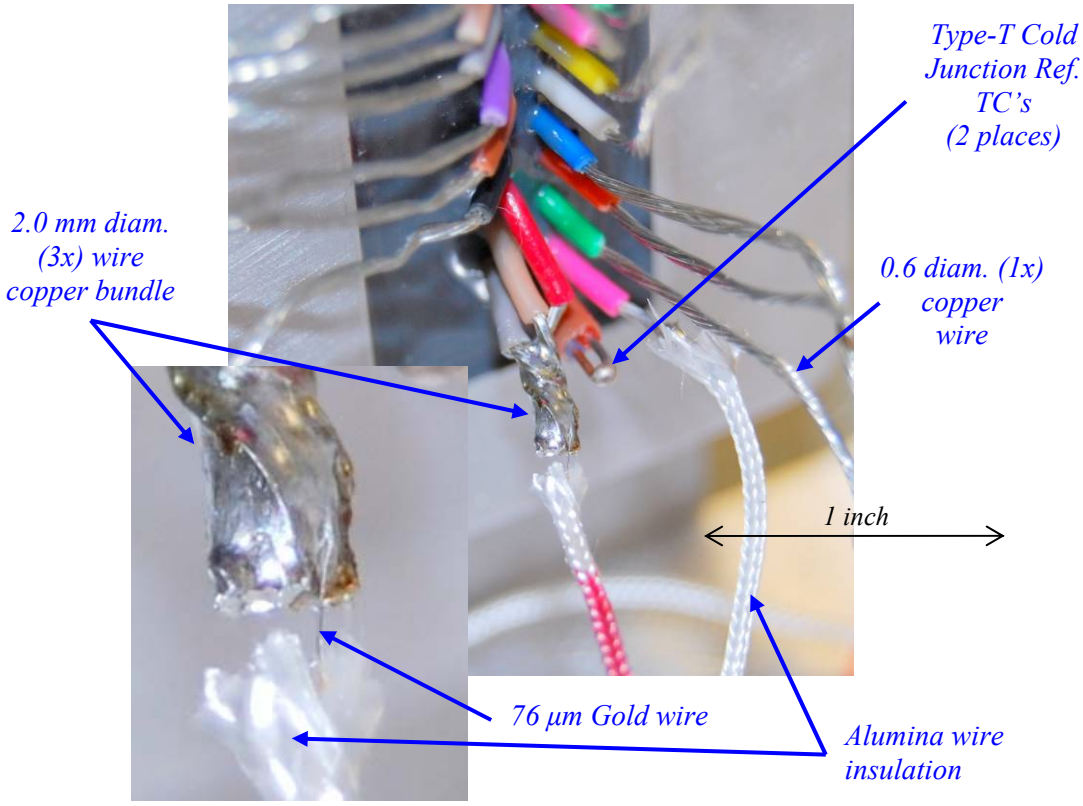

Figure 25. Noble Metal Wire Connected to Copper Extension Wire.

2.5 Material Robustness Testing

The metallic and ceramic components being considered for use in the heat flux sensor assembly were tested to characterize the survivability and identify areas of improvement for design and/or fabrication techniques. The test subjected samples to conditions expected in the intended application including temperature transients, peak temperatures, and mechanical loading. Figure 26 shows the intended load condition expected in application. A 300 lb load was planned for testing in the ASC-E #1 and #4 test setup, although a higher load of 400 lb was being considered by management prior to assembly. It was decided to test the samples at the higher load for proof of concept at the load being considered and to provide margin over lower values already selected.

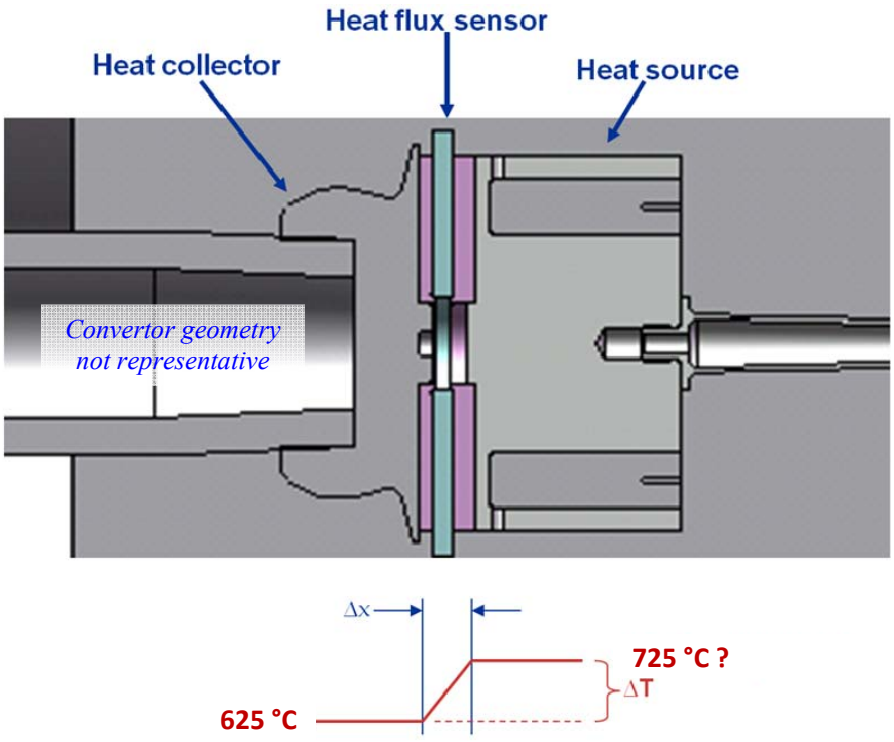

Figure 26. Planned Implementation of Heat Flux Sensor.

Six combinations of test article were tested including Alumina and Mullite ceramic substrates, nickel and Alumina spacers, and nickel disks with and without nickel oxide layers and aluminum oxide layers. Figure 27 shows the numerous test samples tested.

Figure 27. Ceramic and Metallic Test Samples for Robustness Testing.

The nickel oxide layers were used to prevent diffusion bonding of the nickel parts at high temperature and the aluminum oxide layers were used to electrically insulate the face of the nickel disk planned to interface the sensor. Overall, the ceramic substrates held up exceptionally well under mechanical loads, thermal cycling, and peak temperatures similar to those expected in the application. Alumina substrates were tested

using an axially applied mechanical load from 400 to 475 lb. The highest load tested provides about a 60% margin over the baseline 300 lb load planned for Stirling testing.

The test identified (1) available margin in mechanical load and thermal transients, (2) possible failure modes for the ceramic and metallic components, (3) required improvements for metallic spacer fabrication, and (4) a combination of materials for minimum temperature drop across the heat flux sensor assembly. The test setup included parts necessary to apply the mechanical load and temperature difference to the test articles. Figure 28 shows a design graphic and as-built photo of the load assembly, heat source, test articles, and a simulated Stirling heat collector with liquid cooled heat rejection. Not shown in the figure, is the insulation wrapped around the heat source, used to minimize heat loss to the environment. The test articles included different combinations of metallic and ceramic parts required for the heat flux measurement in the Stirling application. These results suggest the substrates have an adequate compressive strength for the intended application. Some substrates selected for test contained hairline cracks. Those substrates did not change during the test, suggesting hairline cracks do not pose a significant risk to crack propagation in the substrate under those thermal and mechanical loads.

The ceramic substrates were tested using an average temperature change rate of 0.5 °C/sec. The rate tested provides a 100% margin over the 0.25 °C/sec expected in Stirling testing. Values as high as 1.5 °C/sec were experienced during transients but only for a few seconds. These results suggested the ceramic disks had adequate resistance to thermally induced stresses which may occur while the Stirling convertor is being heated up or cooled down. Appendix Table A-2 shows the resulting test temperatures.

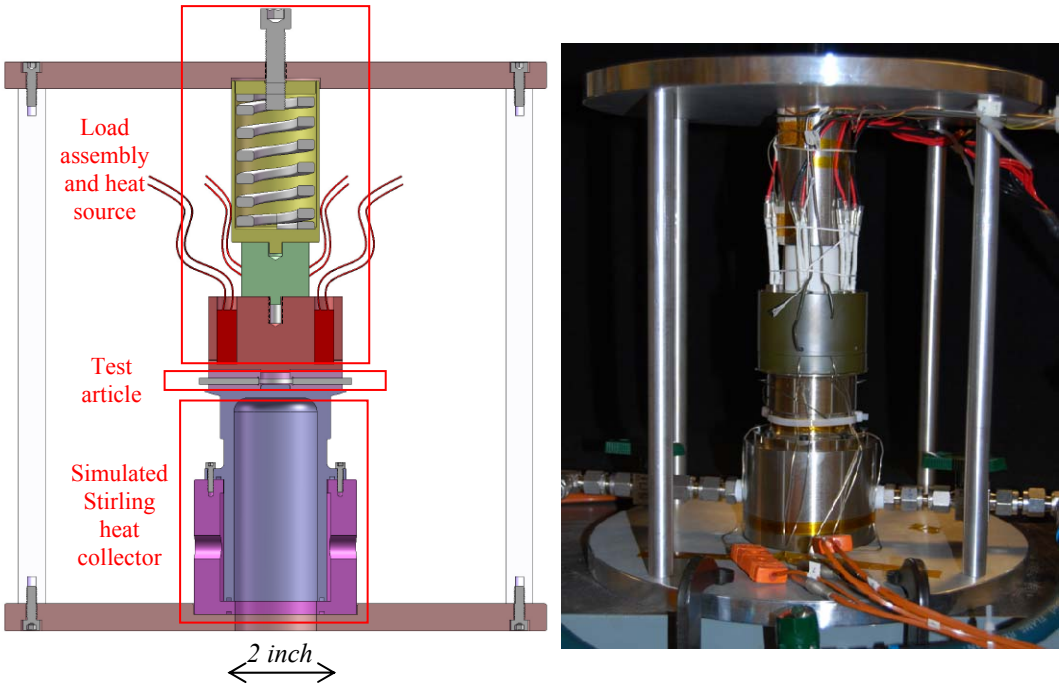

Figure 28. Robustness Test Rig

The nickel spacer disks appeared unaffected by mechanical loading. A layer of aluminum oxide was deposited onto the nickel spacers to electrically insulate the thermocouple array present on the sensor. These thin layers of aluminum oxide are expected to also provide protection against chemical reactions or gold and platinum diffusion into the mating nickel interface. The gold, platinum, and platinum/rhodium thin metallic films were present on the ceramic substrate on Sample 6 before testing. These films were damaged in some areas on each side of the sensor. It appeared that the surface flatness on the nickel spacer was not adequately controlled, which resulted in damage to the thin-film thermocouples. Figure 29 shows the gold and platinum films that had been either compressed or diffused into to the nickel spacers.

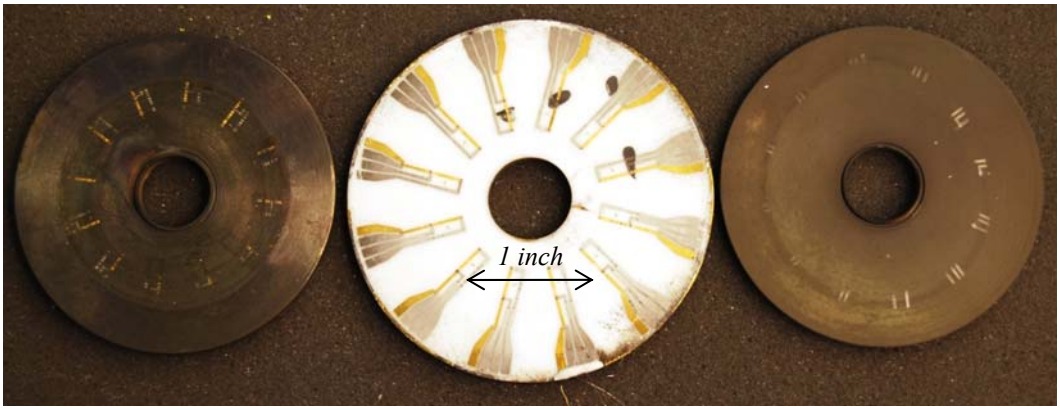

Figure 29. Au and Pt Adhesion or Diffusion onto Nickel Spacer.

Table A-2 shows test data collected from six different combinations of ceramic sensor disks and metallic and ceramic spacer materials. Sample Sets #3 and #6 best represented the target application. The difference in contact resistance between the two tests was almost a factor of 2. The Mullite substrate test, Sample Set # 2 resulted in double the temperature drop compared to the Alumina test, Sample Set #5, but this is expected because the thermal conductivity is nearly twice as high for the Alumina.

Component testing identified the need to control the spacer geometry more closely, namely surface finish and flatness, in order to minimize contact resistance and prevent rough surfaces from damaging the thin films on the sensor. The nickel spacers were used to provide locating features for the sensor relative to the heat collector and heat source and to evenly distribute heat transfer from the heat source to the sensor.

CHAPTER III

CHARACTERIZATION

While the trials and tribulations of fabrication progressed, one sensor, containing a single working thermocouple junction, was provided for initial testing. To get the temperature to read out in the data collection rack, a scheme was constructed to convert measured sensor output voltage to temperature.

3.1 Signal Processing in LabVIEW

The LabVIEW interface software module was constructed by Nissim Lugasy (ASRC Aerospace Corp.) in GRC's Thermal energy Conversion Branch. Before it was programmed, it was constructed using a model programmed by the author. This aided the LabVIEW programming effort and provided a way to validate LabVIEW. The model converted the sensor thermocouple *emf* voltages into temperatures used to calculate heat transfer. The *emf* voltage signals feed out from the sensor through the small-diameter

noble metal wires to a custom-made wire feed through mounted in the insulation enclosure. The small-diameter noble metal wires were soldered to the copper feed through wires. These soldered junctions represent the cold junction of the circuit. Cold junction compensation is necessary because the Seebeck Coefficient is different for the length of the thermocouple represented by the noble metal wires and the length of the thermocouple represented by the copper extension wire. Normally, cold junction compensation is performed in modern thermocouple measurement electronics present in most data acquisition systems. Since the cold junction is located on the inside of the insulation enclosure, the cold junction was expected to operate at roughly the rejection temperature of the Stirling convertor.

In general, to perform cold junction compensation, the cold junction temperature is measured, converted to a voltage using a reference function, added to the sensor output voltage, and finally converted back to a temperature using a different reference function.[13]

The reference temperature measurement is required at the intermediate junction, referred to as the cold junction, between the noble metal wire and the extension wire used to pass the signal long distances. Extension wire is used to prevent the need for long lengths of expensive noble metal wire. Two Type-T reference thermocouples were installed in the custom-made wire feed throughs in order to accurately measure the cold junction reference temperature. The cold junction temperature was converted to a voltage using the Au vs. Pt reference functions produced by National Institute of Standards and Technology (NIST). The NIST reference functions, shown in the Appendix, were developed during a calibration effort at NIST which quantified the stability and

reproducibility of Au vs. Pt wire thermocouples.[14] In that effort, small-diameter Au vs. Pt wire thermocouples were subjected to thermal shock from 960 °C to room temperature 112 times during 1,000 hours of operation. The resulting equivalent temperature changes of the thermocouple at the freezing point of silver did not exceed ±16 m°C. Further, the mean values of emf voltage obtained at full immersion for six Ag freezes were identical to within the equivalent of 1 m°C.

The function which converts temperature to voltage, represented by Table A-3 and the corresponding Seebeck Coefficient, for Au vs. Pt thermocouples, are shown in Figure 30. Functions represented by Appendix Tables A-3, A-4 and A-5, shown in Figure 31, convert voltage to temperature but Table A-4 is only applicable from 0 to 209 °C while Table A-5 is suggested for use between 209 and 1,000 °C. Only Table A-5 was programmed in the DAS because it is satisfactory for use in this Stirling application from 0 and 1,000 °C. This was justified since the difference between it and Table A-3 is only 6 °C at room temperature and almost negligible at around 150 °C, as shown in Figure 31. Figure 32 shows how the function from Table A-4 is not useful above 150 °C.

The output available from Au vs. Pt thermocouples ranges from 6 to 17,000 μV while the thermocouple signal strength expected during steady state operation in the Stirling application ranges from 8,000 to 12,000 μV. Similarly, the total output resolution, or Seebeck Coefficient, ranges from 6 to 25 μV/°C while the output resolution expected during steady state operation in the Stirling application ranges from 18 to 24 μV/°C.

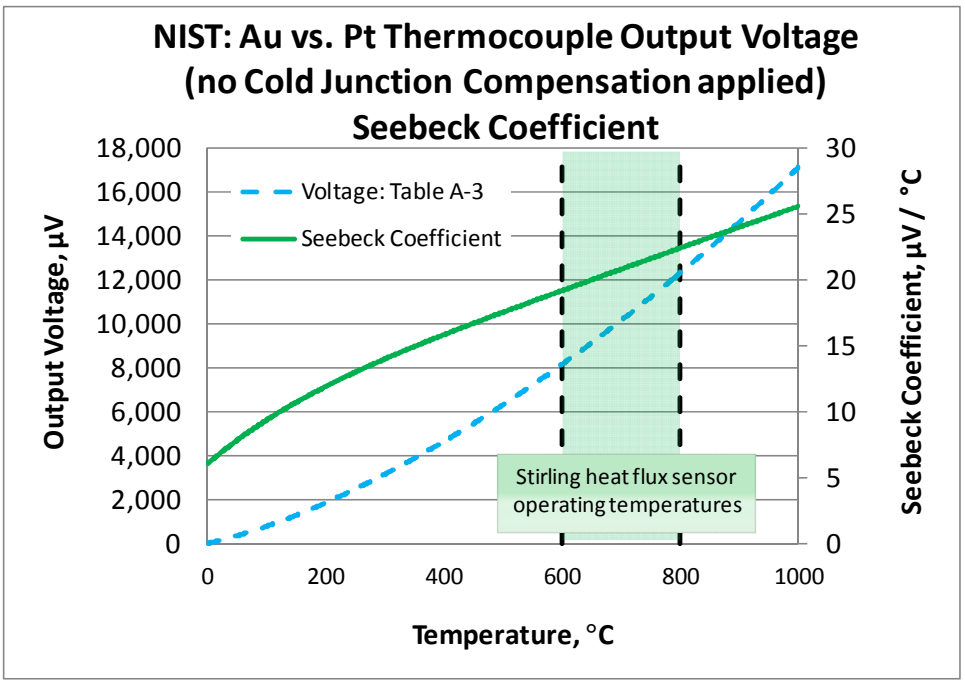

Figure 30. Output Voltage (Table A-3) and Seebeck Coefficient.

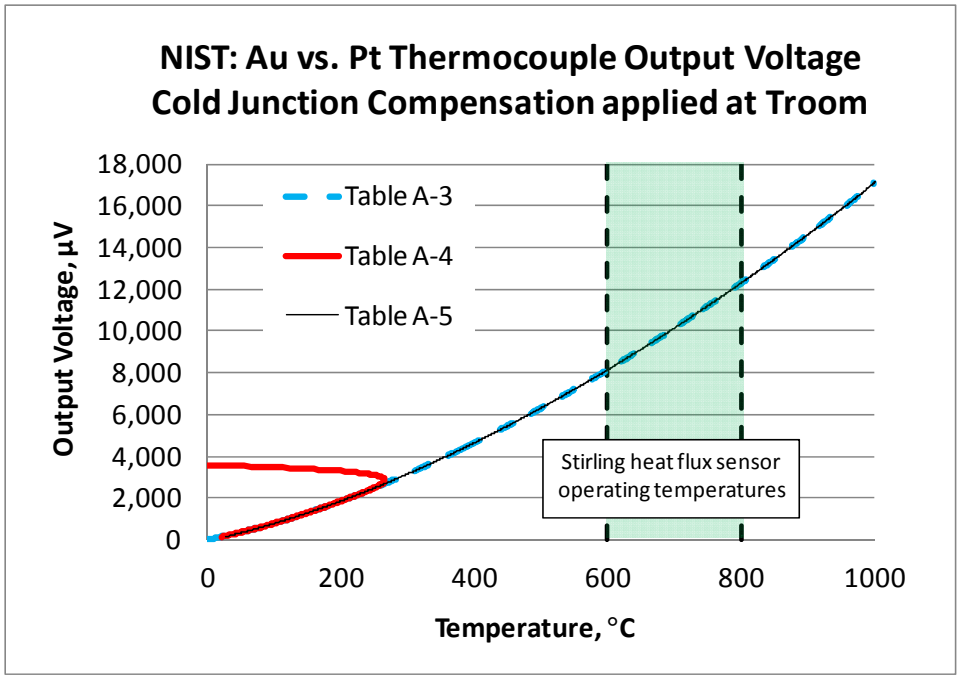

Figure 31. NIST Calibration Tables shown in Appendix.

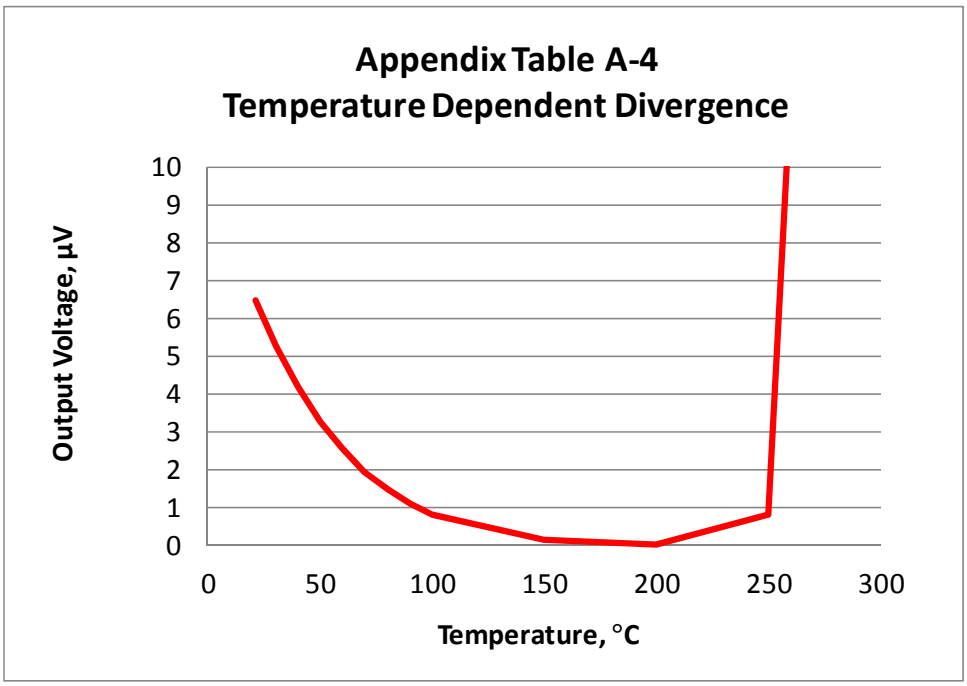

Figure 32. Appendix Table A-4 Temperature Dependent Divergence.

The cold junction compensation procedure is summarized below.

1. Record sensor voltage from Au-Pt thin-film thermocouple
2. Record cold junction temperature from reference thermocouple
3. Convert the cold junction temperature to a reference voltage using Table A-3
4. Add cold junction reference voltage to sensor voltage to get hot junction voltage
5. Convert the hot junction voltage to hot junction temperature using Table A-5

After the voltages were converted to temperatures, the heat flow was calculated using tailored variations of Eq (2). Heat flow was calculated locally and was averaged to compare local and average heat transfer value through the ceramic disk. The physical dimensions, namely disk area and thickness, and thermophysical properties like thermal conductivity are used to calculate heat flow. Appendix Figures A-1 and A-2 show the temperature dependent thermal conductivity for Alumina, based on Appendix Table A-1, and nickel 201 based on the typical values found in the literature.

3.2 Bench Top Test

Bench top tests were performed at GRC to characterize the repeatability and stability of the Au vs. Pt thin-film thermocouples fabricated at GRC and to test the proposed data acquisition process. The bench top test setup graphic and photo, shown in Figure 33, includes (1) a thin-film Au vs. Pt thermocouple deposited on an Alumina substrate (used as the test article), (2) a Au vs. Pt 0.003 inch diameter wire thermocouple located directly on top of the thin-film thermocouple via ceramic paste (used as the reference thermocouple), and (3) a Minco mica heater (used to heat the test setup). The test setup was insulated using Kaowool fiber insulation and the noble metal thermocouple wires were joined to the copper extension wire to create the cold junction. The connections were made using an electrically conductive epoxy (BIPAX TRADUCT BA-2902). The resistance measured < 7 ohms across the leads at the Agilent, making the connections made using the electrically conductive epoxy essentially equal in performance to connections made with parallel gap welding. A Type-K thermocouple was used to measure the cold junction temperature. Before the insulation was installed, the dc *emf* voltage was measured across the test sample thin-film thermocouple junction. The baseline room temperature reading was 2-3 μV. The reading quickly increased to 9 μV in less than one second, when a breath of hot air was blown onto the junction and slowly decreased back to 2-3 μV over about 5 seconds. Figure 34 shows (A) the Minco mica heater near the heated zone of the gold versus platinum thermocouple test sample, (B) the Minco mica heater in position under a layer of Kaowool insulation, and (C) the test setup, featuring the Agilent 34401A, 6 ½ Digit Multimeter used to measure the

sensor *emf* output in micro volts and the Agilent used to measure heater current and voltage.

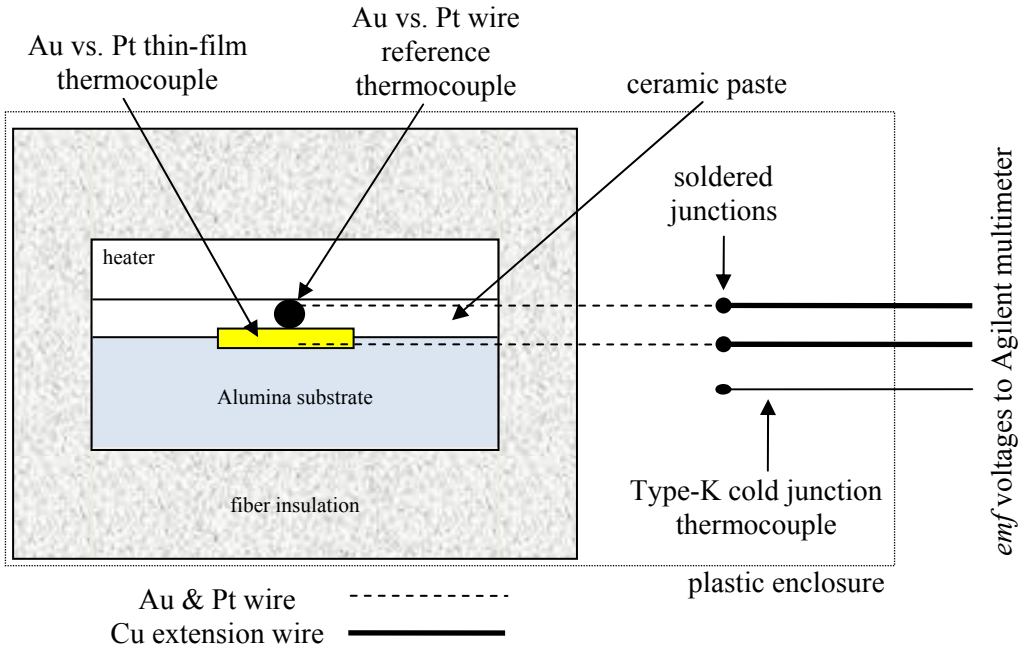

Includes a thin-film Au vs. Pt thermocouple, Au vs. Pt wire thermocouple, and heater.

Figure 33. Diagram and Photo of Bench Top Test Setup.

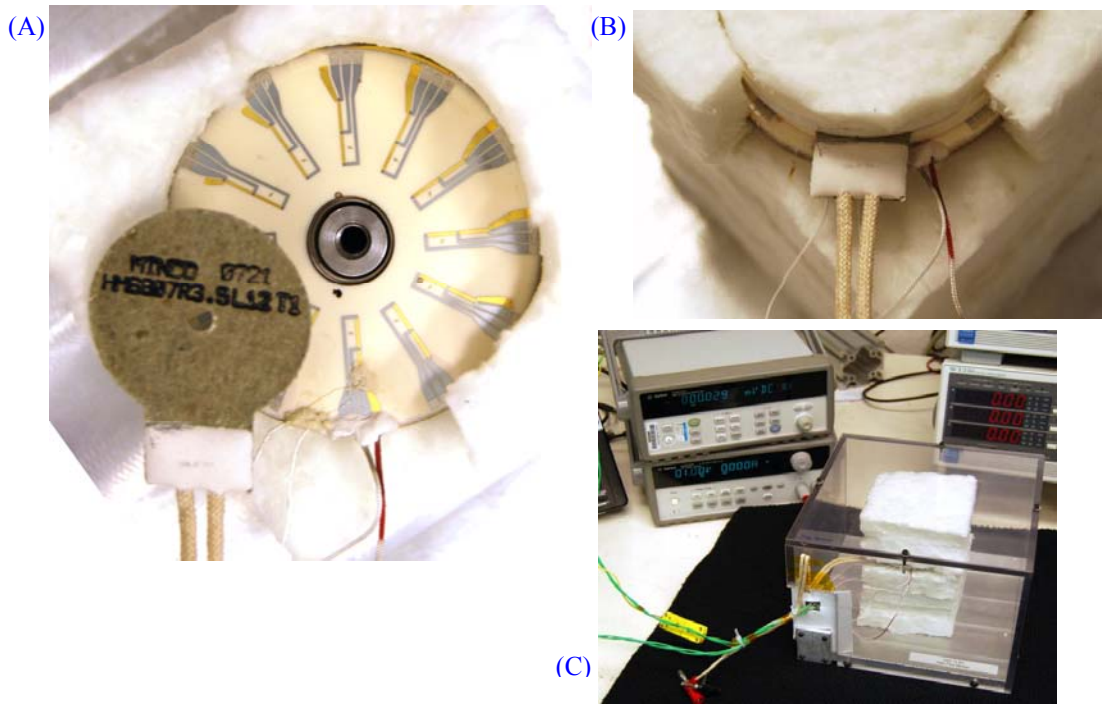

Figure 34. Additional Photos of Bench Top Test Setup.

Two characterization tests were used to measure *emf* voltage output of the thin-film thermocouple as a function of a reference temperature. The first characterization study was a transient test, used to characterize the repeatability of the thin-film thermocouple. A power supply powered a flat Minco mica heater to increase the test sample temperature. A computer program was commanded, by Nissim Lugasy, to repeatedly cycle the temperature of the test article from 50 to 450 °C, the peak temperature being limited by the available heater. The test article was then allowed to cool down to 50 °C before another thermal cycle was automatically performed. These test conditions were used to subject the test article to 15 thermal cycles. Figure 35 contains the resulting *emf* voltage plotted against time for all 15 thermal cycles.

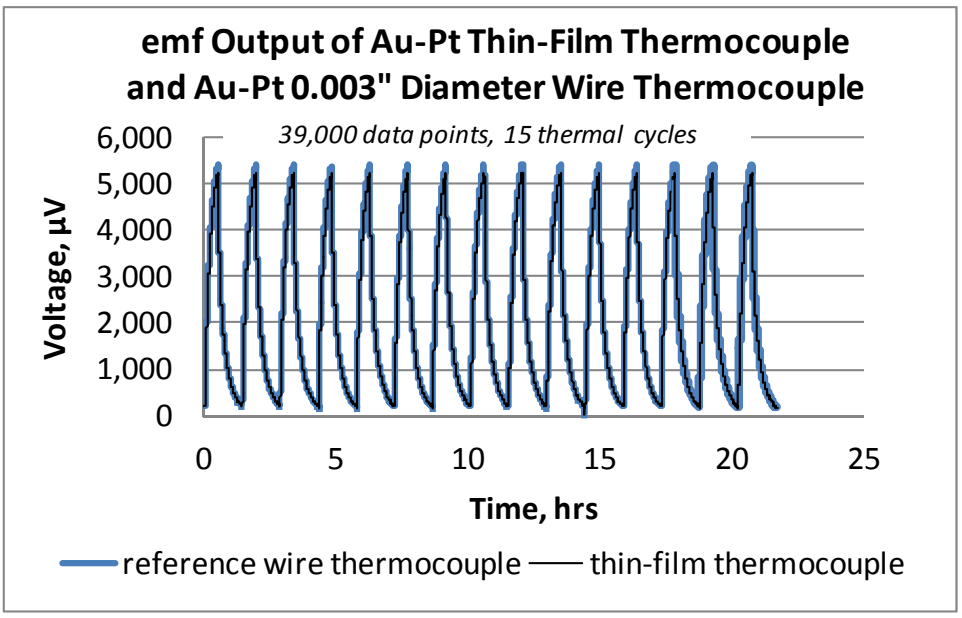

Figure 35. Thin-film Thermocouple *emf* Voltage Output versus Time.

Throughout each thermal cycle, LabVIEW was commanded to record the *emf* voltages at a scan frequency of 2 seconds. The *emf* voltages from both thermocouples were then converted to temperature using the NIST reference functions and the cold junction temperature. Figure 36 contains the resulting *emf* voltage plotted against reference temperature for all 15 thermal cycles. The reference temperature was measured by a 76 µm diameter Au/Pt thermocouple.

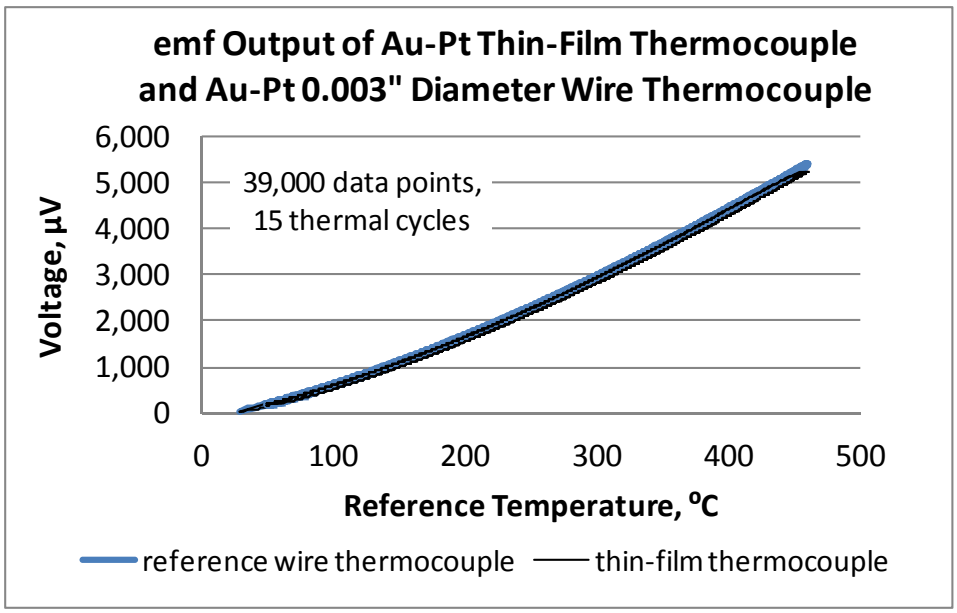

Figure 36. Thin-Film Thermocouple *emf V*oltage Output versus Ref. Temperature.

There was a maximum temperature difference of 9 °C between the thin-film and reference thermocouple, likely due to the reference thermocouple's closer proximity to the heater compared to the thin-film sensor and partly due to the thermal resistance of the ceramic paste used to fix the reference thermocouple onto the thin-film sensor. With heat flowing from the heater to the thin-film sensor, one would expect a temperature gradient in the direction of the heat flow.[15]

The data suggests that the repeatability of the thin-film sensor and the reference thermocouple are at least grossly equal. Additional calculations were performed to explore how similar they were statistically. The sensor temperature data were synchronized using the 2-second data files for 15 thermal cycles. The data were synchronized by setting data point #1 using the 2 second data file when the heater was first powered, indicated by the voltage changing from 0 V to 10 V. Those synchronized sensor temperatures were used to calculate the median and standard deviation. Figure 37

shows the standard deviation based on cycle-to-cycle variation for the test temperatures recorded. The peak standard deviation for all 15 cycles was of 2.3 °C and for only 13 of 15 cycles was 0.6 °C.

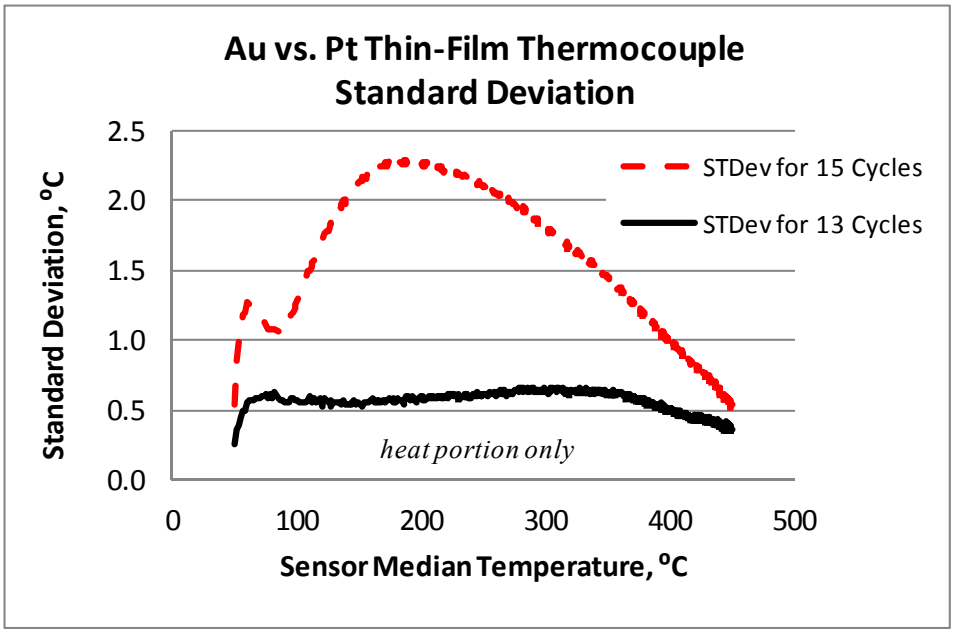

Figure 37. Standard Deviation for Thin-Film Thermocouple Output.

Cycles 5 and 11 were not included due to the inability to synchronize the starting point. They were different due to an unexpected higher heat input when the heater was first powered on. Upon inspection of the data, it was noticed that the computer program controlling the thermal cycling test was erroneously stopped and the previous thermal cycles (cycles 4 and 10) were allowed to cool to a slightly lower temperature than desired before being restarted. This caused the next heating cycle to need additional heat input and a corresponding higher rate of temperature increase compared to all other cycles when the heater was powered on. For that reason, cycles 5 and 11 were omitted for the

calculation of absolute deviation. Also excluded were the cooling portions of each cycle because, while the heater controller performed very consistently, the cooling rate was not as consistent from cycle to cycle. Overall, 13 heating cycles were compared.

The absolute deviation did not exceed 2 °C for 13 heating cycles (18,000 data points). The absolute deviation of the sensor temperature is the absolute difference between the sensor temperature and the median. This value, calculated at each 2-second interval, compares how different the temperatures were from the median for 13 heating cycles at each time interval. In addition to variations in sensor output, this calculation measures how consistent the heating cycles were controlled from one cycle to another. This did not turn out to the best way to show repeatability because of the inherent combination of measuring both controller and sensor output repeatability.

The second characterization study was a steady-state test used to characterize the stability of the thin-film thermocouple. The test setup maintained a steady-state temperature of 495 °C (heater temperature limit). Throughout the test, LabVIEW was commanded to record the emf voltages at a scan frequency of 2 seconds. The emf voltages from both thermocouples were then converted to temperature using the NIST reference functions and the cold junction temperature. Figure 38 shows the temperature data from the thin-film and reference wire thermocouple. The maximum temperature variation was about 0.2 °C, mostly because the temperatures were still slowly increasing. Plotting the same data over only ten minutes results in about 0.1 °C variation. This variation was on the order of what was expected from a Au vs. Pt thermocouple.

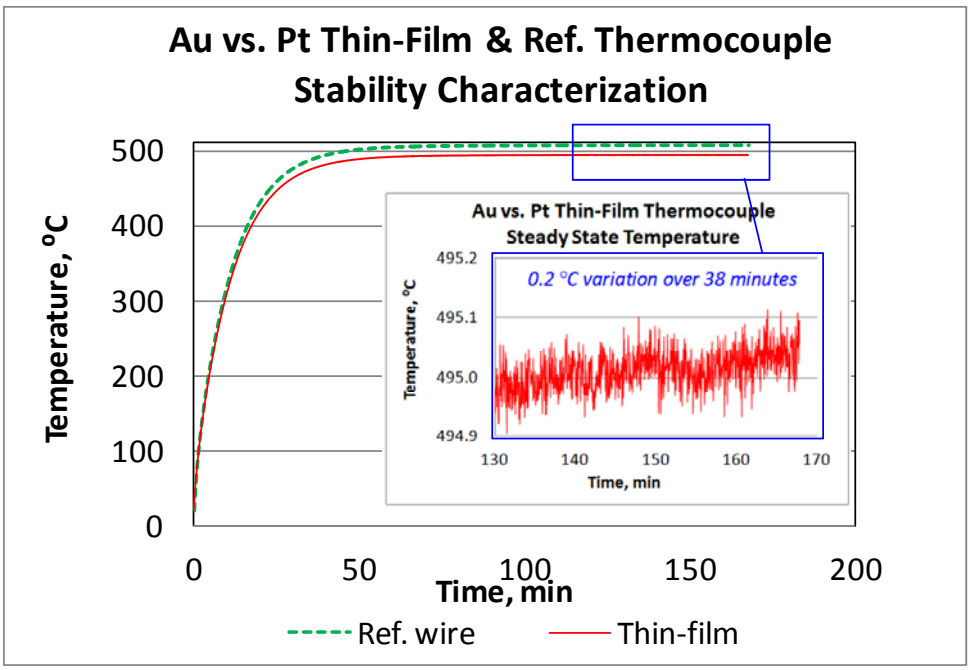

Figure 38. Au vs. Pt Thin-Film & Ref. Wire Thermocouple Test Temperatures.

CHAPTER IV

INTEGRATION AND INSTALLATION

Recording the heat flux measurements in the data acquisition system (DAS) involved two main tasks, integration and installation. Integration was carried out by programming the cold junction compensation and NIST calibration functions into the DAS and ensuring all of the signals in the final sensor assembly were operational using the Agilent data logger. Recall that cold junction compensation is required when the transition from noble metal wires to extension wires, the cold junction, is at an elevated temperature. For this application, the cold junction temperature averaged 53 °C and 55 °C on ASC-E #1 and ASC-E #4, respectively. In addition to doing cold junction compensation, the algorithm had to account for the use of the nonstandard thermocouples by providing the NIST calibration tables for converting voltages to temperatures and vice versa for the Type-T cold junction temperature measurement.

The heat flux sensor LabVIEW scheme, used to characterize the sensors during bench top testing, was integrated into the existing software environment planned for monitoring the convertors during operation. The LabVIEW module was programmed with a scan rate of 5,000 samples/sec. The Agilent scan frequency was slowed down to scan 32 channels every 0.1 second so to not to overwhelm the LabVIEW module reading the signal into the DAS. A filter was used in the conversion of voltage to temperature in order to filter out erroneous output voltages that occurred on a regular basis. These anomalous signals are discussed in the next chapter.

4.1 Sensor Installation

After the cold junction compensation and NIST calibration tables had been programmed into the DAS, the final assembly was tested using the Agilent data logger. Figure 39 shows the finished sensor wired up to the multiplexer card for use in the Agilent data logger. When this step was performed on Sensor 2, a gold leg was found to have failed since the initial delivery. Sensor 2 had been delivered with one failed gold junction so an additional failed common leg rendered the sensor unable to measure heat flux on one entire station. This indentified the issue of low bond strength between the gold films and Alumina substrate. The work performed to mitigate this issue is discussed in the conclusions. Table III shows the D-subminiature connector pin-out diagram used to connect the extension wire to the Agilent and Figure 40 shows a graphic to complement the table.

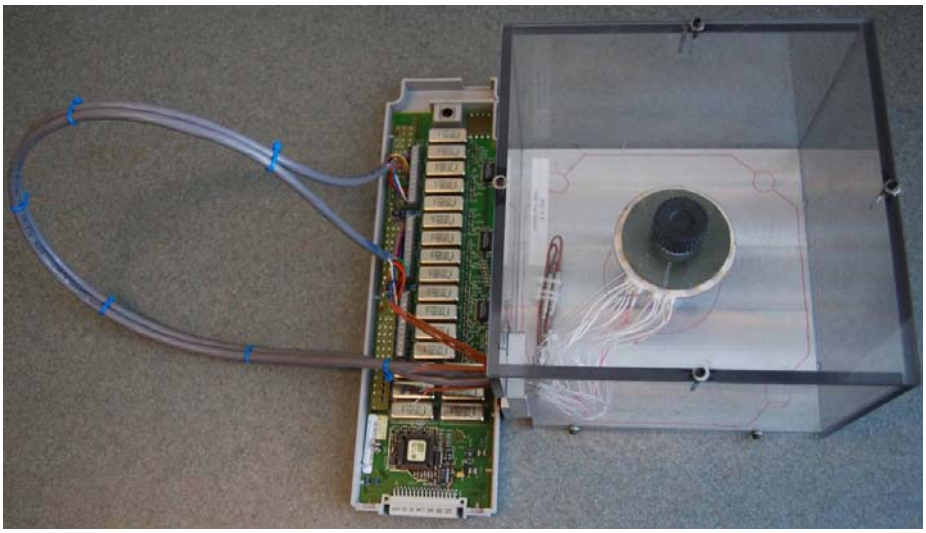

Figure 39. Completed Sensor & Spacer Assembly Wired to Agilent Multiplexer Card.

Table III. Heat Flux Sensor Feed Through Wiring Diagram, ASC-E #1 and #4.

pin	ID	Station	color	card sign	card channel	TC Leg & sign
1	S1T_J1	**1**	pink	Low	1	Pt-negative
2	S1T_J2	**1**	black	Low	2	Pt-negative
3	S1T_J3	**1**	tan	Low	3	Pt-negative
4	S1B_J4	**1**	green	Low	4	Pt-negative
5	S1B_J5	**1**	orange	Low	5	Pt-negative
6	S1B_J6	**1**	white	Low	6	Pt-negative
14	S1T_C	**1**	gray	High	1	Au-positive
15	S1T_C	**1**	purple	High	2	Au-positive
16	S1T_C	**1**	yellow	High	3	Au-positive
17	S1B_C	**1**	brown	High	4	Au-positive
18	S1B_C	**1**	red	High	5	Au-positive
19	S1B_C	**1**	blue	High	6	Au-positive
7	S2T_J7	2	pink	Low	7	Pt-negative
8	S2T_J8	2	black	Low	8	Pt-negative
9	S2T_J9	2	tan	Low	9	Pt-negative
10	S2B_J10	2	green	Low	10	Pt-negative
11	S2B_J11	2	orange	Low	11	Pt-negative
12	S2B_J12	2	white	Low	12	Pt-negative
20	S2T_C	2	gray	High	7	Au-positive
21	S2T_C	2	purple	High	8	Au-positive
22	S2T_C	2	yellow	High	9	Au-positive
23	S2B_C	2	brown	High	10	Au-positive
24	S2B_C	2	red	High	11	Au-positive
25	S2B_C	2	blue	High	12	Au-positive
13	empty					

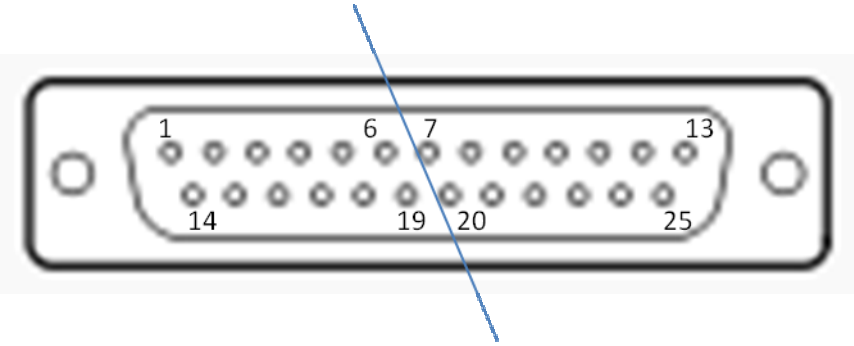

Figure 40. Miniature D-Sub Wiring Diagram.

Table IV shows the data recorded during a test used to determine individual junction functionality after the finished sensors were connected to the Agilent data logger multiplexer card. All sensors were delivered with some open junctions. Sensor 2 was the only sensor to experience film failures after being delivered but before installation.

Table IV. Pre-Installation Resistance Measurements.

Sensor	T_{room} = 21 °C	Sensor #1 (used on ASC-E #4)	Sensor #2 (not used)	Sensor #3 (used on ASC-E #1)
Junction	D-sub pin combo	Resistance, Ohms	Resistance, Ohms	Resistance, Ohms
1	1-14	7.3	8.1	Delivered open
2	2-15	6.3	6.8	Delivered open
3	3-16	5.5	6.0	4.7
4	4-17	7.7	7.1	6.9
5	5-18	6.8	6.1	6.0
6	6-19	5.8	6.0	5.2
7	7-20	7.8	**Failed**	8.1
8	8-21	Delivered open	**Failed**	6.5
9	9-22	5.6	**Failed**	5.3
10	10-23	7.9	Delivered open	6.5
11	11-24	7.1	Delivered open	6.5
12	12-25	5.7	Delivered open	5.5

Reference: T_{room} = 21.1 °C

With integration tasks complete, installation was carried out by installing the sensors into the Stirling support hardware. The support hardware, designed to hold the ASC-E's during testing, did not initially include provisions for a heat flux sensor. Several aspects of the design had to be revised to include features for holding the sensor and wires and feeding wires through structural supports that would encase the micro-porous insulation and an inert gas environment. Installation of the sensors into the ASC-E #1 and #4 test setup involved performing tasks to: (a) ensure that the existing support hardware design could incorporate the relatively high temperature drop across the ceramic substrate, (b) connect noble metal wires to less expensive extension wire, and (c) fabricate custom-made wire feed throughs which enabled sending wires through the enclosure and connection to the test stand. Additional thermocouples were added before the sensor wire connections were completed. The desire to collect reference temperatures lead to the inclusion of 1/32 inch diameter Type-N thermocouple probes located in the nickel spacers. Figure 41 shows the two thermocouples located in the top spacer. Also shown less clearly are the two lower thermocouples located in the bottom spacer.

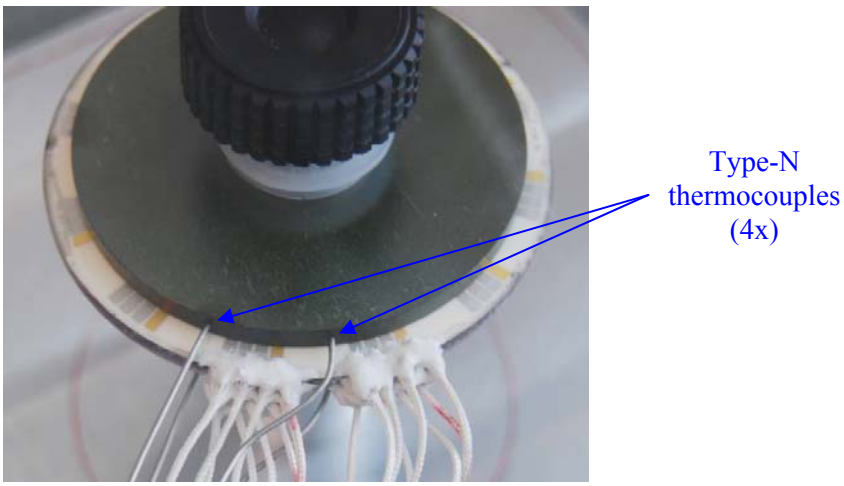

Figure 41. Type-N Thermocouples (4x) in Nickel Spacers.

4.2 Test Setup Assembly

The convertors were installed onto the enclosure base with one vertical wall installed. Microporous insulation Parts A, B, and C were installed and the CSAF and hot-end thermocouples were routed to a separate D-sub connector, shown in Figure 42 (A). The caption for each component installed during the assembly process is highlighted with red text in Figures 42 through 44. The heat flux sensor installation was a delicate process where the sensor was lowered into position by using forceps to hold the inner diameter of the ceramic substrate. Great care was given to minimizing the distance of travel from the holding fixture to the convertor heat collector.

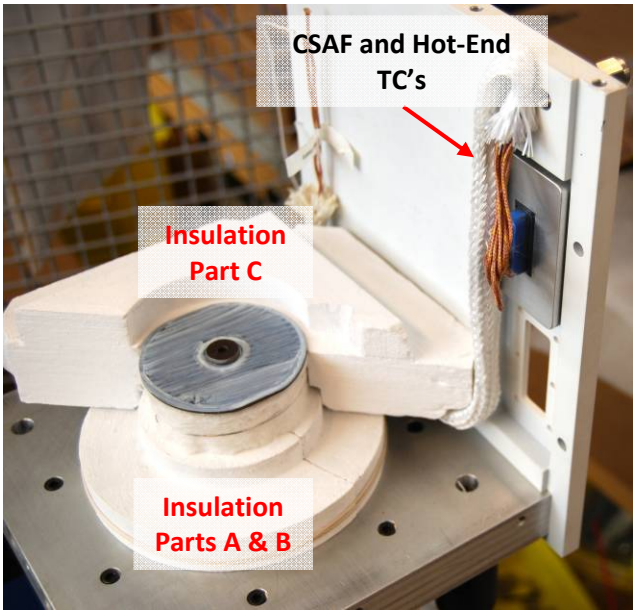

(A) ASC-E #1 with microporous insulation.

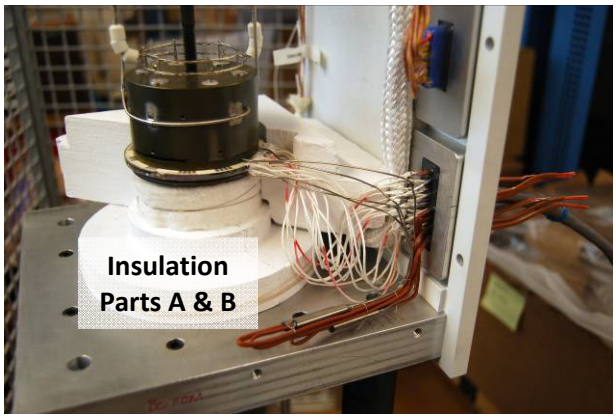

(B) Heat flux sensor installed (sensor wires not bundled) and heat source fit check.

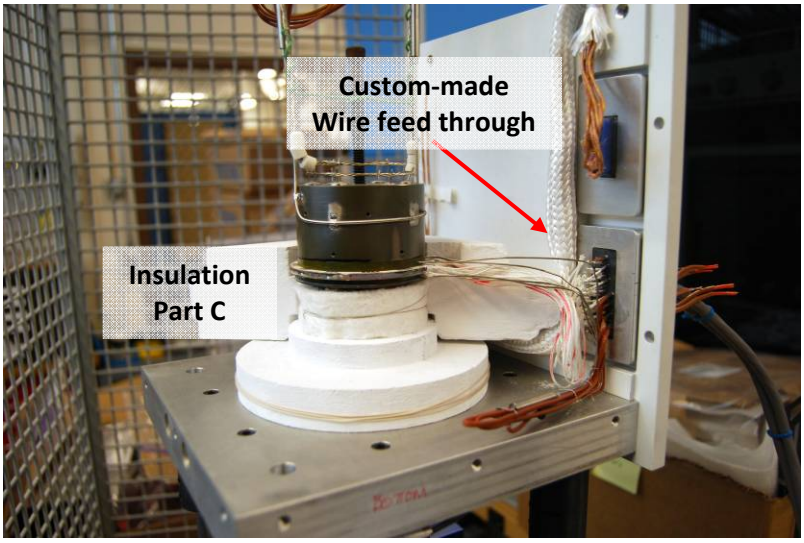

(C) Heat flux sensor installed (sensor wires bundled) and heat source fit check.

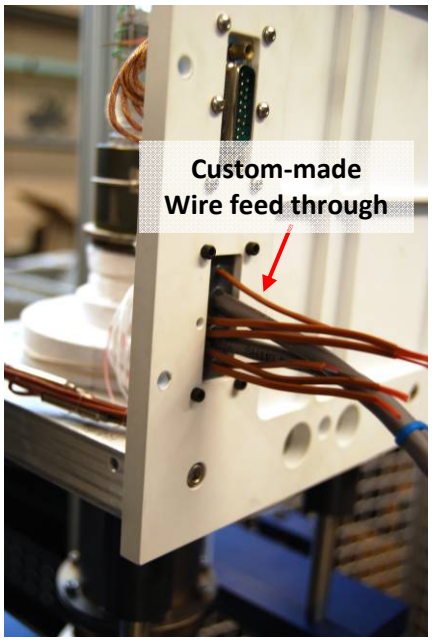

(D) Exterior view of custom-made wire feed through.

Figure 42. ASC-E #1 & #4 Test Setup Assembly.

Figure 42 (B) shows the sensor wires loose and unorganized and the heat source present as part of an orientation checkout. The wires were then carefully bundled together so as not put any tension on any of them, as shown in Figure 42 (C). Finally, Figure 42 (D) shows the un-terminated Type-T and Type-N thermocouples and copper extension wire feeding through the aluminum enclosure. The enclosure was originally designed and tested with an Argon environment inside of the box because Type-R thin-films were originally planned and the heat source life would benefit from the inert environment. The enclosure turned out to contain too many gross leaks, making it difficult to maintain an Argon supply over the 10,000 hours of operation. The Argon supply was replaced a few times before it was decided to drop the capability from the scope of the test. Not having the inert environment was not believed to have a significant impact on preventing oxidation of the gold or platinum films, and the nickel parts were not at high risk of oxidation due to the relatively low test temperatures.

The wire path used to protect the delicate sensor wires is clearly shown in Figure 43 (A). With Insulation Part C installed and wires routed and partially bundled, Part D was installed to create the wire path. Insulation Part E simply fit over the top, ensuring that the wires were not crushed or pinched. The wire path can be seen from a top view in Figure 43 (C) and from a side view where the wires exit through a small window in Figure 43 (D). The exit window was carefully stuffed with blanket insulation to prevent line-of-sight losses. With Insulation Part E in position, the heat source assembly was installed along with the rest of the insulation parts. Figure 44 shows the sequence in which Insulation Parts F, G, H, and I were installed. The remaining enclosure walls were installed and a mechanical load was applied to the heat source at room temperature.

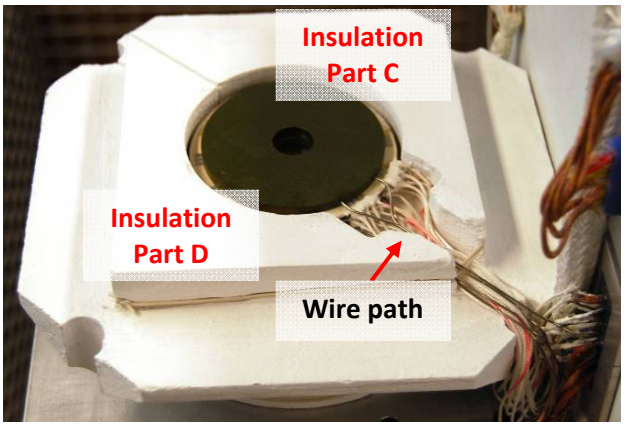

(A) Insulation Part C , Part D, and wire path.

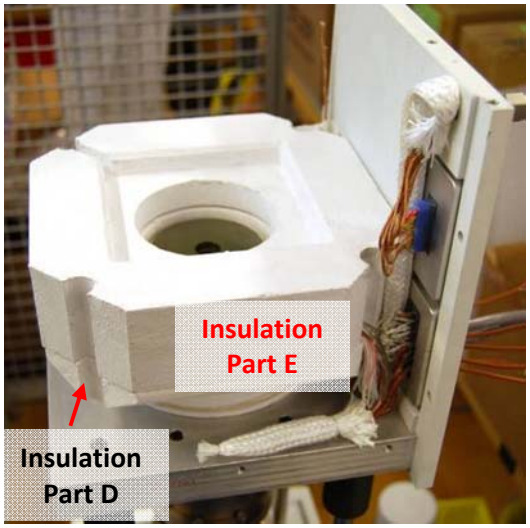

(B) Insulation Part D and Part E.

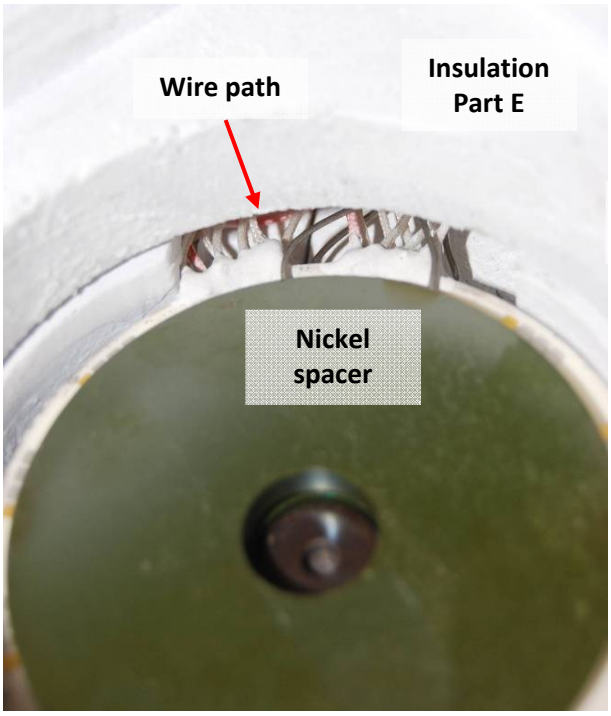

(C) Insulation Part E, wire path, and nickel spacer (between heat source and sensor).

(D) Insulation Part E and wire path exit window, later stuffed with blanket insulation.

Figure 43. ASC-E #1 & #4 Test Setup Assembly.

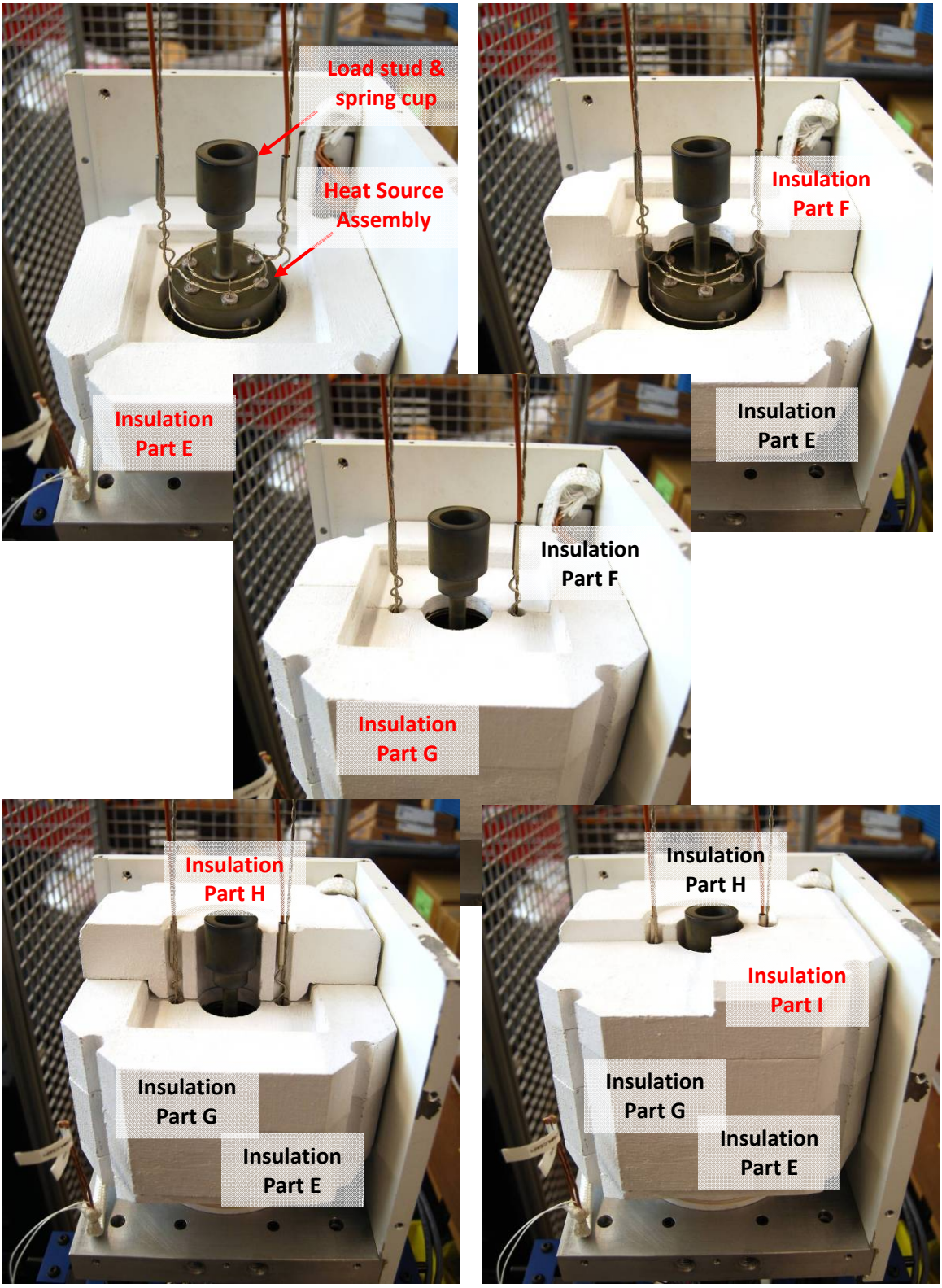

Figure 44. ASC-E #1 & #4 Test Setup Assembly.

Analytical calculations were made to predict what room temperature load would be needed to achieve the desired load at test temperatures. Table V shows the input and calculated values used to determine the necessary room temperature load needed to achieve the desired load during application. The Bellville washers used in the assembly have a nonlinear stiffness and the support structure turned out to be sensitive to thermal expansion. The desired load of 150 lb ±25 lb was achieved by using 1 ¼ turns on the load screw. This applied an 86 lb load at room temperature and 161 lb load at test temperatures. Not shown in detail are the calculations for individual components which determined the overall change in structure length due to thermal expansion (0.045 in).

Table V. Analytical Calculations for Heat Source Mechanical Load.

Bellville washer inputs	spring thickness	in	0.040
	spring free height	in	0.059
	available travel per spring	in	0.019
	number of springs		12
	stiffness for 1 spring	lb/in	20000
Load screw inputs	load stud threads per inch		24
	deflection per turn	in	0.0417
Room temp (1 spring)	deflection needed for 1 spring	in	0.0043
Room temp (12 springs)	stiffness for spring stack	lb/in	1,667
	deflection needed for spring stack	in	0.052
	resulting load for spring stack	lb	**86**
Test temp (12 springs)	change in structure length due to thermal expansion	in	0.045
	deflection for spring stack w/ thermal expansion	in	0.097
	resulting load for spring stack w/ thermal expansion	lb	**161**
Statistics	increased load due to thermal expansion	lb	75
	ratio of thermal expansion to required room temp deflection	%	87%
	number of turns on preload stud		1.24

CHAPTER V

TESTING

After the sensors were installed into the test setup, steps were taken to ensure that the data being steamed from the Agilent data recorder to LabVIEW was being processed and captured correctly. The sensor output was recorded during convertor insulation loss testing, a test performed to enable 1st order prediction of heat lost to the environment during operation. Figures 45 through 47 provide a measure of functionality for each sensor. Figure 45 shows each junction's temperature measurement at a single 2-sec data record for each test temperature. During the test, the convertor hot-end temperature was maintained over a test period at each of the following temperatures: 350, 450, 550, and 650 °C. The test was static (no piston motion) so there was no heat flowing to the Stirling cycle. Heat was only transferred to the rejector due to parasitic heat losses made up of solid and gas conduction and radiation.

ASC-E #1's sensor was delivered with Junctions 1 and 2 open so it was surprising to see both junctions fully functional. Junction 7, noted as functioning during the previous checkout test, did not report a temperature for the first two test points and then started functioning on the last two test points.

ASC-E #4's sensor was delivered with Junction 8 open so it was not unusual to find that junction inoperative. Figure 46 shows the test temperatures throughout the hot region of the test setup for each convertor throughout insulation loss testing, with the above mentioned junctions omitted (J7 on E#1 and J8 on E#4). Figure 47 shows the superimposed test temperatures for the 650 °C operating point onto the hot region of the setup. The white and green data points represent averaged wire probe thermocouple and thin-film thermocouple measurements. The data was used to determine that most junctions initially operated within the expected temperature range.

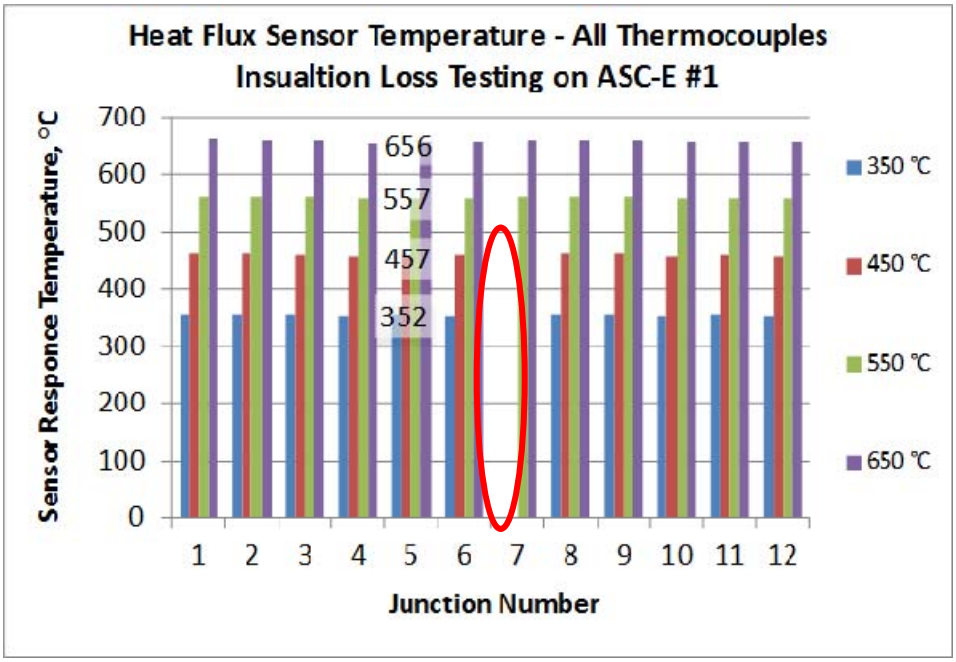

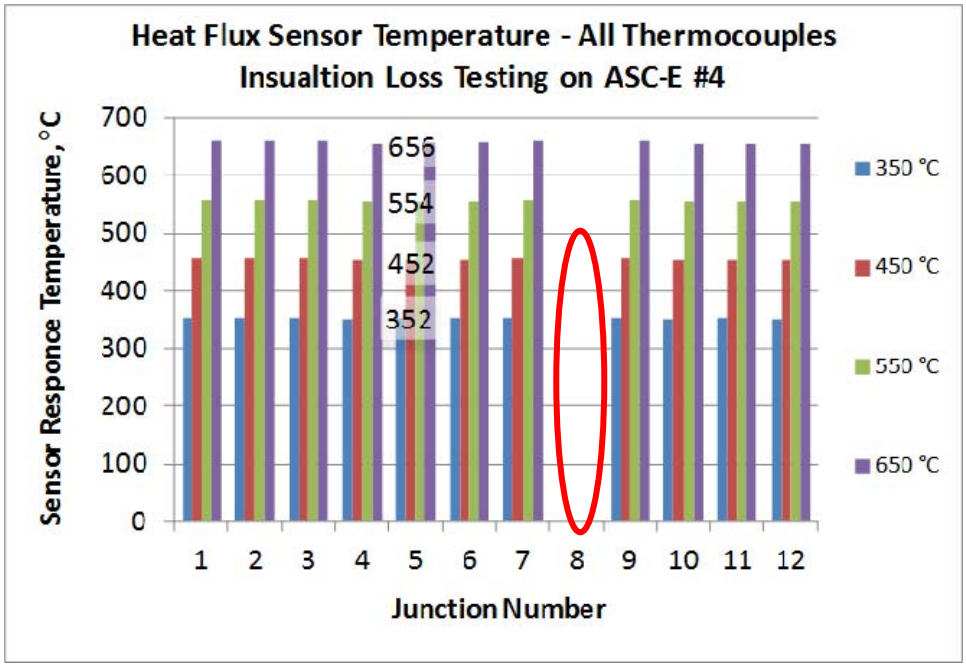

Figure 45. ASC-E #1& #4 Insulation Loss Test Data.

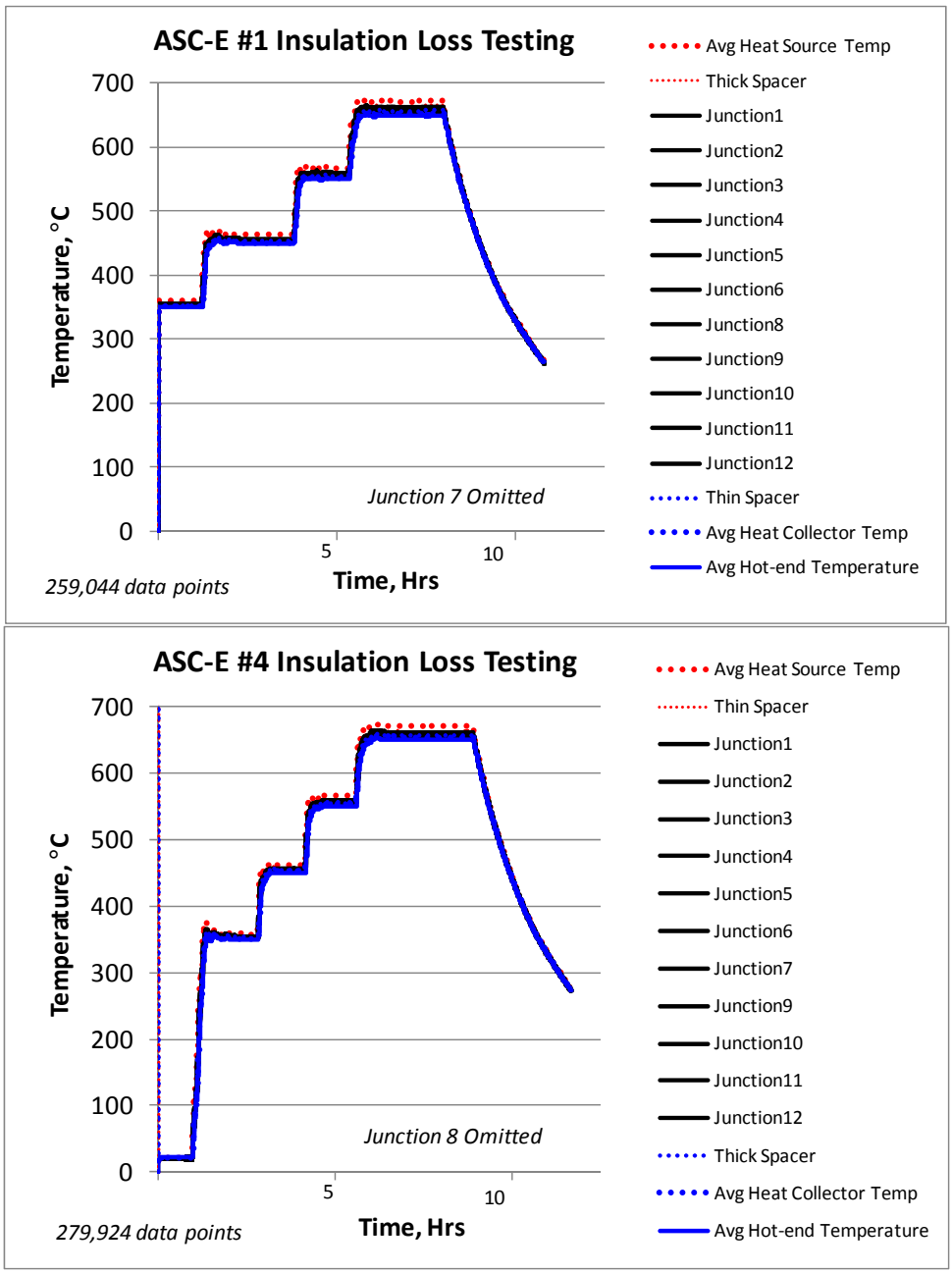

Figure 46. ASC-E #1 & #4 Insulation Loss Test Data, 2-sec Data Shown.

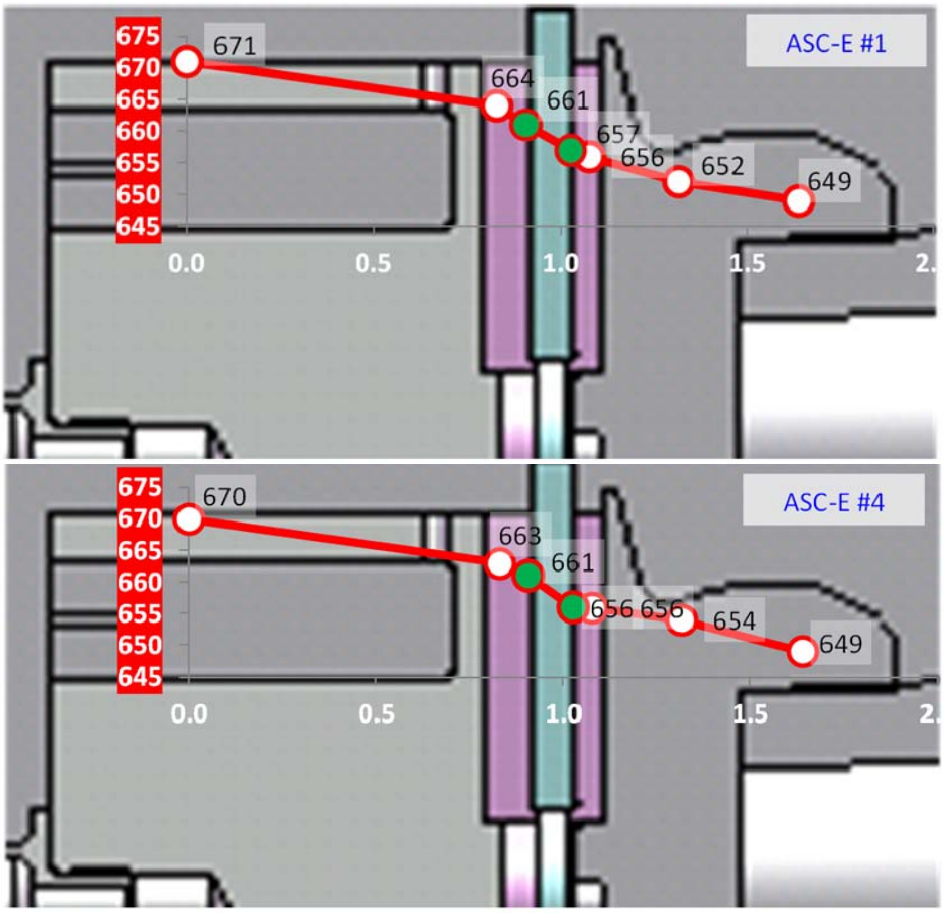

Figure 47. ASC-E #1 & #4 Measured Temperatures for 650 °C Insulation Loss Test.

5.1 Data Reduction and Calculations

The calculation for heat transfer from the heater to the Stirling was represented by an average heat flow through the thickness of the ceramic substrate. This formulation is described below. The nomenclature is based on the thermocouple numbering scheme shown in Figure 48. Figure 48 (A) shows the thermocouple junctions located on each side of the disk that enable the measurement of temperature difference. The pattern contains junctions located at key locations to enable measurement of a temperature gradient on each disk face, including at three different radii, shown in Figure 48 (A) and (B), and at two key circumferential locations. The radial locations were intended to quantify a

temperature gradient from center to edge of the disk, with the medium radius (r2) located directly under the cartridge heater. This was not possible because the design of the heater block was changed during the fabrication stage of the photolithography process. This resulted in two, evenly spaced junctions located under a cartridge heater.

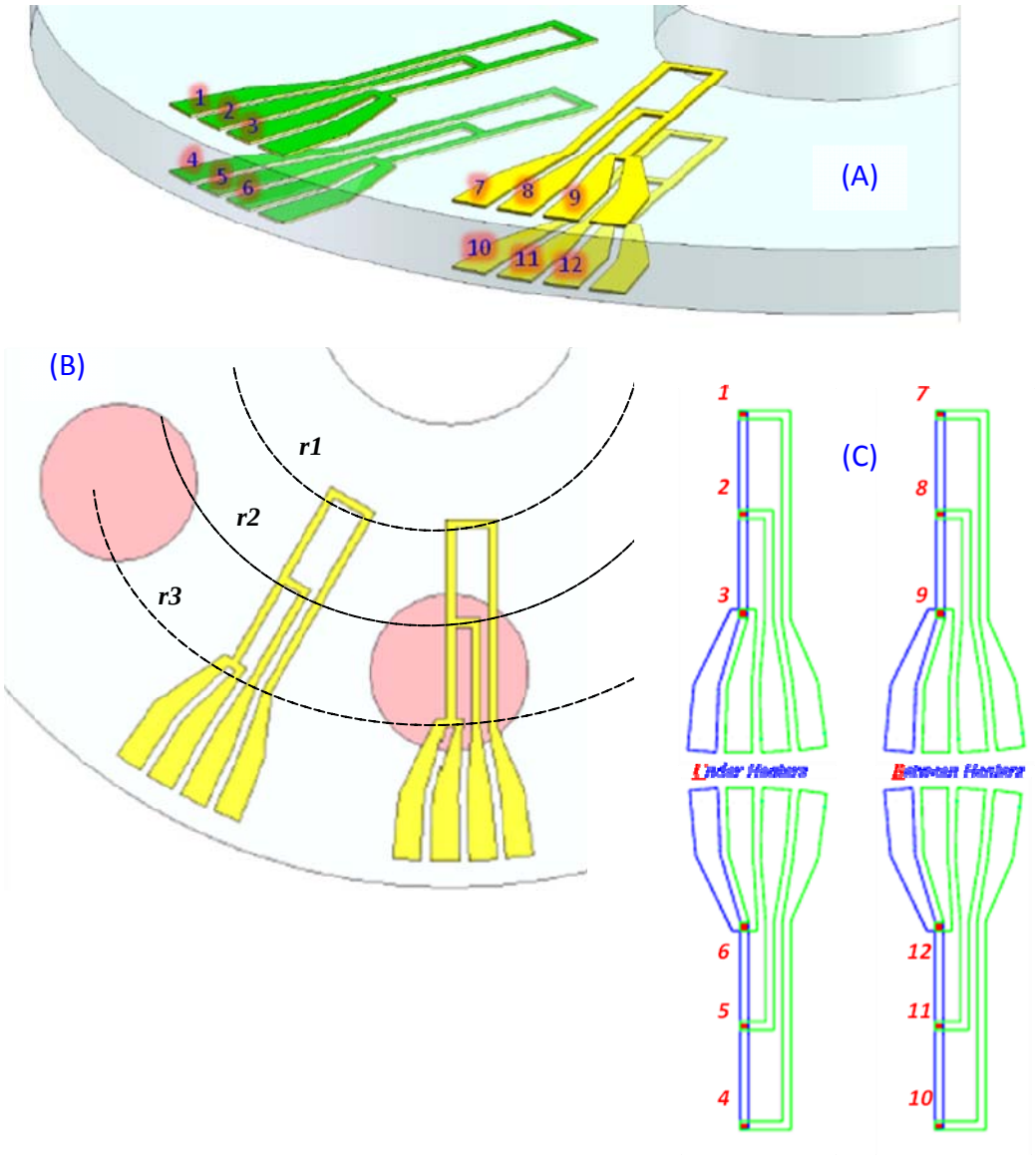

Figure 48. Thermocouple Junction Numbering Scheme.

Because the location under a cartridge heater would likely have a greater heat flux compared to the location between heaters, the circumferential locations were designed to quantify the temperature difference from under and between cartridge heaters. Figure 48 (C) shows the junction numbering.

Equation (3) shows the heat flow (W) between Junction 1 and 4, where A (m^2) is heat transfer area, k (W/(m-°C)) is the disk's average thermal conductivity, and Δx (m) is the disk thickness. The subscripts *r1, r2, and r3* seen in Equations (3) through (5) represent each of the three different radial locations shown in Figure 48. The FEA study, presented in Chapter II, resulted in a fairly uniform temperature distribution on the face of the sensor. Based on those results, an effort to determine a scheme to represent an area weighted heat flow was not pursued. In the formulation shown below, heat flow was calculated in two ways. Equations (3) through (5), the representative area for each junction is equal, so the calculation of heat flow at each junction assumes the entire disk face is at that temperature. Junctions 1 through 6 are located between heaters. Equations (3) through (5) can be averaged, as shown in Eq. (6).

$$Q_{r1} = \frac{kA}{\Delta x}(T_1 - T_4) \qquad \text{Eq. (3)}$$

$$Q_{r2} = \frac{kA}{\Delta x}(T_2 - T_5) \qquad \text{Eq. (4)}$$

$$Q_{r3} = \frac{kA}{\Delta x}(T_3 - T_6) \qquad \text{Eq. (5)}$$

Equation (6) shows the average heat flow for the pattern located between cartridge heaters. Similarly, Eq. (7) shows the average heat flow for the pattern located under a cartridge heater.

$$Q_{Bavg} = \frac{kA}{\Delta x}\left(\frac{(T_1 - T_4)+(T_2 - T_5)+(T_3 - T_6)}{3}\right) \quad \text{Eq. (6)}$$

$$Q_{Uavg} = \frac{kA}{\Delta x}\left(\frac{(T_7 - T_{10})+(T_8 - T_{11})+(T_9 - T_{12})}{3}\right) \quad \text{Eq. (7)}$$

The above values for heat flow were compared to an average value of heat flow, shown in Eq. (8). The average heat flow is calculated based on an average surface temperature for each side of the disk. All of the face temperatures are averaged and used to calculate the temperature difference through the disk.

$$Q_{avg} = \frac{kA}{\Delta x}\left(Avg(T_1, T_2, T_3, T_7, T_8, T_9) - Avg(T_4, T_5, T_6, T_{10}, T_{11}, T_{12})\right) \quad \text{Eq. (8)}$$

Using an average heat flow was believed to be a reasonable approach based on the assumption that there would be a relatively small temperature gradient across the face of the sensor. This formulation also assumes adiabatic conditions at the surface of the ceramic disk. Some fraction of the total heat transfer is lost to the surrounding blanket insulation. However, the amount should be relatively small because the thermal conductivity ratio of nickel parts to the ceramic is 10:1 and of the ceramic to blanket insulation surrounding that area is 30:1. One dimensional heat transfer through a finite volume was calculated to estimate a worst case heat loss from the edges of the heat flux

sensor assembly. Figure A-3, shown in the Appendix, shows (a) the heat flux sensor geometry and heat flow paths, (b) a representative volume of the microporous insulation surrounding the heat flux sensor assembly, and (c) the representative area where heat is lost through the surface of the insulation. For an assembly surface temperature of 700 °C, the insulation loss is 420 W/m^2. Approximating the exterior surface of the insulation with a thin revolved surface results in a heat loss of 2.3 W.

5.2 ASC-E #1's Heat Flux Sensor

Inspection of the heat flux sensor data revealed that many of the thermocouple junctions had failed during the test. An interesting phenomenon observed about the thermocouple performance was that the junction output could fail, usually resulting in a zero value, and then later recover to a logical value (nearly picking up where it left off before failure). Figure 49 shows the junction output voltages for the sensor present on ACS-E #1 from 0 to 10,000 hr. Figure 50 shows the corresponding temperatures. Additional plots of the sensor's emf voltage output are shown in Appendix Figures A-4 and A-5.

Some junctions had intermittently failed during the test. One would expect that the films which experienced physical damage would remain failed throughout the test. Furthermore, a change in chemistry due to diffusion of interfacing metallics should result in a constant bias. One possible explanation for the temporary nature of the output failure is that some portion of a film had adhered to the interfacing disk, despite is Alumina coating. At that point, the electrical circuit would be partially present on the sensor and partially present on the interfacing disk. Those parts of the circuit could become

disjointed during thermal transients, caused by shutdown and startup. This could explain the intermittent signal output during startup and shutdown.

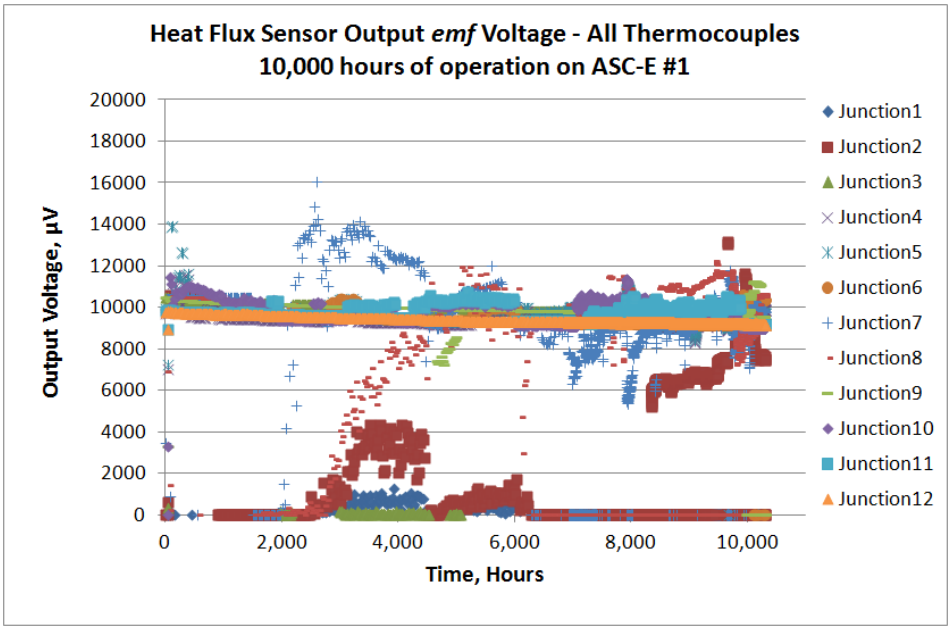

Figure 49. ASC-E #1's Sensor Output Voltage, All Junctions, 0-10,000 hr.

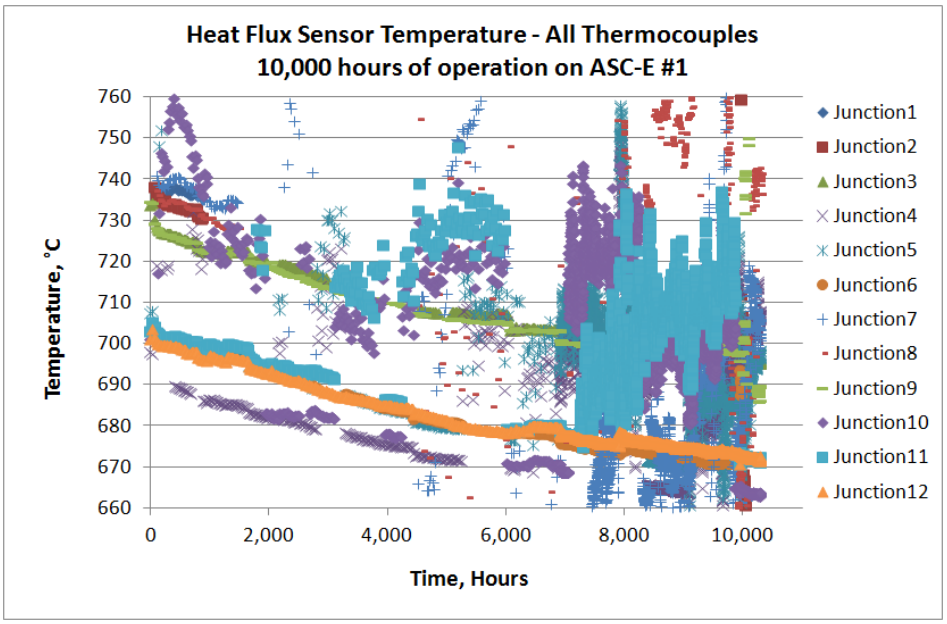

Figure 50. ASC-E #1's Sensor Temperatures, all junctions, 0-10,000 hr.

Figure 51 shows junction temperatures from 2,250 to 2,500 hr. Only four of those were operational past 7,000 hr. The temperatures shown in the figure were used to quantify axial and radial temperature differences of the sensor located on ASC-E #1.

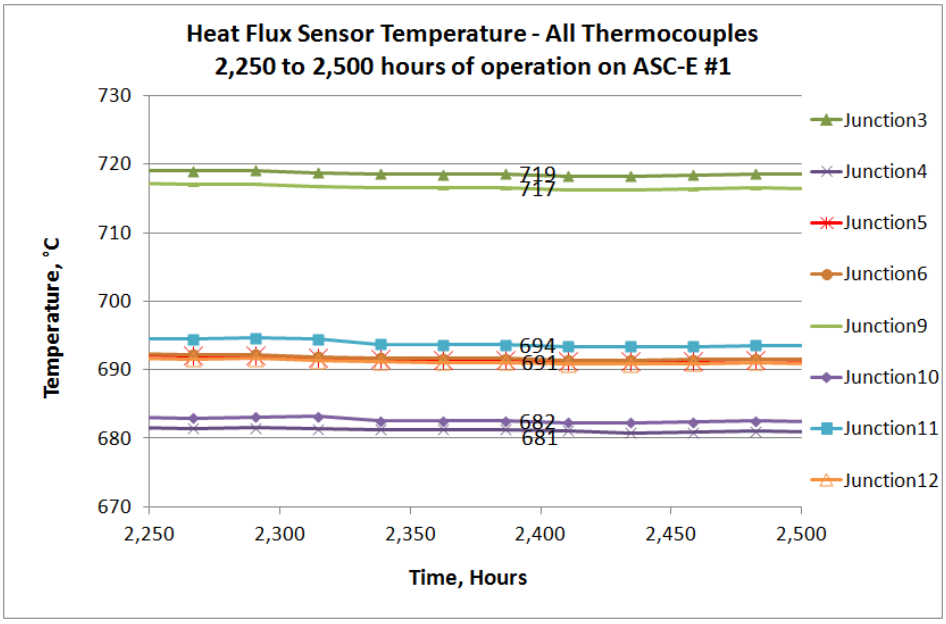

Figure 51. ASC-E #1's Sensor Temperatures, (8x) Junctions, 2,250 to 2,500 hr.

Figure 52 shows axial and radial temperature differences recorded from 2,250 to 2,500 hrs. Table VI contains a summary of the temperature differences shown in the figure. The maximum radial temperature variation observed was 11 °C while the maximum circumferential temperature variation was 3 °C. The radial temperature variation exceeded the FEA predictions by 2x while the circumferential temperature variation was lower than anticipated.

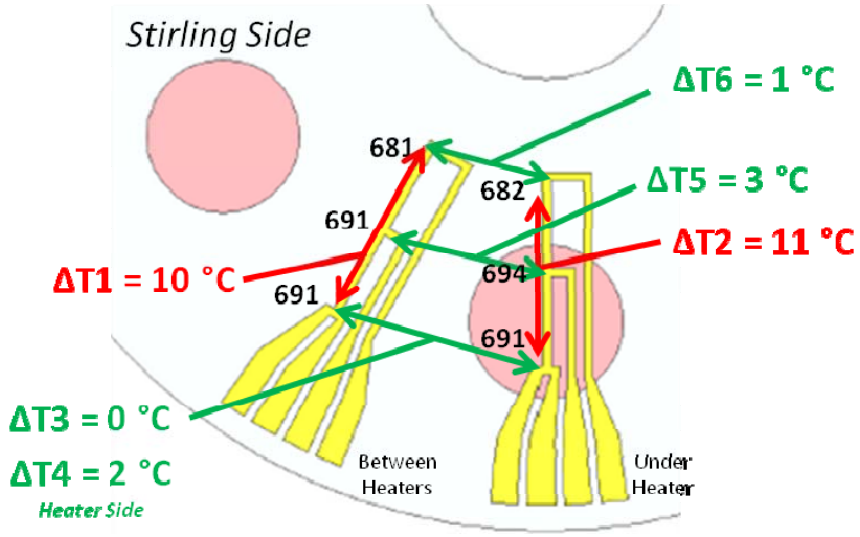

Figure 52. ASC-E #1's Sensor Temperature Variation, 2,250 to 2,500 hr.

Table VI. Resulting Temperature Variation on Stirling side of ASC-E #1's Sensor.

ΔT	°C	Gradient Direction
1	10	Radial
2	11	Radial
3	0	Circumference
4	2	Circumference, ***Heater side***
5	3	Circumference
6	1	Circumference

Figure 53 shows the four thermocouples which survived throughout the 10,000 hr test. Junction 9 did actually end up failing later at 10,300 hr. The data presented was limited to 10,000 hr. The surviving temperatures were compared to the spacer temperatures, shown in Figure 54, only to find the thick spacer temperature was about 35 °C higher than the sensor temperature near that spacer. In contrast, the thin spacer temperature was just about the same as the sensor temperature near that spacer. The temperature trends observed might be explained by the steep temperature gradient near

the much hotter heat source and by contact resistance, although the latter does not appear to be prevalent throughout the data for either convertor, and is therefore unlikely.

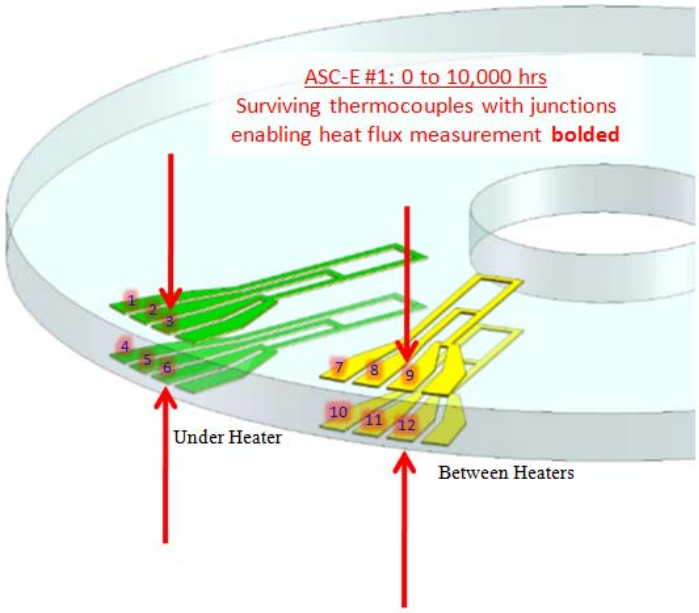

Figure 53. ASC-E #1's Sensor Surviving Junctions at 10,000 hr.

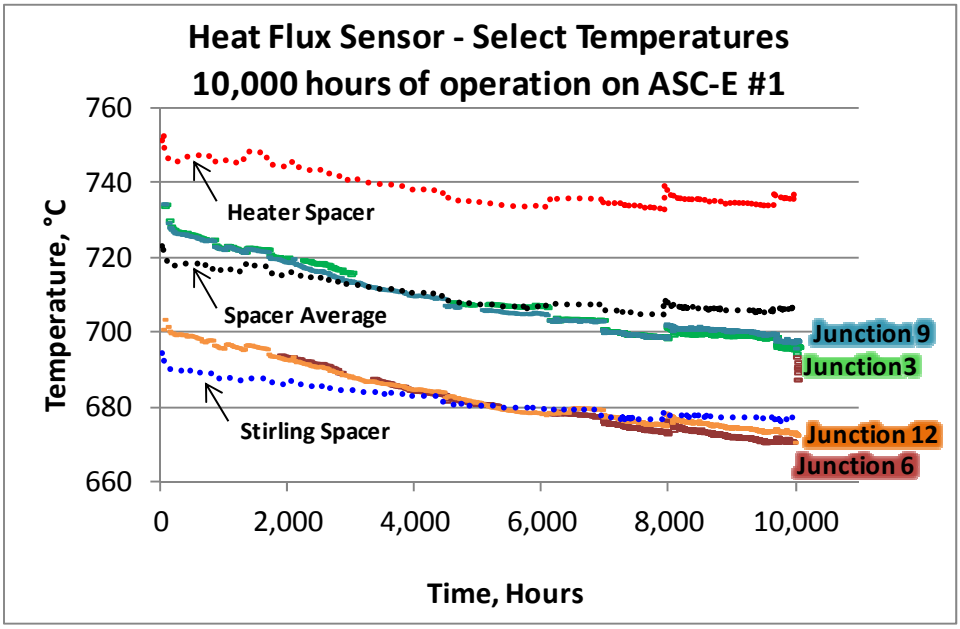

Figure 54. ASC-E #1's Sensor Temperature, 4x Junctions & Spacers, 10,000 hr.

Based on the four surviving thermocouples, heat flow values were calculated for locations under and between the cartridge heaters, shown in Eq. (9) and (10). For comparison, the average heat flow was calculated using a temperature difference based on an average face temperature, using the surviving junction's temperatures, shown in Eq. (11).

$$Q_{Bavg} = \frac{kA}{\Delta x}(T_3 - T_6) \quad \text{Eq. (9)}$$

$$Q_{Uavg} = \frac{kA}{\Delta x}(T_9 - T_{12}) \quad \text{Eq. (10)}$$

$$Q_{avg} = \frac{kA}{\Delta x}\big(Avg(T_3, T_9) - Avg(T_6, T_{12})\big) \quad \text{Eq. (11)}$$

The corresponding heat flow values based on the available temperature measurements is shown Figure 55. Table VII describes the events labeled 1 through 12. Figure 55 only highlights some of the events while others are shown for the same data collected on ASC-E #4. Event 2, shown in Figure 55, shows an increase in heat flow but does not correspond to a recorded event in the test history. Such recorded events could include shutdown for facility maintenance, controlled shutdown due to failed test instrumentation, or a change in the operating point based on the desire to maintain a particular steady state operation. The periods from events 3 to 4 and events 5 to 9 show increasing heat flow for a period of known steady power output. This increase is discussed further in the next chapter.

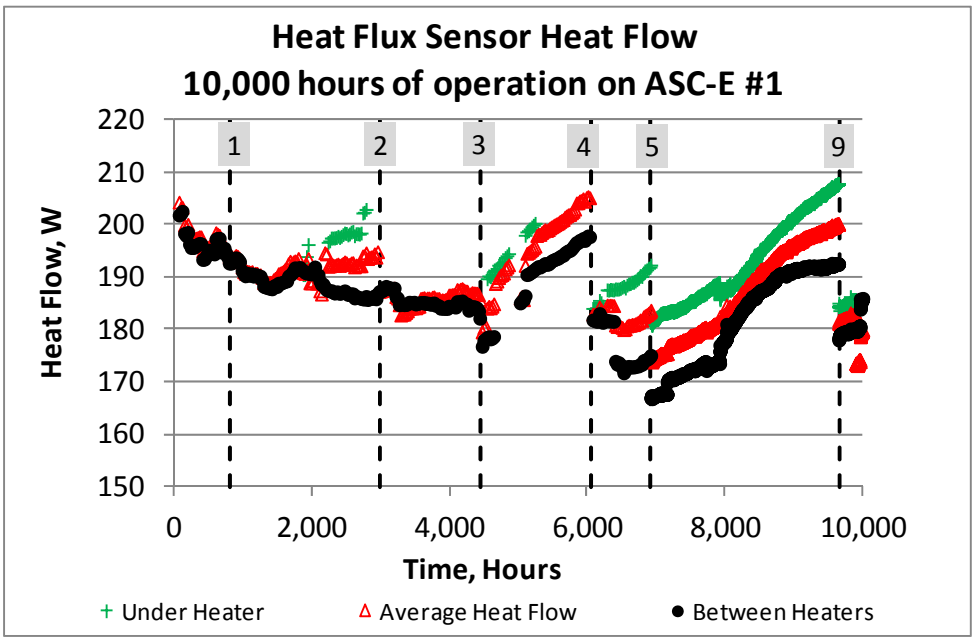

Figure 55. ASC-E #1's Sensor Heat Flow, 10,000 hr.

Table VII. Test Event List

Item	Hrs	Description
1	808	A & B PID adjustment (-1 °C)
2	2986	*no shutdown, unknown event*
3	4444	manual shutdown, known change in performance
4	6049	manual shutdown, rack calibration
5	6926	manual shutdown, power lead swap
6	8024	controlled shutdown, thermocouple failure
7	8999	*no shutdown, unknown event*
8	9273	*no shutdown, unknown event*
9	9667	manual shutdown, facility maintenance
10	9743	*no shutdown, unknown event*
11	9888	*no shutdown, unknown event*
12	9980	manual shutdown, facility maintenance

Figure 56 shows the heat flow from 9,000 to 9,250 hr. The locations under and between cartridge heaters varied around 11 W. The average heat flow, bounded by the heat flow under and between cartridge heaters, was 197 W.

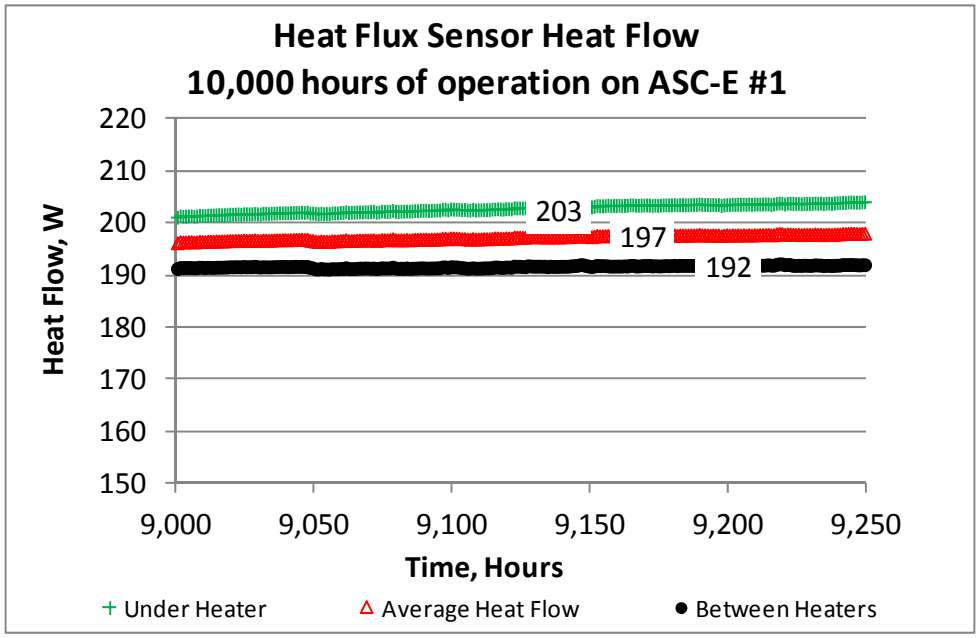

Figure 56. ASC-E #1's Sensor Heat Flow, 9,000-9,250 hr.

Figure 57 shows how the heat flow calculation correlates strongly to the axial temperature difference across the disk. The axial temperature difference ranged from 23 to 28 °C throughout the test. This turned out to be much lower than the expected 40 °C discussed in Chapter II. This can be explained by comparing the constant thermal conductivity used in the design phase to the temperature dependent value observed during testing. When the thermal conductivity was increased from the constant 5.4 W/(m-°C) to the value observed during testing, 7.5 W/(m-°C), the temperature difference decreased from 40 to 29 °C which is in line with the test data.

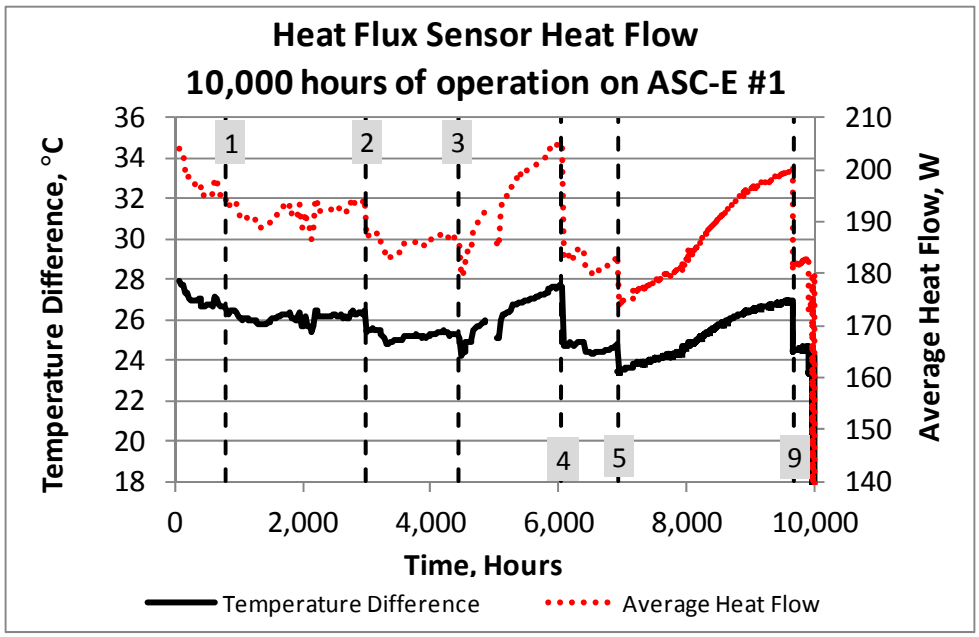

Figure 57. ASC-E #1's Disk Axial Temp. Diff. & Sensor Avg. Heat Flow, 10,000 hr.

Figure 58 shows how the heat flow calculation is weakly correlated to changes in the ceramic thermal conductivity, which ranged from 7.4 to 7. 5 W/(m-°C) throughout the test. Figure 59 shows the Hot-End Temperature changing with the Heat Flow at events 1, 3, and 4. Event 1 represents a PID adjustment and events 3 and 4 represent thermal cycles experienced during shutdown and startup. The only trend in Heat Flow that corresponds to Heater Temperature, shown in Figure 60, is the slow decreasing trend occurring from event 1 to 3. This trend is expected in tests which contain a heat source that is mechanically loaded against the convertor. The test is controlled off of the Hot-End Temperature so as the contact resistance decreases due to oxidation of the mating components, the amount of heat required to maintain that Hot-End Temperature decreases and so does the Heater Temperature.

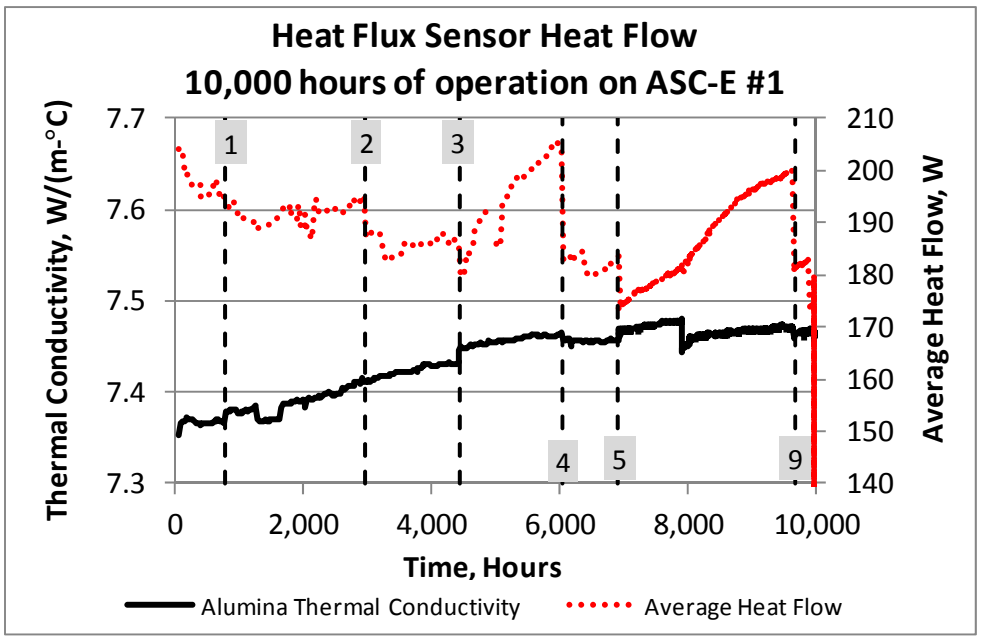

Figure 58. ASC-E #1's Sensor Alumina Thermal Cond. & Avg. Heat Flow, 10,000 hr.

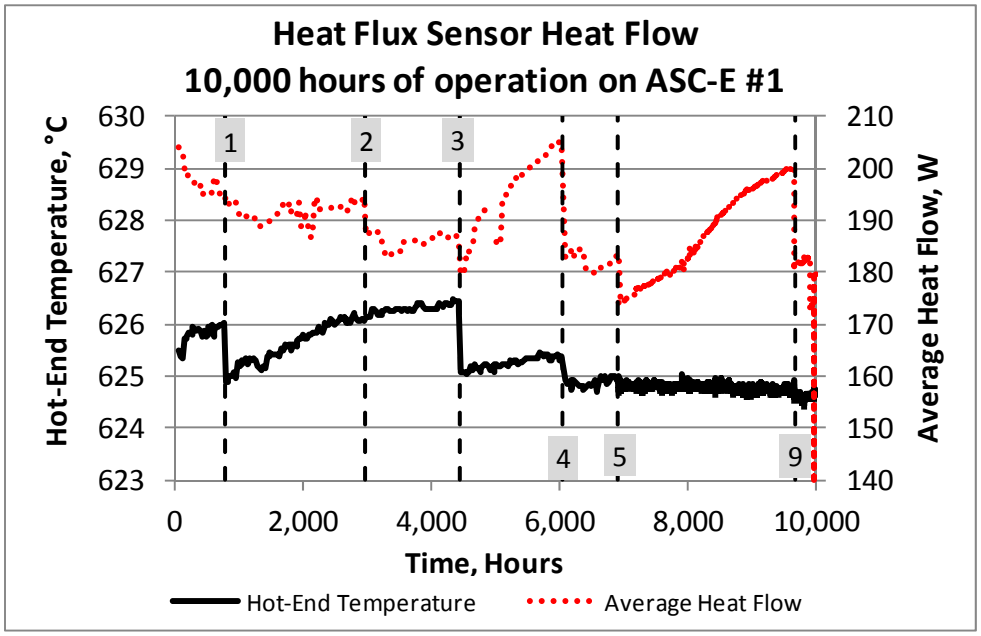

Figure 59. ASC-E #1's Hot-End Temperature & Sensor Avg. Heat Flow, 10,000 hr.

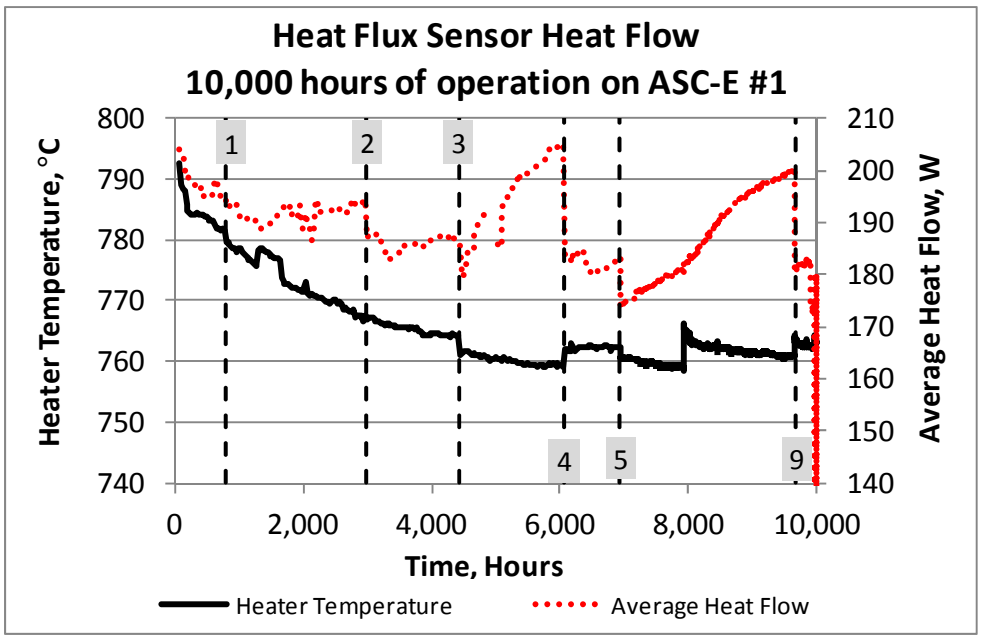

Figure 60. ASC-E #1's Heater Temperature & Sensor Avg. Heat Flow, 10,000 hr.

The piston amplitude and average heat flow are shown in Figure 61.

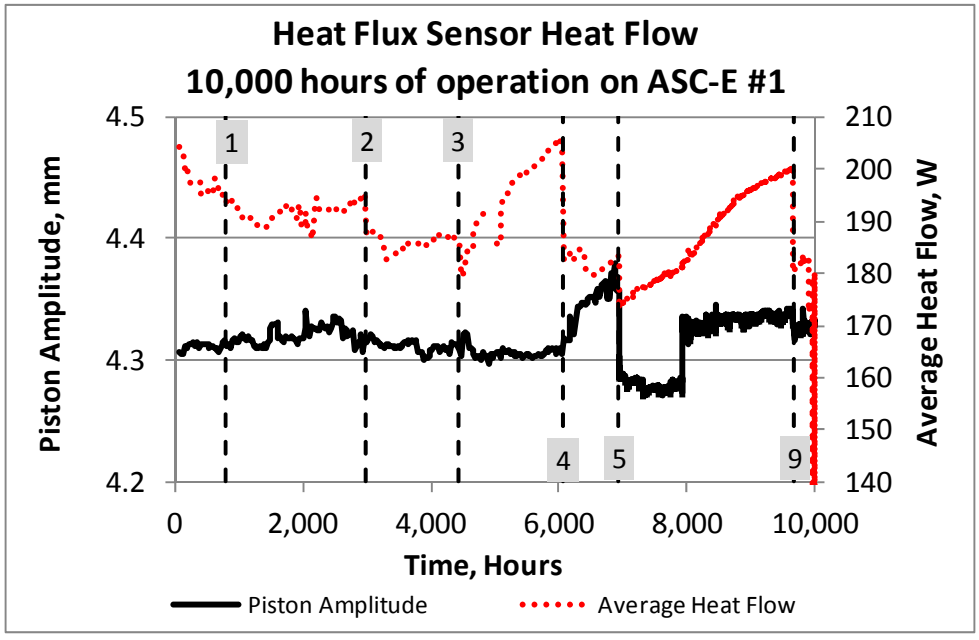

Figure 61. ASC-E #1's Piston Amplitude & Sensor Avg. Heat Flow, 10,000 hr.

Periods from events 3 to 4 and from events 5 to 6 represent periods when the Piston Amplitude remained relatively flat and the Heat Flow continued to increase. Also, events 4 to 5 represent a period when the Piston Amplitude increased and the Heat Flow was flat. These data suggest the convertor's performance was changing: for a constant operating frequency and hot-end temperature control, the heat input should increase when the piston amplitude is increased. The convertor thermal efficiency, calculated using Equation (12), ranged from 35 to 39 % until event 3. The efficiency then ranged from 31 to 36 %, usually starting out high and decreasing until the next shutdown event.

$$\eta = \frac{electric\ power\ output}{Sensor\ Average\ Heat\ Flow} \qquad \text{Eq. (12)}$$

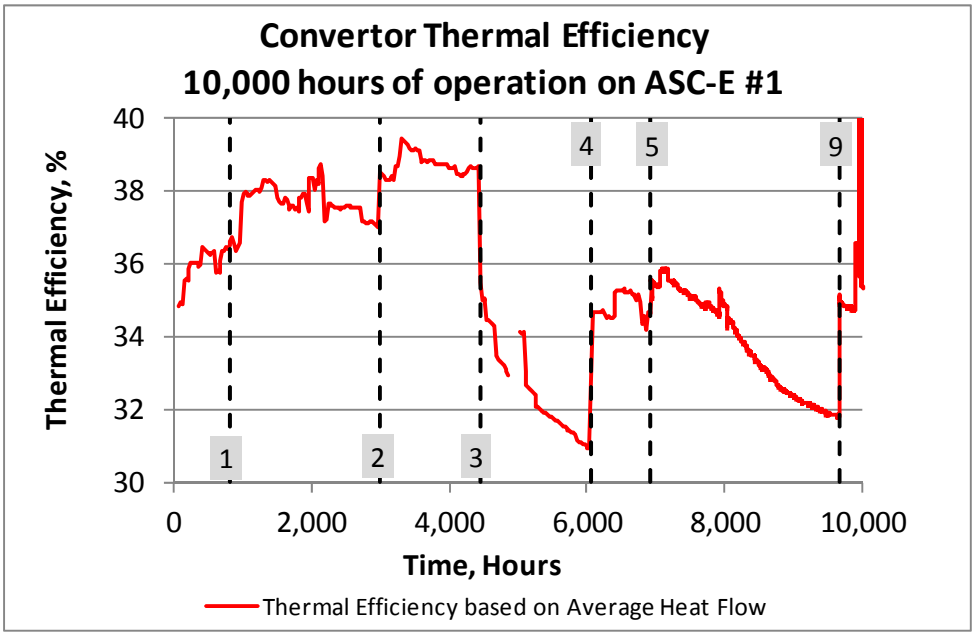

Figure 62. ASC-E #1's Thermal Efficiency, 10,000 hr.

5.3 ASC-E #4's Heat Flux Sensor

Figure 63 shows the junction temperatures for the sensor present on ACS-E #4's through 10,000 hr. The corresponding sensor emf voltage output is shown in Appendix Figure A-10. Different than that observed on ASC-E #1's sensor, all of one side was not operational until 6,000 hr. Additionally, some junctions had intermittently failed during the test, as observed on ASC-E #1. The four opposed junctions that were operational from 8,000 to 10,000 hr enabled the calculation of heat flow under and between cartridge heaters.

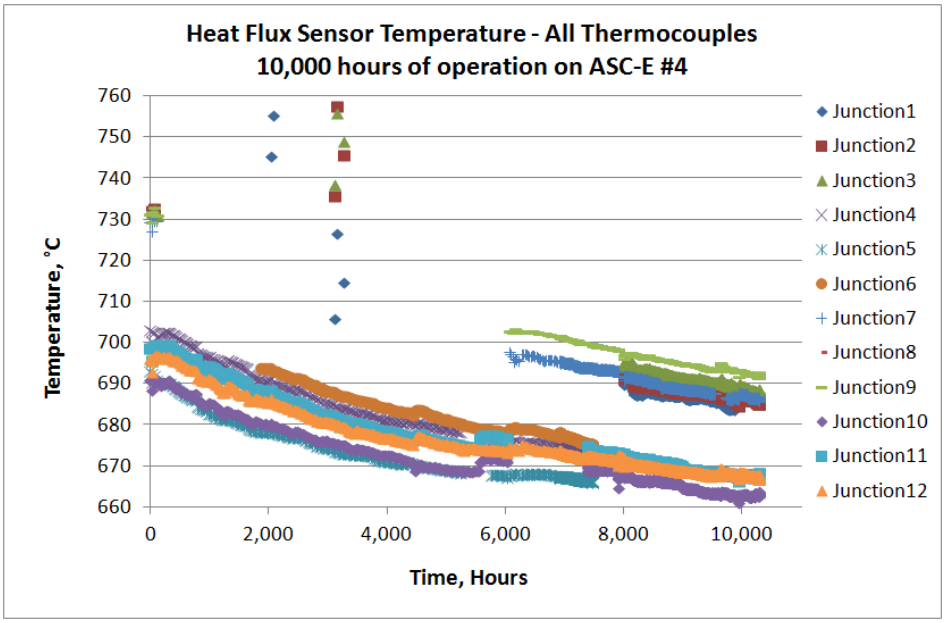

Figure 63. ASC-E #4's Sensor Temperatures, All Junctions, 0-10,000 hr.

Figure 64 shows junction temperatures from 9,000 to 9,250 hr. The temperatures shown in the figure were used to quantify axial and radial temperature difference of the sensor located on ASC-E #4. Figure 65 shows graphically what is summarized in Table VIII. The maximum radial temperature variation observed was 6 °C while the maximum

circumferential temperature variation was 3 °C. The radial temperature variation was 5 °C less than that observed on ASC-E #1 while the circumferential temperature variation was the same at 3 °C.

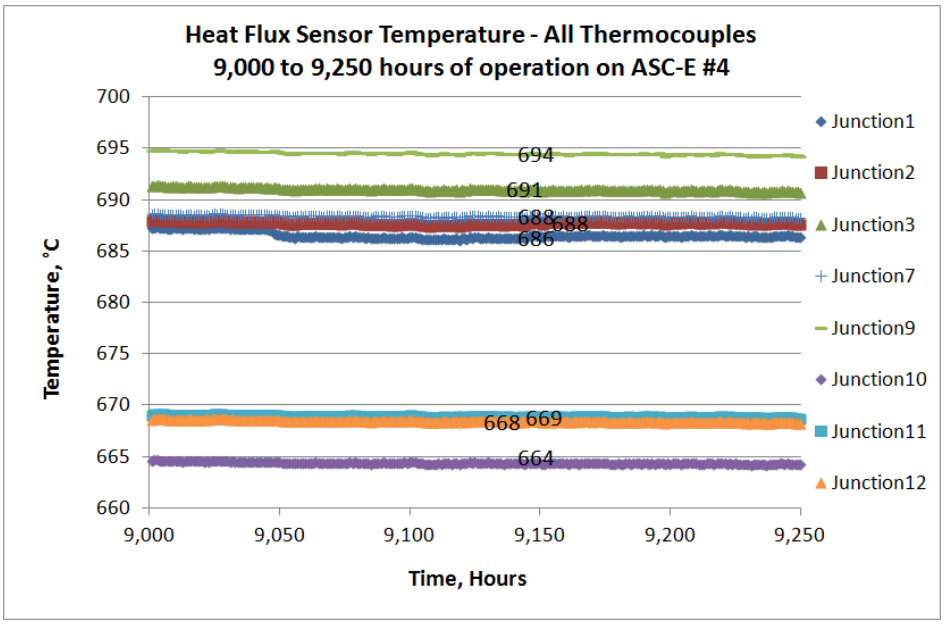

Figure 64. ASC-E #4's Sensor Temperatures, (8x) Junctions, 9,000-9,250 hr.

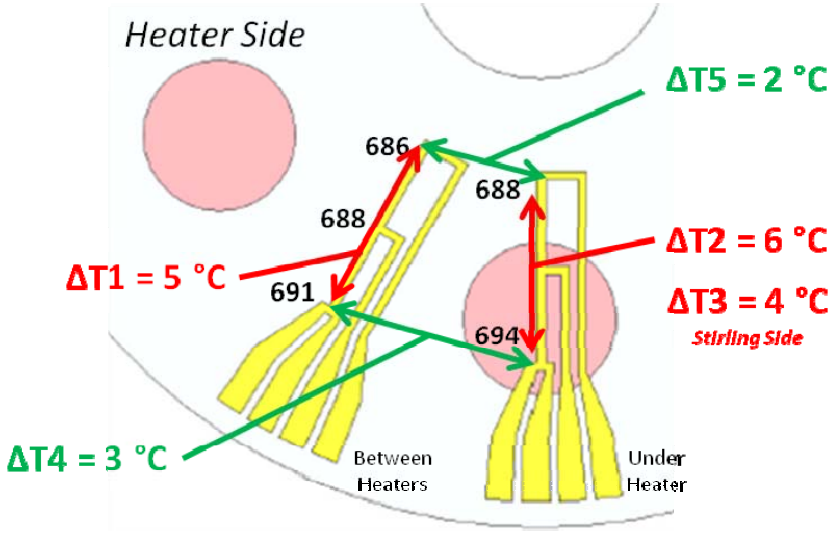

Figure 65. ASC-E #4's Sensor Temperature Variation, 9,000-9,250 hr.

Table VIII. Resulting Temperature Variation on Heater side of ASC-E #4's Sensor.

ΔT	°C	Gradient Direction
1	5	Radial
2	6	Radial
3	4	Radial, **Stirling side**
4	3	Circumference
5	2	Circumference

Figure 66 shows thermocouples junctions which survived past from 8,000 to 10,000 hr.

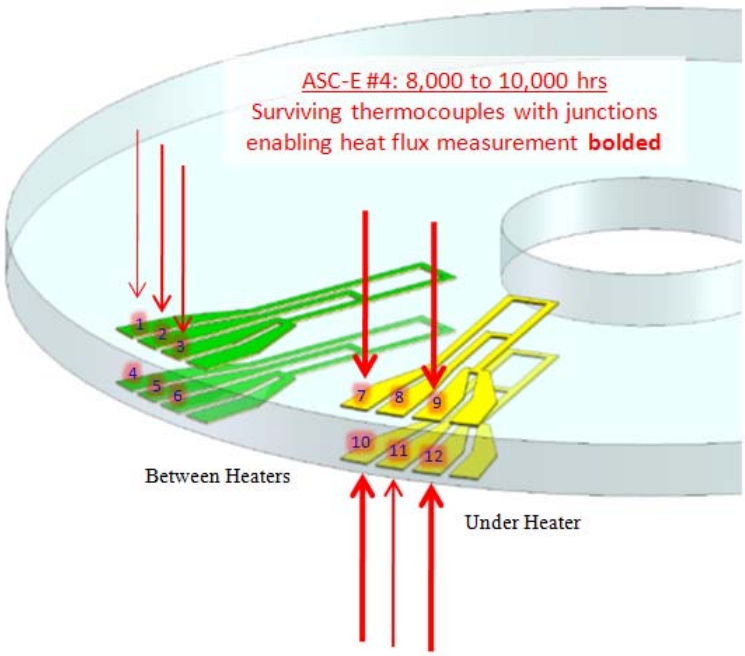

Figure 66. ASC-E #4's Sensor Surviving Junctions from 8,000-10,000 hr.

The surviving junction temperatures were compared to the spacer temperatures, shown in Figure 67. The same observation made in ASC-E #1's data was also observed

here. The thick spacer temperature was about 35 °C higher than the sensor temperature near that spacer. Similar observations were made with the thin spacer as well. The temperature trends observed are likely explained by the steep temperature gradient near the much hotter heat source. Contact resistance is much less likely, considering the same result on both convertors.

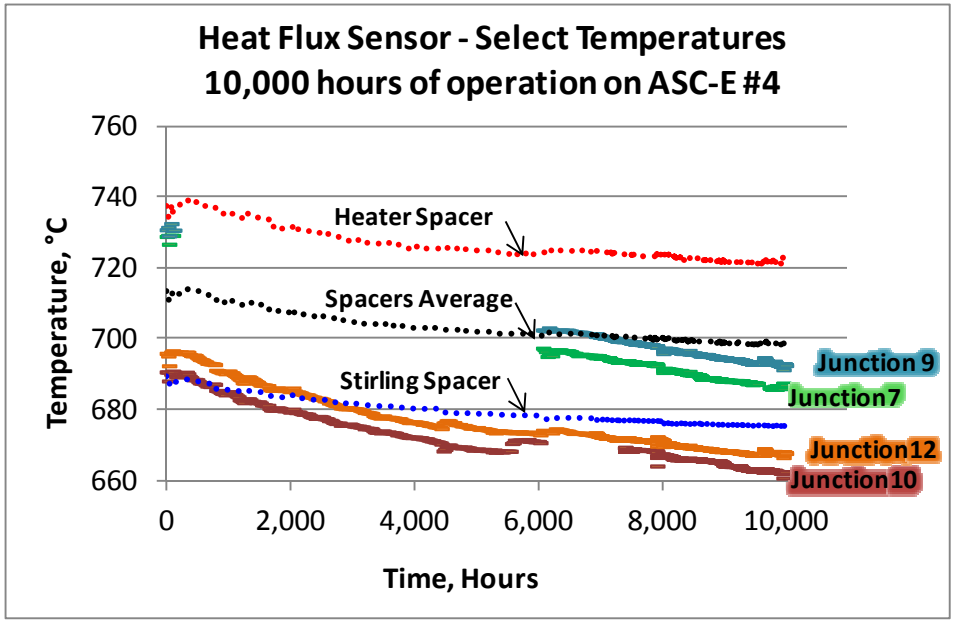

Figure 67. ASC-E #4's Sensor Temp., 4x Junctions & Spacers, 10,000 hr.

Based on the four surviving thermocouples, heat flow values were calculated for two locations under a cartridge heater, as shown in Eq. (13) and (14). For comparison, the average heat flow was again calculated using a temperature difference based on an average face temperature, using the same junction temperatures, shown in Eq. (15).

$$Q_{Uavg}^{r1} = \frac{kA}{\Delta x}(T_7 - T_{10}) \qquad \text{Eq. (13)}$$

$$Q_{Uavg}^{r3} = \frac{kA}{\Delta x}(T_9 - T_{12}) \qquad \text{Eq. (14)}$$

$$Q_{avg} = \frac{kA}{\Delta x}\left(Avg(T_7, T_9) - Avg(T_{10}, T_{12})\right) \qquad \text{Eq. (15)}$$

The corresponding local heat flow values based on the available temperature measurements are shown Figure 68. Events 7, 8, 10, and 11 represent unknown causes for the change observed in Heat Flow. Other events represent shutdown/startup thermal transients.

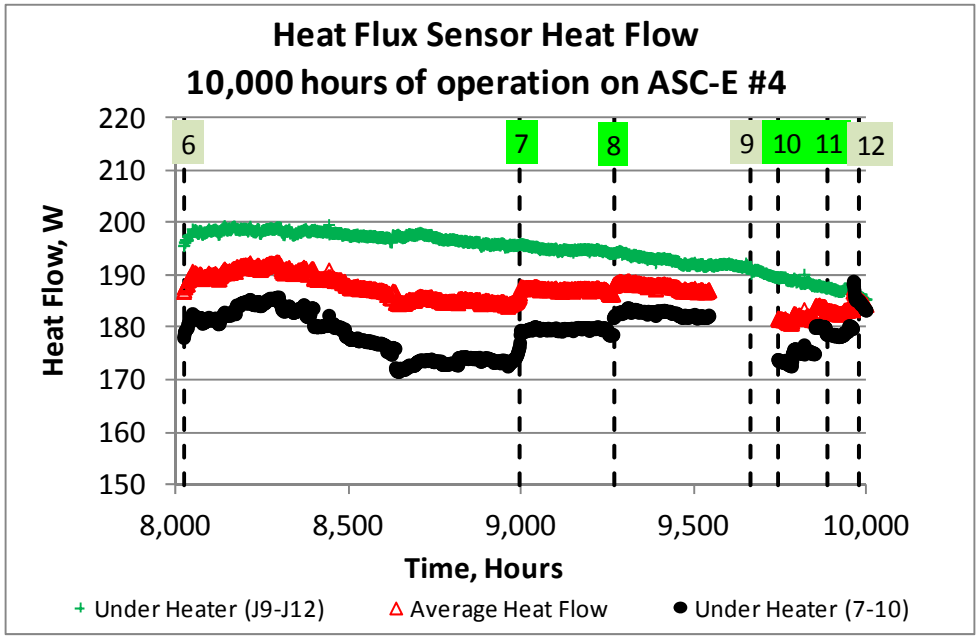

Figure 68. ASC-E #4's Sensor Heat Flow, 8,000-10,000 hr.

Figure 69 shows the heat flow from 9,000 to 9,250 hr. There was a much larger difference between the highest heat flow (195 W) and the average heat flow (164 W). The surface temperatures were suspected of being erroneous but checked out during

inspection. The locations two locations under a cartridge heaters varied a surprising 15 W. The average heat flow turned out to be 10 W lower than that observed on ASC-E #1.

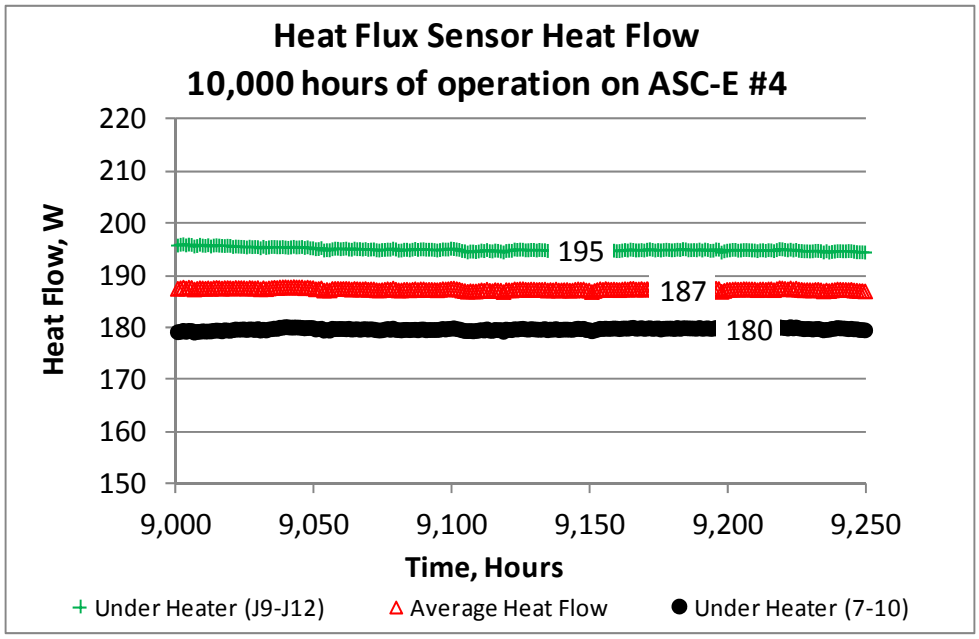

Figure 69. ASC-E #4's Sensor Heat Flow, 9,000-9,250 hr.

Figure 70 shows that the heat flow correlates strongly to the axial temperature difference across the disk. The axial temperature difference ranged from 21 to 24 °C throughout the test. Figure 71 shows how the heat flow calculation is weakly correlated to changes in the ceramic thermal conductivity, which was around 7.5 W/(m-°C) throughout the test.

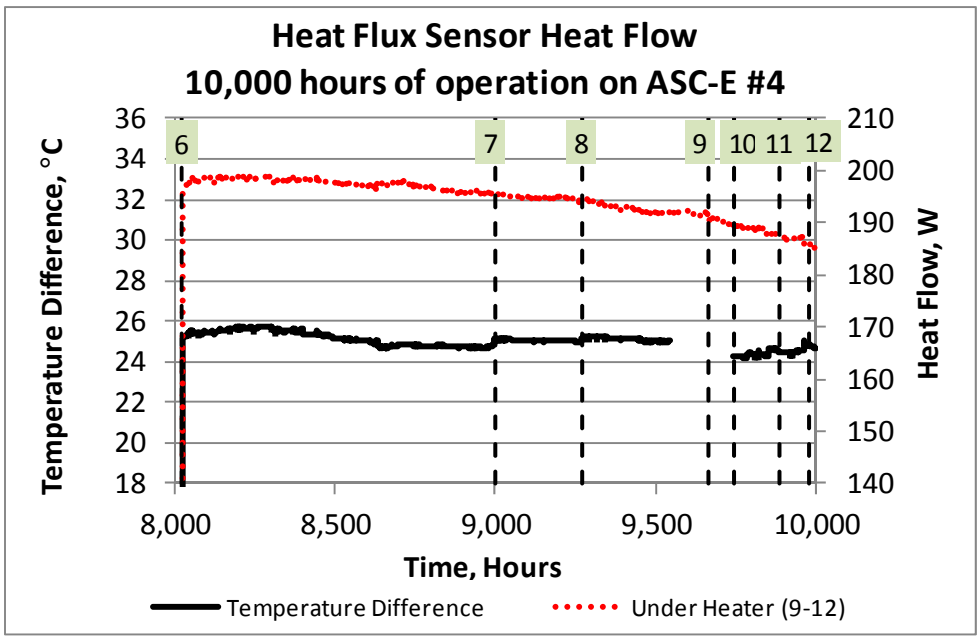

Figure 70. ASC-E #4's Disk Temp. Diff. & Sensor Local Heat Flow, 8,000-10,000 hr.

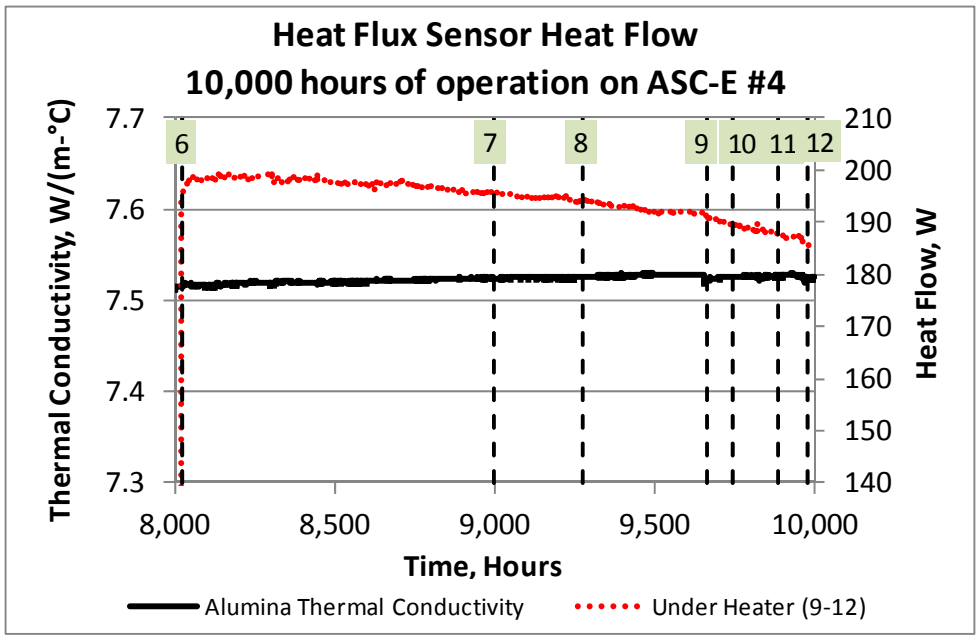

Figure 71. ASC-E #4's Disk Cond. & Sensor Avg. Heat Flow, 8,000-10,000 hr.

Figures 72 and 73 show that the Heat Flow had a stronger correlation to the Heater Temperature, compared to the Hot-End Temperature. The overall decreasing trend

of Heat Flow follows the same trend observed on the Heater. Also, event 9 represents a manual shutdown, which explains the jump in Heater Temperature upon resuming the test. Figure 74 shows that the Heat Flow did not have a strong correlation to the Piston Amplitude. ASC-E #4's Thermal Efficiency, shown in Figure 75, was calculated using Eq. (16).

$$\eta = \frac{electric\ power\ output}{Sensor\ Heat\ Flow{:}\ Under\ Heater(9-12)} \qquad \text{Eq. (16)}$$

ASC-E #4's Thermal Efficiency trended upward for the data collection period achieved, ranging from 32 to 35 %.

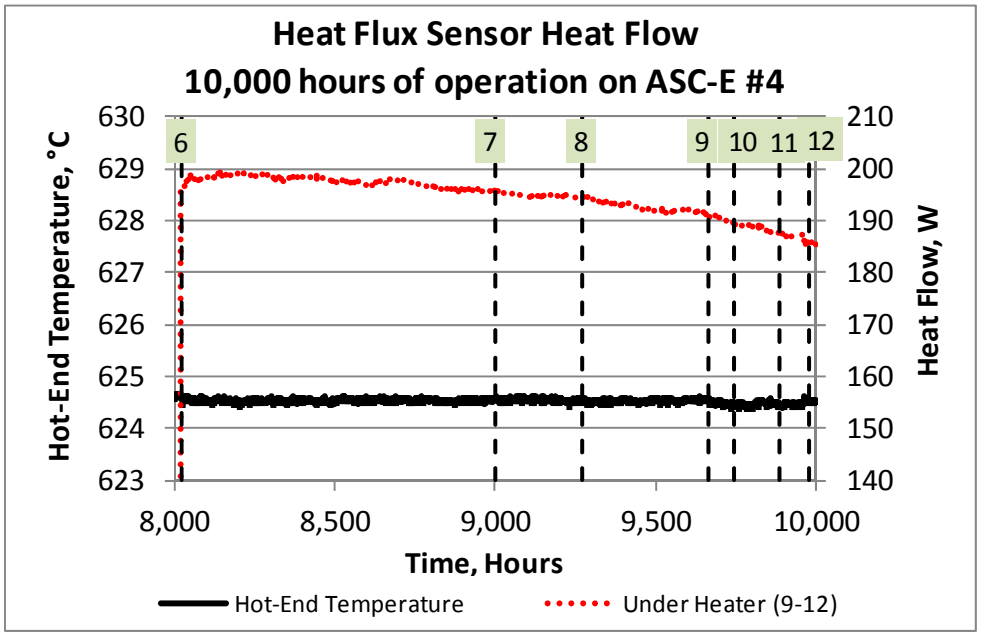

Figure 72. ASC-E #4's Hot-End Temp. & Sensor Local Heat Flow, 8,000-10,000 hr.

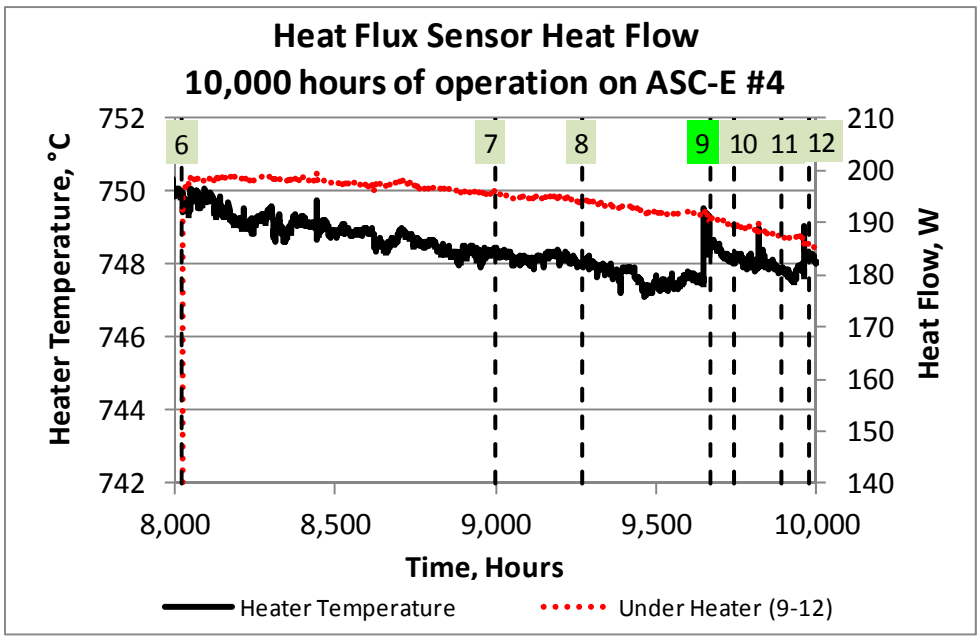

Figure 73. ASC-E #4's Heater Temp. & Sensor Local Heat Flow, 10,000 hr.

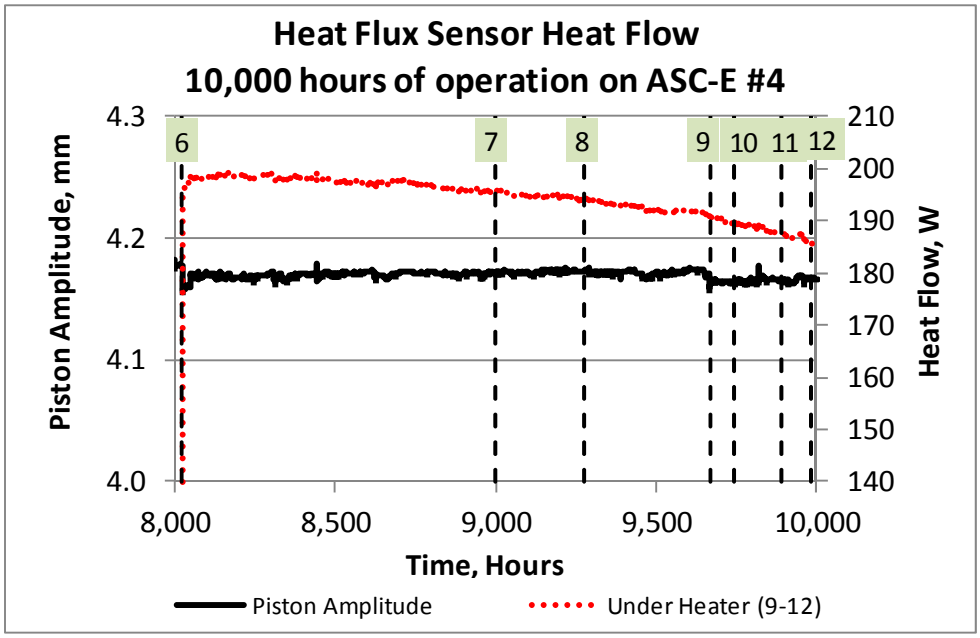

Figure 74. ASC-E #4's Piston Amplitude & Sensor Local Heat Flow, 8,000-10,000 hr.

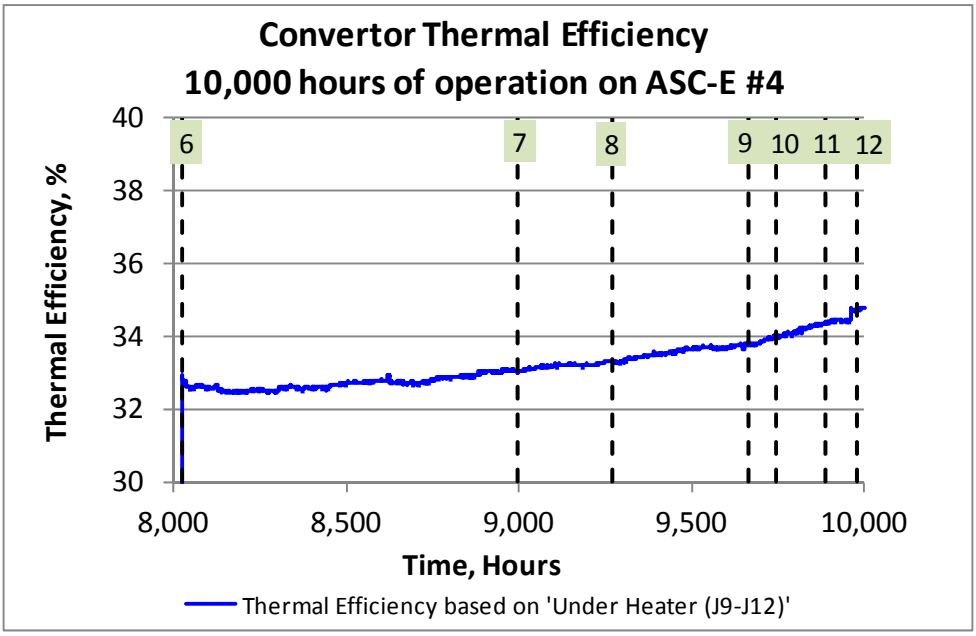

Figure 75. ASC-E #4's Thermal Efficiency, 8,000-10,000 hr.

5.4 Disassembly and Inspection

The ASC-E #1 and #4 test setup was disassembled in the summer of 2011. The insulation was removed and the sensors were removed from the test setup and installed into the protective box designed to hold the custom-made feed through and maintain the same wire orientation used in application. The condition of the sensors after 10,000 hours of testing was much better than expected. Figures 76 through 79 show the condition of the sensors and nickel spacers upon removal of the microporous insulation for both convertors. The sensors were not discolored in any way but did show signs of film diffusion near the outer diameter. Figure 76 shows ASC-E #1's setup where a film pattern found in six distinct diffusion sites on the mating spacer which suggests that the areas where the films were discovered did not have a sufficient layer of protective Alumina, sputtered onto the face of the sensor and spacers to protect against film

diffusion. Cracks were also observed in the thin protective layer of Alumina coating the spacers. The diffusion sites are also highlighted on the heat source spacer, in Figure 73, with areas of film diffusion on the heat collector spacer. The damage to the thin films could explain the anomalous behavior of the thermocouple output.

Figure 78 shows ASC-E #4's sensor, which appears dirty due to the pieces of fiber insulation that had fallen onto the sensor during insulation removal. Figure 79 shows several diffusion sites were observed on the mating spacers in that setup as well, most notably, the large half of the heat collector spacer which appeared considerably different compared to installation. These degradation modes and mitigation techniques are discussed in the next chapter.

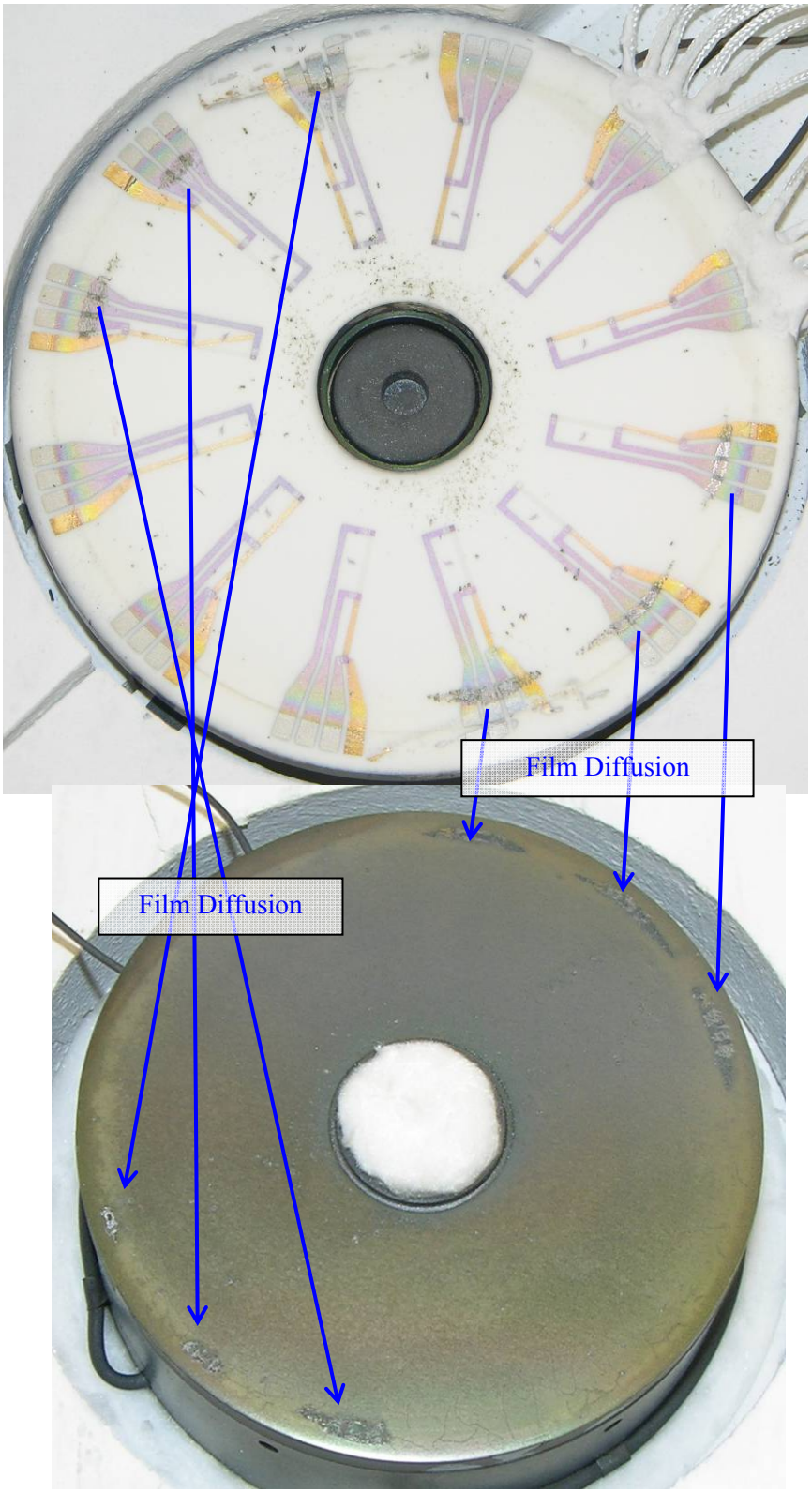

Figure 76. Post Disassembly Condition on ASC-E #1.

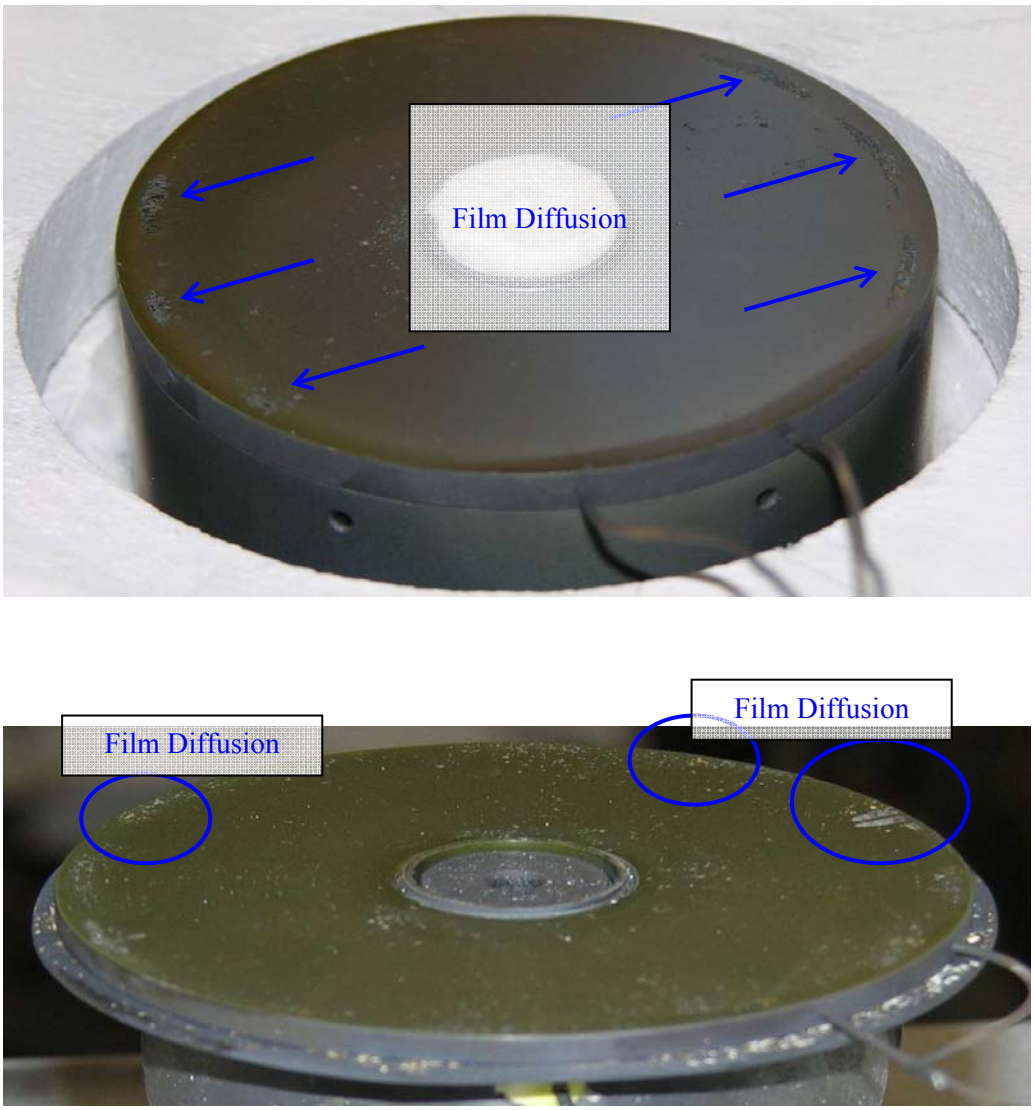

Figure 77. Post Disassembly Condition on ASC-E #1.

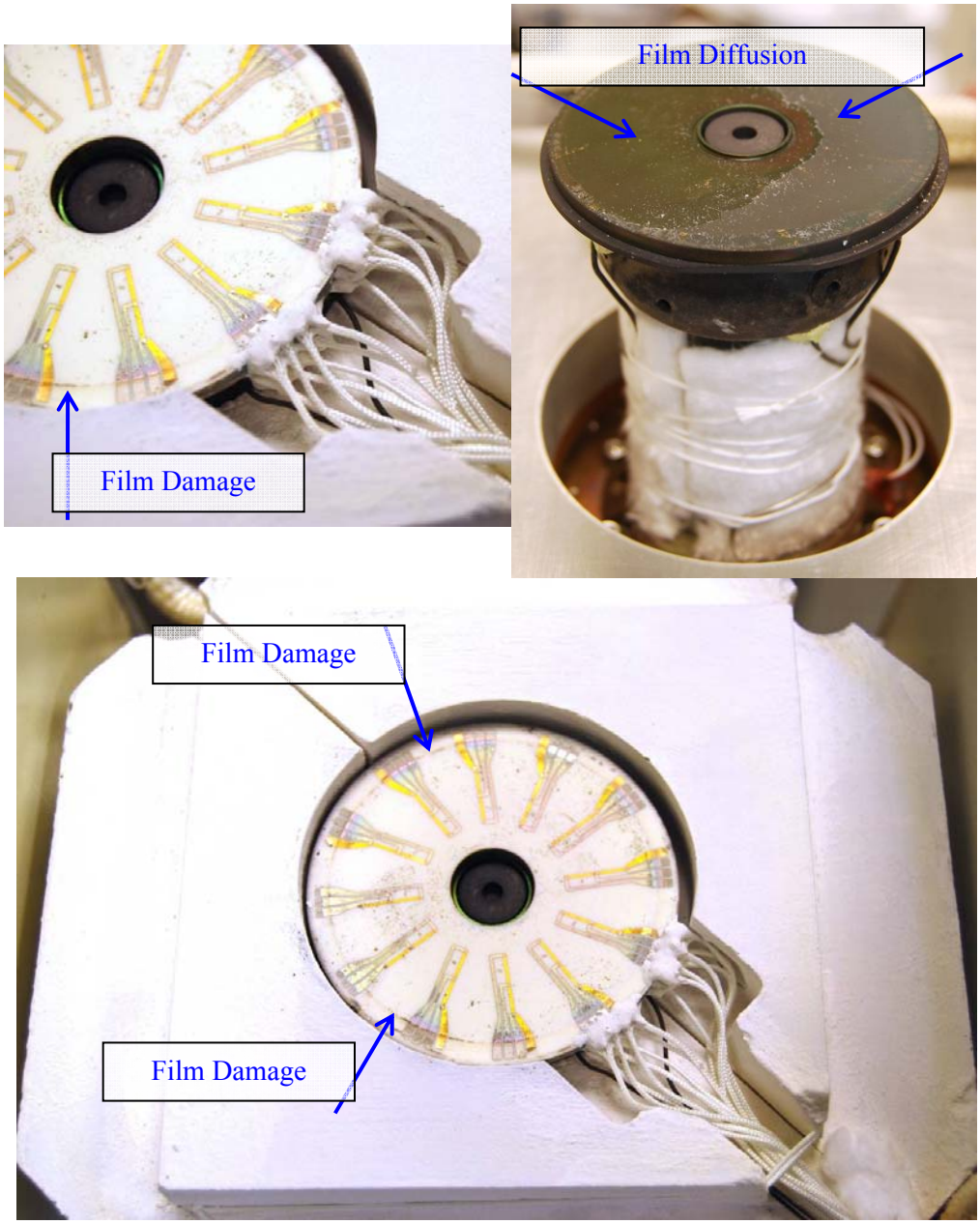

Figure 78. Post Disassembly Condition on ASC-E #4.

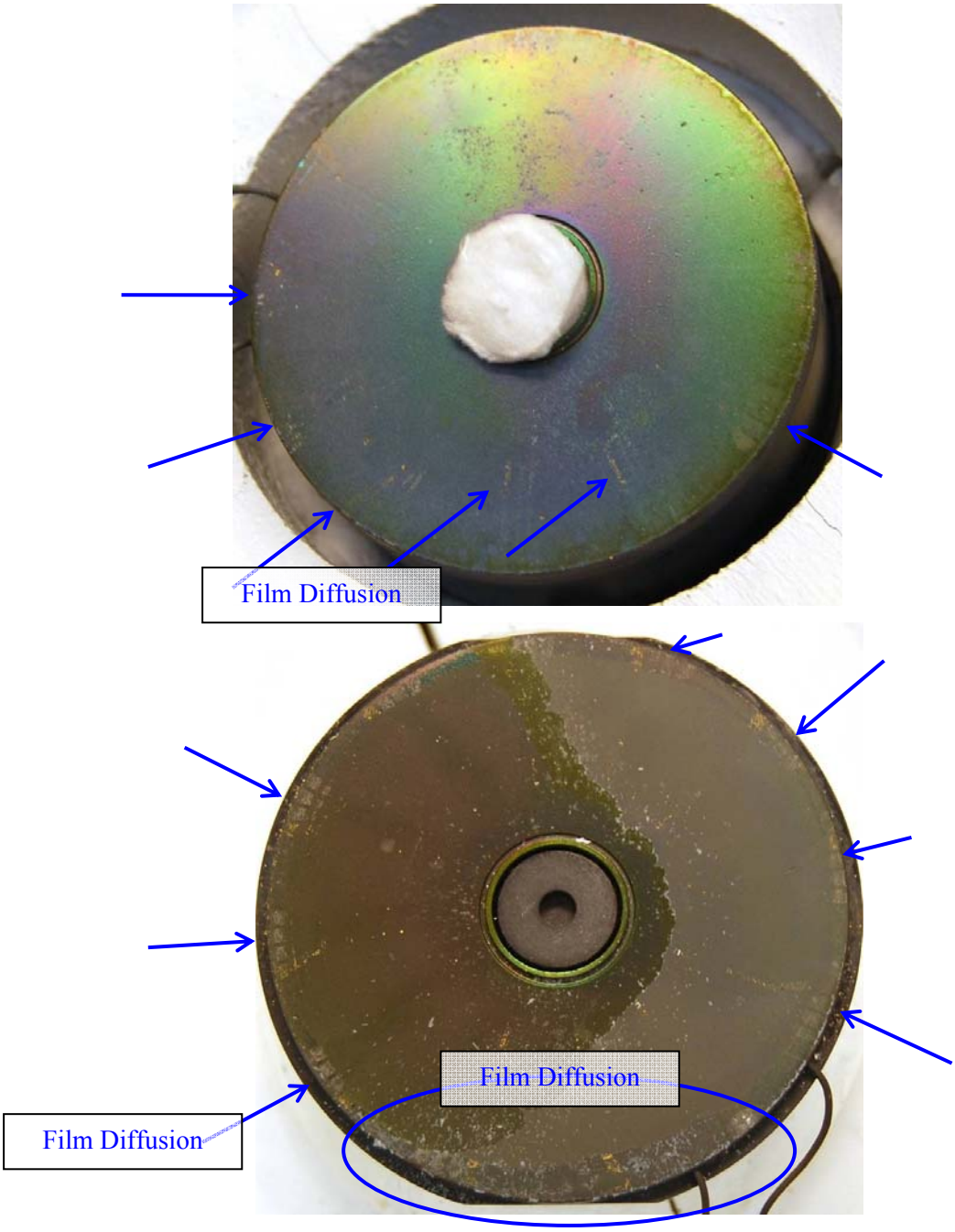

Figure 79. Post Disassembly Condition on ASC-E #4.

CHAPTER VI

CONCLUSIONS

A thin-film heat flux sensor was designed, fabricated, characterized, and tested to directly measure the heat transfer from the heat source to a Stirling convertor while on test at NASA Glenn Research Center. The development effort identified materials, fabrication procedures, and data collection techniques required for measuring heat flux in a Stirling convertor application. The sensors contained gold versus platinum thermocouples deposited on full dense Alumina ceramic substrates. The sensors were tested for 10,000 hours at temperatures exceeding 700 °C in the ASC-E #1 and #4 setup.

The test started in 2009 and was completed in 2011, when the test was shutdown and the sensors removed. Many thermocouple junctions had failed during the test, however, the surviving thermocouple junctions were used to calculate heat flow into the Stirling convertor for over 10,000 hrs on ASC-E #1 and for the last 2,000 hrs of testing

on ASC-E #4. While the effort proved the concept of directly measuring heat flow into an electrically heated Stirling convertor, it also showed that such sensors need to incorporate design improvements to improved reliability for possible future use in power systems.

The resulting heat flow measurements and corresponding thermal efficiency are briefly discussed. Also discussed are several areas of improvement for future designs, including: heat flow formulation, sensor resolution, maximum operating temperature, and sensor robustness. Finally, the status heat addition into Stirling convertors at GRC is summarized.

6.1 Resulting Heat Flow and Thermal Efficiency

The measurements represent heat flow through the ceramic disk located between the heat source and Stirling convertor. Each disk contained six local heat flow measurement sites. In addition, the average heat flow was also calculated based on face temperature. By the end of the test, each disk contained only two local heat flow measurements. The sensors did not perform as desired due to intermittent junction failures which disabled the heat flow measurements. Figure 80 shows the resulting heat flow measurements made during the 10,000 hr test. The heat flow varied most on ASC-E #1, ranging from 175 to 205 W and averaging at about 190 W. The value of heat flow usually changed after a convertor startup, as seen after events 3, 4, and 5. The heat flow only varied from 180 to 195 W on ASC-E #4. The convertor heat flow values are about 10 % lower than the 200 to 210 W expected at those alternator power output levels. That could have elevated the efficiency calculations by about 3 to 4%.

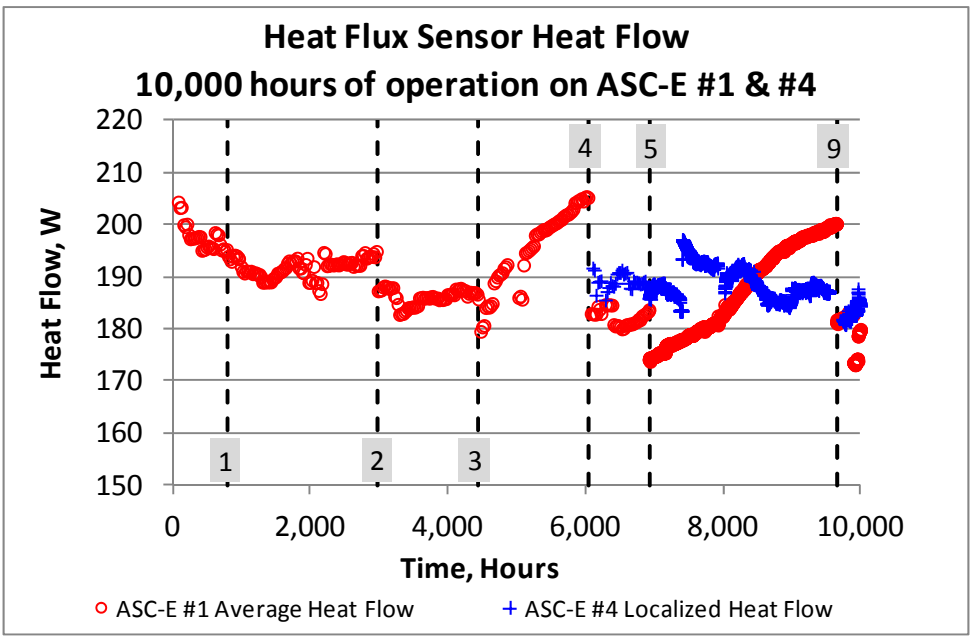

Figure 80. Resulting Heat Flow from ASC-E #1 and #4.

Data between events 3 to 4 and between events 5 to 9 represent periods when power output remained relatively constant while ASC-E #1's heat flow increased significantly. This suggests that ASC-E #1's Stirling cycle was accepting less heat. The operating frequency and piston amplitude were found to have remained essentially constant during those periods. Furthermore, the spacer and hot-end temperatures do not imply that the contact resistance was increasing between the heat flux sensor assembly and convertor heat collector. These data suggest that the expansion space pressure amplitude was decreasing during those periods.

Figure 81 shows the resulting thermal efficiency for both convertors, which are based on a constant alternator power output. The thermal efficiency of ASC-E #4 appears to be slowly increasing throughout the period of successful data collection (8,000 to 10,000 hrs), reaching 35% at the end of the test. The thermal efficiency of ASC-E #1 was

slowly increasing toward 39% until event 3, after which a new trend appeared. Upon every startup after event 3, the new trend started at around 35 % and decreased until the next shutdown event occurred.

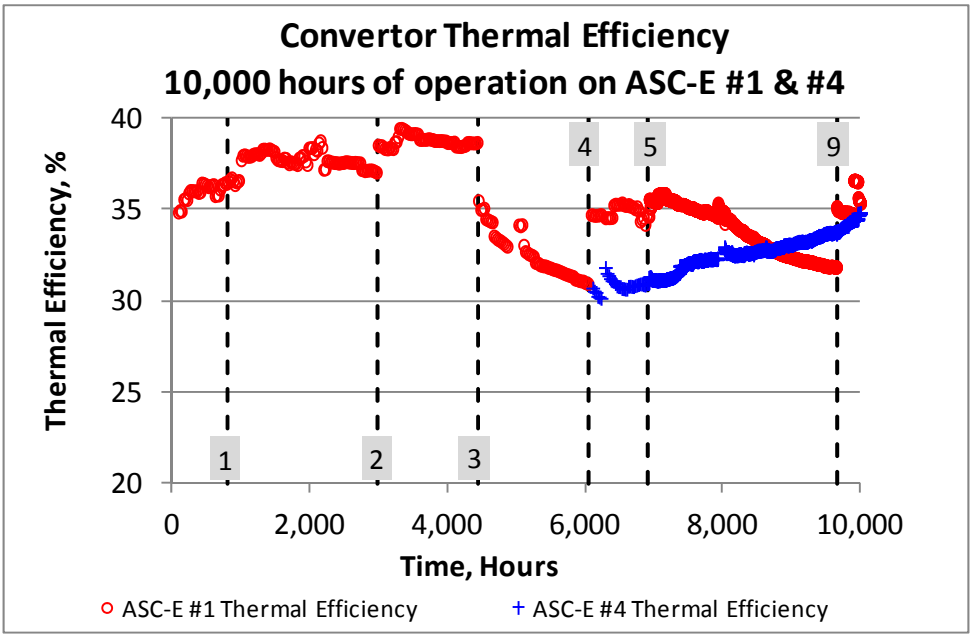

Figure 81. Resulting Thermal Efficiency from ASC-E #1 and #4.

The Sankey diagram, shown in Figure 82, represents an energy balance for ASC-E #1 performed at 9,000 hours of operation. The energy is balanced between the combination of measured, estimated, and calculated values of energy in watts. The Gross Heat Input and Electrical Power Output were both measured using highly accurate voltage and current meters. The Sensor Heat Flow was measured using the heat flux sensor, of which the uncertainty has not yet been quantified. The Indicated Power Output represents the mechanical power available from the Stirling engine. It was calculated by assuming an alternator efficiency of 91% (shown as 7 W loss), which was determined during

alternator characterization testing performed at GRC. The Heat Rejected was calculated by subtracting the Head Insulation Loss, Parasitic Loss, and Indicated Power Output from the Sensor Heat Flow. Parasitic Loss was estimated based on modeling results for this convertor operating under a 625 °C Hot-End Temperature. The Heater Insulation Loss and Head Insulation Loss represent the amount of heat energy lost back to the insulation surrounding the hot surfaces. The Heater Insulation Loss was calculated by taking the difference of the Gross Heat Input and Sensor Heat Flow. All of the values shown are in the range of what could be expected from this convertor design operating at a 625 °C Hot-End Temperature.

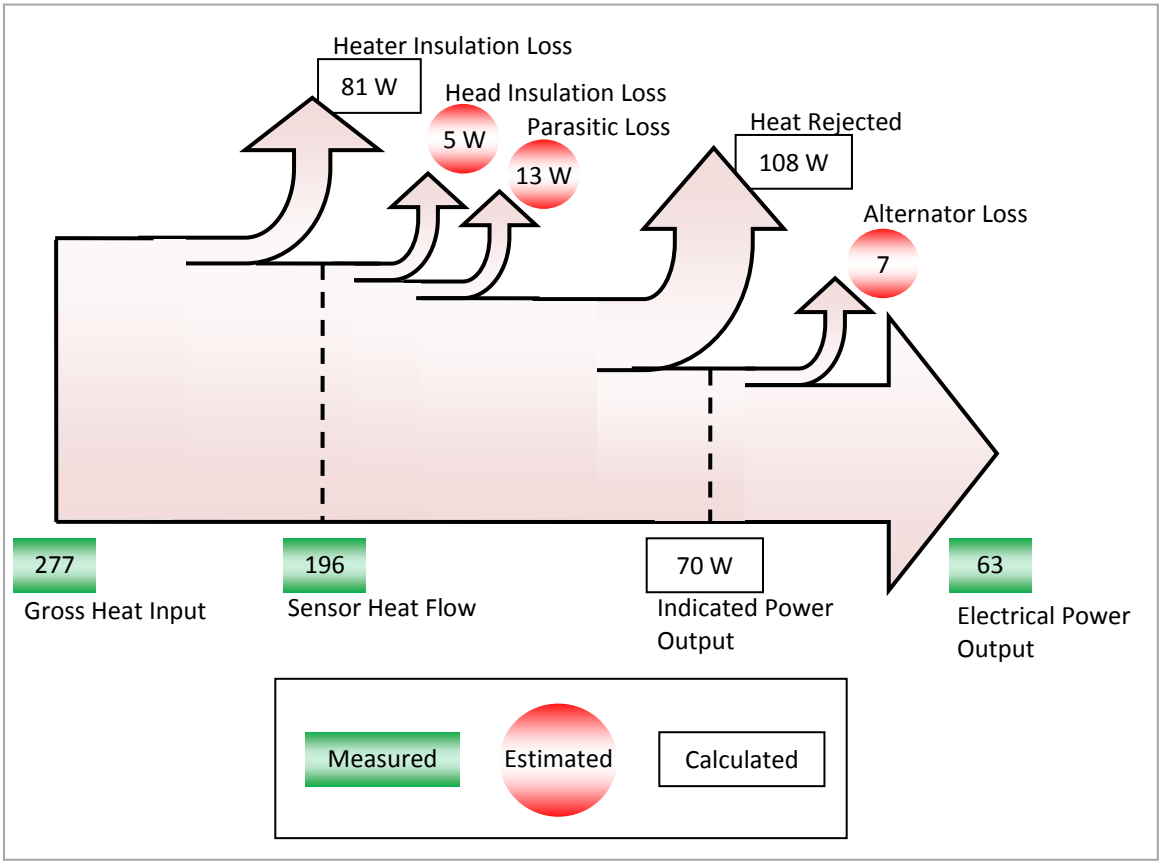

Figure 82. Sankey Diagram of ASC-E #1 Energy Balance Performed at 9,000 hrs.

6.2 Improved Heat Flow Formulation

Formulation of heat flow could also be refined to include weighting for hotter areas that represent a slightly larger area than cooler regions. The current approach used an average heat flow, believed to be a reasonable approach based on the assumption that there would be a relatively small temperature gradient across the face of the sensor. However, the radial temperature variation exceeded the FEA results by 2 times. A better value for heat flow could be acquired by refining the representative value of area for each thermocouple junction to provide an area weighted average temperature used in the heat transfer calculation.

6.3 Improved Sensor Resolution and Uncertainty

The sensor was designed so the resulting temperature difference did not significantly decrease the life of the heater, which is sensitive to the heater operating temperature. The temperature difference across the sensor was designed based on preliminary data for the Alumina thermal conductivity, which turned out to be higher for the sensors used in application. That resulted in a lower axial temperature difference across the ceramic disk which decreased the resolution of the sensor. The limiting case turned out to be the heater head up orientation, which was ASC-E #1. That setup experienced a maximum heater temperature of 760 °C and a corresponding temperature difference from the heater to hot-end of convertor of 135 °C. The average temperature difference across the ceramic disk of 25 °C and average heat flow value of 190 W resulted in a sensor resolution of 0.13 °C/W. The goal of designing a sensor with a higher resolution competes directly with the goal of designing a long life heater. Limiting the heater temperature to 800 °C, believed to be an upper limit for acceptable life, results in an increased sensor resolution of 2.6

times. Future designs should attempt to maximize the resolution which will undoubtedly decrease the measurement uncertainty. Calculation of uncertainty for the heat flow measurement was not included in this effort. To do this, all major contributing error sources would have to be quantified for use in uncertainty calculation.

6.4 Improved Temperature Limit

If heater temperature and life were not part of the design trade space, a higher heater temperature and corresponding temperature difference across the ceramic disk could improve the sensor resolution. This could require the existing sensor to operate at temperatures above the recommended maximum operating temperature of 950 °C. For survival at high temperatures, platinum versus palladium (Pt vs. Pd) thermocouples were suggested by the Sensors and Electronics Branch. The thermocouples are reported to be stable to 1,300 °C in an inert environment.[16] Other tests note exceptional stability for in-air operating temperatures up to 1,500 °C.[17] Also, an improved sensor resolution could be achieved using semi-conductive oxides being developed by NASA as part of the Aviation Safety Program.[18,19] Such sensors have very high outputs (more than double that of Au-Pt), are stable at temperatures around 1,100 °C (for limited time), and are fabricated from oxides, which are inherently stable in hot oxidizing atmospheres.

6.5 Improved Robustness

Several areas of improvement have been indentified that could result in a more robust senor and reduce or eliminate junction failures. The gold film bond strength is an example of degradation observed during normal handling of the sensors before installation. After the sensors were installed and the test was underway, Gus Fralick and John Wrbanek of GRC's Sensors and Electronics Branch performed trials in an effort to

optimize the sputtering process, resulting in improved gold film bond strength. Of eight trials, three passed the scratch test, used as acceptance criteria for film adhesion. These tests resulted in an improved process and gold film bond strength.

Another example of degradation was seen in the protective layer of Alumina present on the sensor and nickel spacers. Less than 1 micron layers of Alumina were sputtered directly onto the finished sensor and nickel spacers to protect the films from chemical reaction (diffusion) with interfacing materials. The post disassembly inspection revealed many films that had either been damaged due to nonuniform surface geometry (nonuniform loading) or diffusion of the thin-films into the interfacing material despite the presence of a protective layer of Alumina. The thickest possible layers were sputtered before flaking becomes a real problem. That said, one improvement that could help protect the thin films near the outer diameter is an increase in the diameter of the protective layer of Alumina. This desire to maximize the protected area competes directly with area of the pad reserved for wire connections but the initial design provided an excess of area for wire connections, which could be decreased. Another, possible more effective, improvement would be to use a thin Alumina disks in place of the nickel disks between the sensor and the heat source and Stirling heat collector. Thin Alumina disks would not add a significant increase in temperature difference and prevents the need for sputtering protective layers of Alumina. Alumina disks would likely need to undergo robustness testing to provide data on selection of the optimum thickness.

6.6 Stirling Heat Addition at NASA Glenn Research Center

After these heat flux sensors was placed into operation, a parallel effort was launched to achieve a more accurate prediction for heat addition to the ASC on test at

GRC. This test and modeling effort included numerous activities, including: making thermophysical property measurements of test setup materials to provide inputs to the numerical models, acquiring additional test data that was collected during convertor tests to provide numerical models with temperature profiles of the test setup via thermocouple and infrared measurements, using multi-dimensional numerical models (computational fluid dynamics code) to predict net heat input of an operating convertor, and using validation test hardware to provide direct comparison of numerical results and validate the multi-dimensional numerical models used to predict convertor heat input and efficiency. The resulting validation hardware test measurement uncertainty was around 2% and the resulting difference between test measurement and numerical model results was also around 2%. This effort produced ASC heat input predictions which were validated using specially designed test hardware and is currently NASA's best known method of predicting heat addition to a Stirling Convertor.

REFERENCES

[1]Schreiber, J. G. "Supporting Technology at GRC to Mitigate Risk as Stirling Power Conversion Transitions to Flight", *Proceedings of the Sixth International Energy Conversion Engineering Conference (IECEC 2008)*, Cleveland, OH, August 2008.

[2]Lewandowski, E.J., et al. "Extended Operation Testing of Stirling Convertors in Support of Stirling Radioisotope Power System Development", *Proceedings of the Sixth International Energy Conversion Engineering Conference (IECEC 2008),* American Institute for Aeronautics and Astronautics, Cleveland, OH, August 2008.

[3]Oriti, S.M. and Cornell, P.A., "Processing and Preparation of Advanced Stirling Convertors for Extended Operation at NASA Glenn Research Center," *Proceedings of the Sixth International Energy Conversion Engineering Conference (IECEC 2008)* American Institute for Aeronautics and Astronautics, Cleveland, OH, August 2008.

[4]Wrbanek, J.D., and Fralick, G.C., "Thin Film Physical Sensor Instrumentation Research and Development at NASA Glenn Research Center", NASA TM-2006-214395, ISA# TP06IIS023, September 2006.

[5]Gardon, R., An Instrument for the Direct Measurement of Intense Thermal Radiation, Review of Scientific Measurements, 24, 5, 1953, pp. 366-370.

[6]Liebert, C. H., "Miniature High Temperature Plug-Type Heat Flux Gages", NASA TM-105403, April 1992.

[7]Will, H., "Fabrication of Thin Film Heat Flux Sensors", Proceedings of the Third Health Monitoring Conference for Space Propulsion Systems, University of Cincinnati Press, pp. 348-355, Cincinnati, OH, 1991.

[8]Cho, C.S., Fralick, G.C., & Bhatt, H. D., “Steady State and Frequency Response of a Thin Film Heat Flux Gauge”, Journal of Spacecraft and Rockets, Vol. 34, No. 6, Nov-Dec 1997.

[9]Fralick, G.C., Wrbanek, J.D., Blaha, C., “Thin Film Heat Flux Sensor of Improved Design,” NASA TM-2002-211566, September 2002.

[10]Wilson, S.D., Fralick, G.C., Wrbanek, J.D., Sayir, A., “Fabrication and Testing of a Thin-Film Heat Flux Sensor for a Stirling Convertor”, NASA/TM—2010-216063, AIAA 2009-4581, January 2010.

[11]Blaha, C.A., “Liftoff Process of Difficult and Non-Etchable Material using Photo-lithography”, NASA Tech Briefs, March 2002.

[12]Holanda, R., Kim, W.S., Pencil, E., Groth, M., and Danzey, G.A., “Attachment of Lead Wires to Thin-Film Thermocouples Mounted on High Temperature Materials Using the Parallel Gap Welding Process”, NASA Technical Memorandum 102442, May 1990.

[13]Bentley, R.E., “Handbook of Temperature Measurement Vol. 3: The Theory and Practice of Thermoelectric Thermometry”, Springer-Verlag Singapore Pte. Ltd. 1998.

[14]Burns, G.W., Strouse, G.F., Liu, B.M., and Magnum, B.W., ”Gold versus Platinum Thermocouple: Performance, Data and an ITS-90 based Reference Function,” NIST, Gaithersburg, MD, In Temperature: Its Measurement and Control in Science and Industry, Ed. by J.F. Schooley, Vol. 6, pp. 531-536, Amer. Institute of Physics, New York, 1992.

[15]Kreider, K.G., Ripple, D.C., and DeWitt, D.P., ”Calibration of Thin-Film Thermocouples on Silicon Wafers” NIST, Gaithersburg, MD, 1998.

[16]Hill, K.D., “An Investigation of Palladium Oxidation in the Platinum-Palladium Thermocouple System”, Metrologia, 2002, 39,51-58.

[17] Burns, G.W., Ripple, D.C., and Battuello, M., “Palladium versus Palladium Thermocouples: An emf-temperature Reference Function for the Range of 0 °C to 1,500 °C”, Metrologia, 1998, 35,761-780.

[18]Gregory, O.J., Busch, E., and Fralick, G.C., “Thermoelectric Properties of Ceramic Thin Film Thermocouples,", ISA# TP06IIS037, May 2006.

[19]Wrbanek, J.D., Fralick, G.C., Farmer, S.C., Sayir, A., Blaha, C.A., and Gonzalez, J.M., “Development of Thin Film Ceramic Thermocouples for High Temperature Environments," NASA TM-2004-213211, AIAA 2004-3549, August 2004.

APPENDIX

Table A-1. Full Dense Alumina Thermal Conductivity Test Results.

Temperature,°C→	30	50	100	200	300	400	500	600	700	800	900	950
	Thermal Conductivity, W/mK											
Mean	28.870	24.768	21.774	16.381	13.616	11.050	9.440	8.748	7.328	6.494	6.108	5.937
Standard Deviation	0.373	1.815	0.052	0.951	0.158	0.409	0.149	0.399	0.141	0.4634	0.156	0.707
Maximum	29.150	27.330	22.520	19.040	13.820	11.670	9.610	9.540	7.540	7.220	6.340	8.110
Minimum	28.310	21.340	21.160	15.280	13.450	10.290	9.310	8.07	7.170	5.660	5.92	5.110

Data Provided by Ali Sayir of GRC's Ceramics Branch.

Table A-2. Robustness Test Results.

TP80-037 Results		Sample Set 1		Sample Set 2		Sample Set 3		Sample Set 4		Sample Set 5		Sample Set 6	
Description		Substitute HFS Ni 201, oxidized		Mullite3-S4 Ni 201 spacers, r1		Alumina2-S5.a spacers:r2, E-beamed Alumina on Ni 201		Alumina2-S5.b **spacers: r2 Alumina2**-S10, S7		Alumina2-S4 **silica arm** spacers:r2, E-beamed Alumina on Ni 201		Alumina2-S6 Au/Pt films, wires spacers:r2, E-beamed Alumina on Ni 201	
Test Date	units	13-Jan-09		17-Jan-09		23-Jan-09		24-Jan-09		28-Jan-09		29-Jan-09	
Mechanical Load	lbs		399		399		340		322		401		305
		ave	max	ave	max	ave	max	ave	max	ave	max	ave	max
Heater Temperature	°C	716	731	752	772	807	821	841	872	653	685	868	884
Heater Spacer Temperature	°C	677	689	677	685	730	736	717	734	584	601	787	794
Collector Spacer Temperature	°C	665	676	565	567	651	655	626	640	523	536	660	665
Collector Temperature	°C	**588**	596	514	516	**623**	627	**578**	590	**499**	512	**622**	627
ΔT (spacers)	°C	**12**	13	112	118	**79**	81	**91**	94	**61**	65	**127**	129
ΔT (heater - collector)	°C	**128**	135	238	256	**184**	194	**263**	282	**154**	173	**246**	257
Input Power	watts	345	460	345	501	**387**	502	369	503	**300**	503	**393**	507
Calculations	units	ave	max	ave	max	ave	max	ave	max	ave	max	ave	max
input power ratio	--	1.01		1.01		0.90		0.95		1.17		0.89	
scaled heater temperature	°C	726		763		730		798		762		773	
scaled ΔT (heater - hot-end)	°C	**66**		**103**		**70**		**138**		**102**		**113**	

**scaled heater temperature = (measured Heater Temp * Input Power Ratio) , scaled ΔT (heater - collector) = (scaled heater temperature - expected collector temp)*

Table A-3. Coefficients and function: Au-Pt (0 °C to 1,000 °C)[14].

Purpose: Convert temperature (°C) to emf (microvolt)		
Exponent	Coefficient	Equation
1	6.036199E+00	$E = p(t_{90}) = \sum_{i=1}^{9} p(t_{90})^i$
2	1.936730E-02	
3	-2.229986E-05	
4	3.287119E-08	
5	-4.242062E-11	
6	4.569270E-14	
7	-3.394303E-17	
8	1.429816E-20	
9	-2.516787E-24	

Table A-4. Coefficients and function: Au-Pt (0 °C to 209 °C) [14].

Purpose: Convert emf (microvolt) to temperature (°C)		
Exponent	Coefficient	Equation
1	1.654390E-01	$p(t_{90}) = \sum_{i=1}^{8} b_i(E)^i$
2	-8.409884E-05	
3	8.416613E-08	
4	-7.517469E-11	
5	4.849554E-14	
6	-2.013876E-17	
7	4.747563E-21	
8	-4.797308E-25	

Table A-5. Coefficients and function: Au-Pt (209 °C to 1,000 °C) [14].

Purpose: Convert emf (microvolt) to temperature (°C)		
Exponent	Coefficient	Equation
0	6.763360E+02	$t_{90} = \sum_{i=0}^{11} b_i\left((E - 9645)/7620\right)^i$
1	3.735504E+02	
2	-5.537363E+01	
3	1.701900E+01	
4	-6.098761E+00	
5	2.457162E+00	
6	-3.385575E+00	
7	3.853735E+00	
8	1.178891E+00	
9	-2.702558E+00	
10	-1.686158E+00	
11	1.876968E+00	

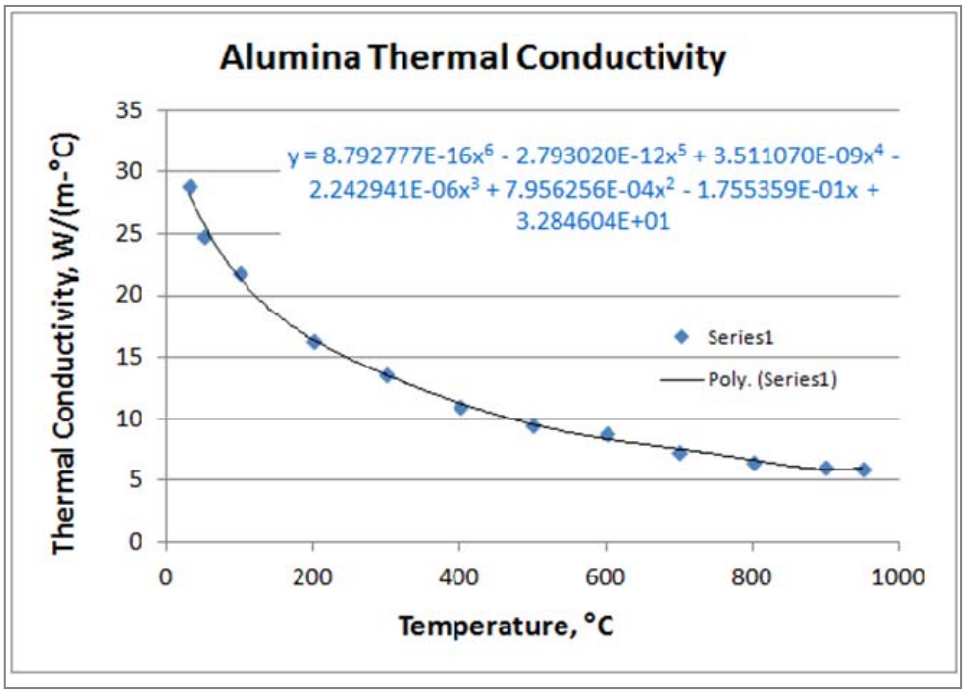

Figure A-1. Curve Fit for Alumina Thermal Conductivity (mean values in Table A-1).

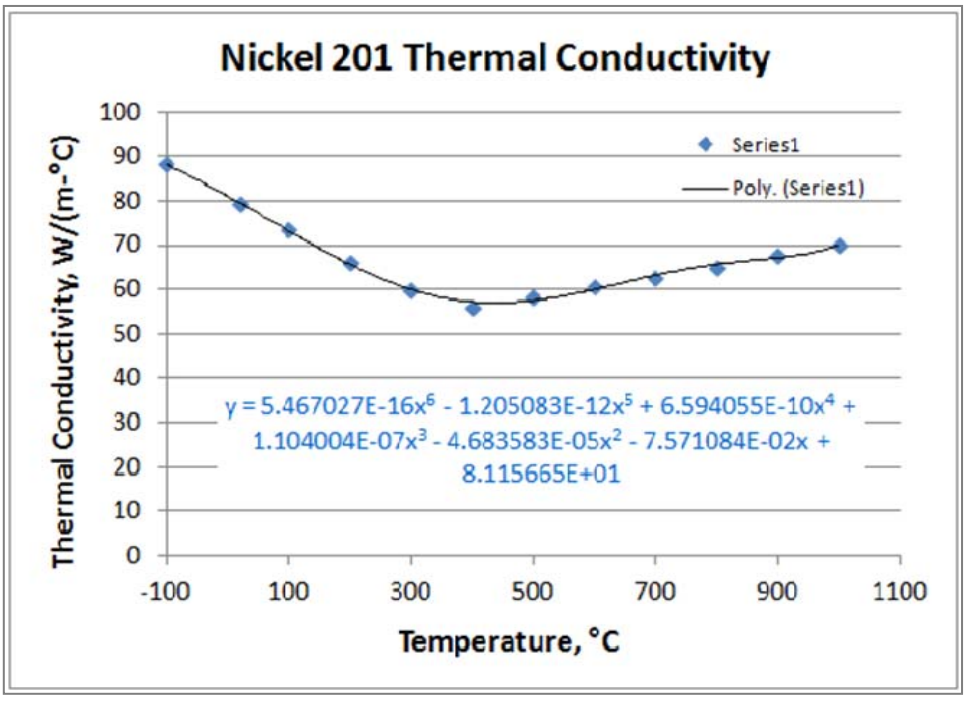

Figure A-2. Curve fit for Nickel 201 Thermal Conductivity.

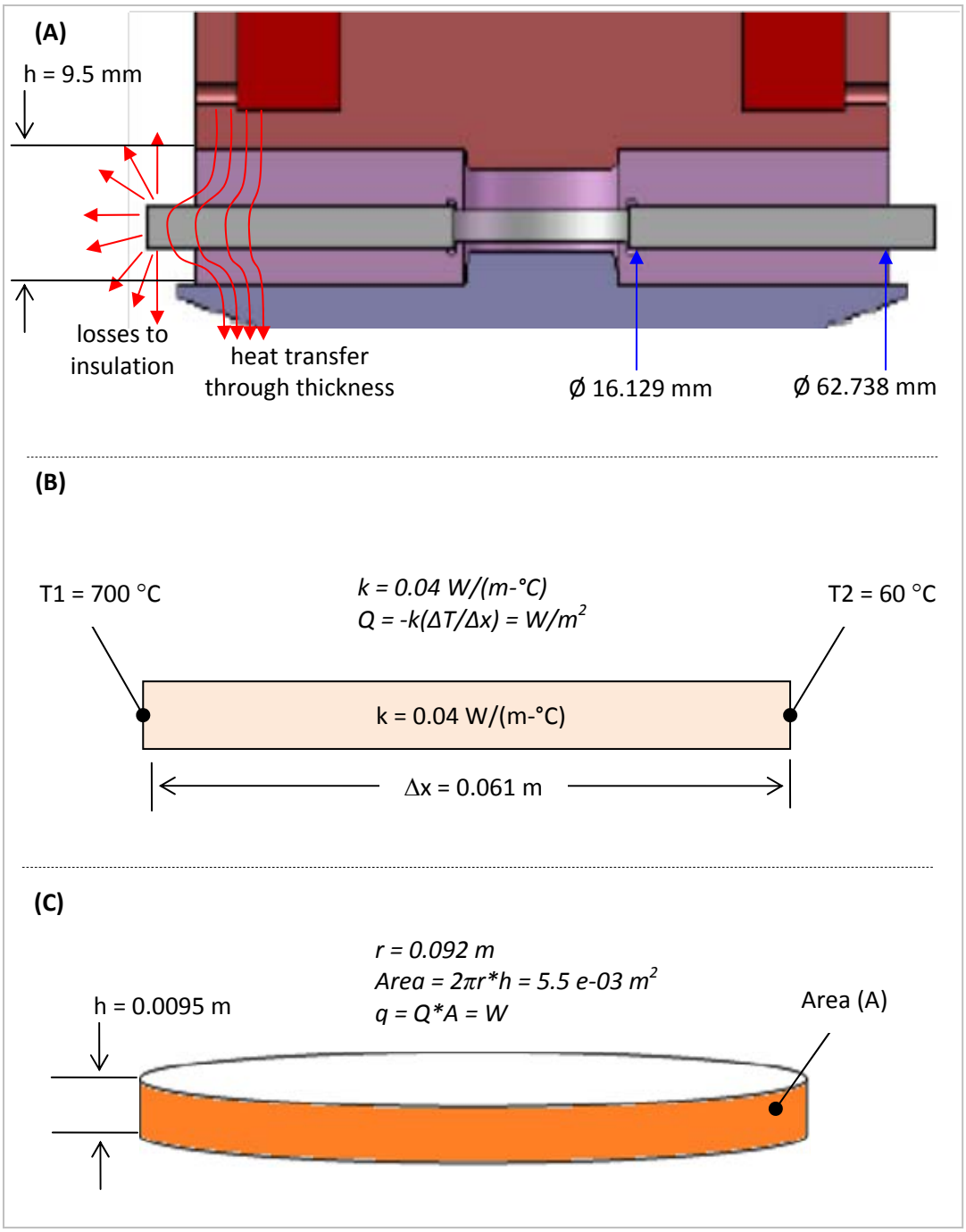

Figure A-3. Assembly Heat Transfer Paths & Estimated Heat Losses.

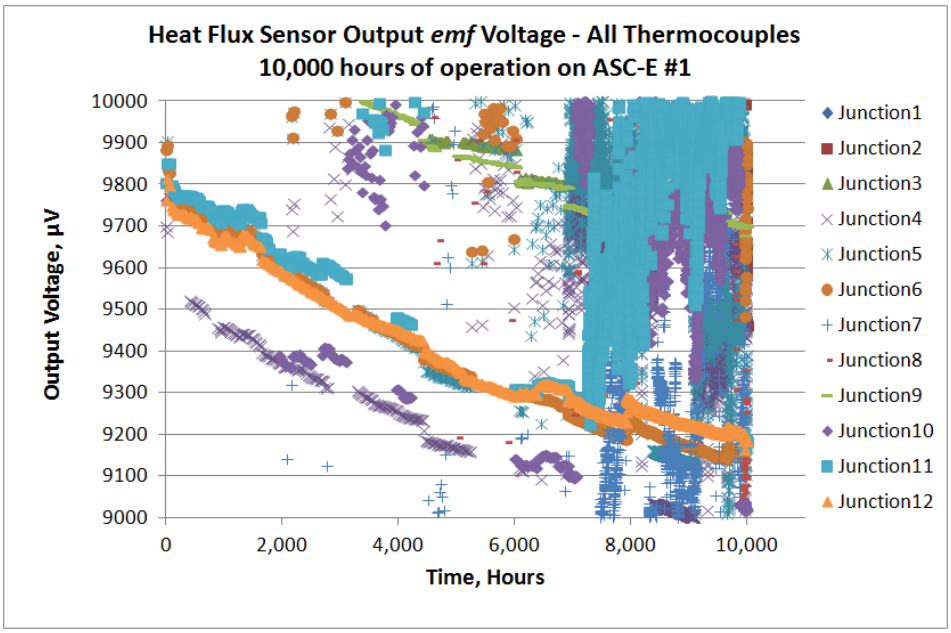

Figure A-4. ASC-E #1's Sensor Output Voltage, All Junctions, 0-10,000 hr.

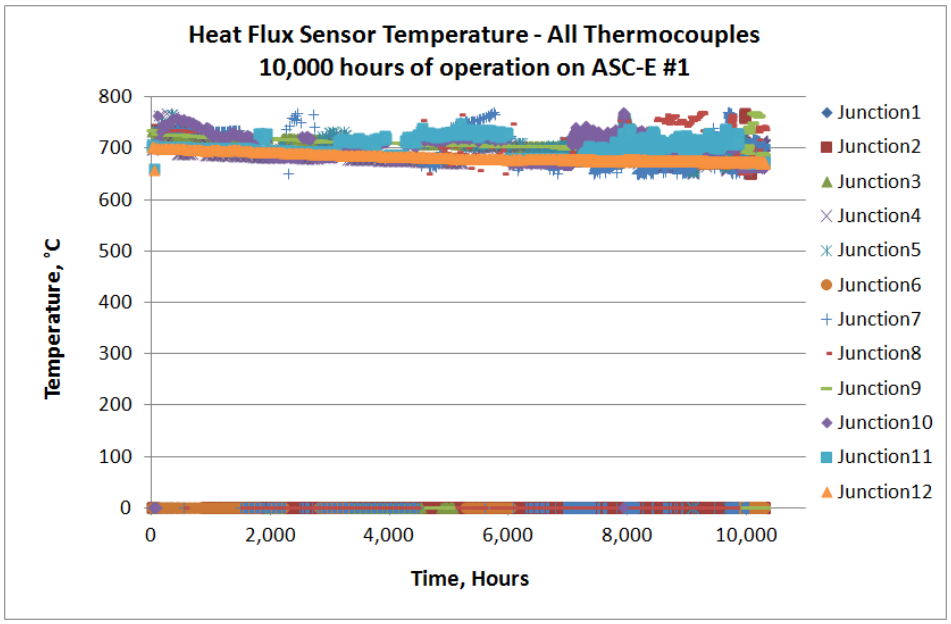

Figure A-5. ASC-E #1's Sensor Temperatures, All Junctions, 0-10,000 hr.

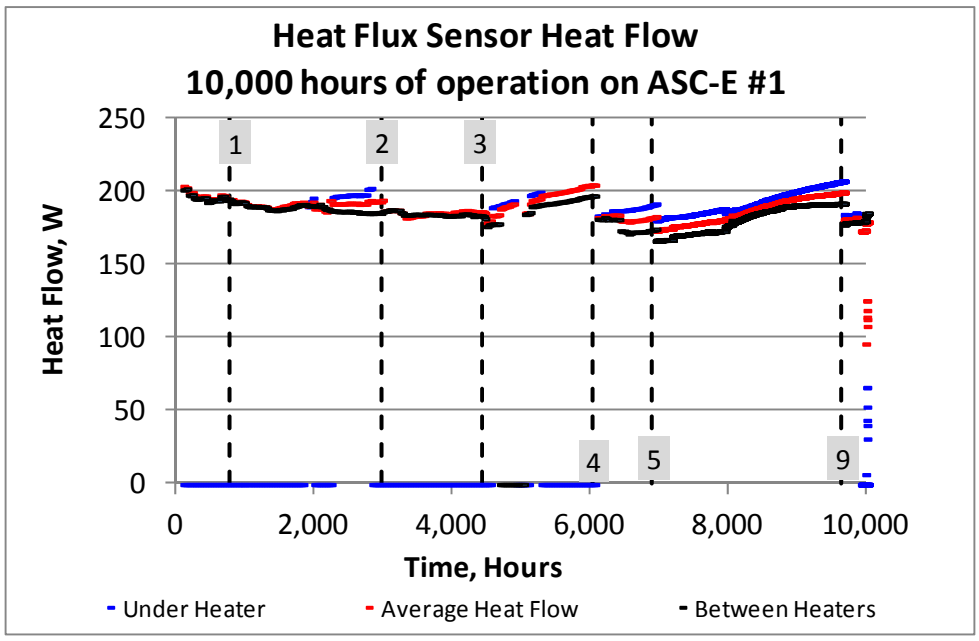

Figure A-6. ASC-E #1's Sensor Heat Flow, 0-10,000 hr.

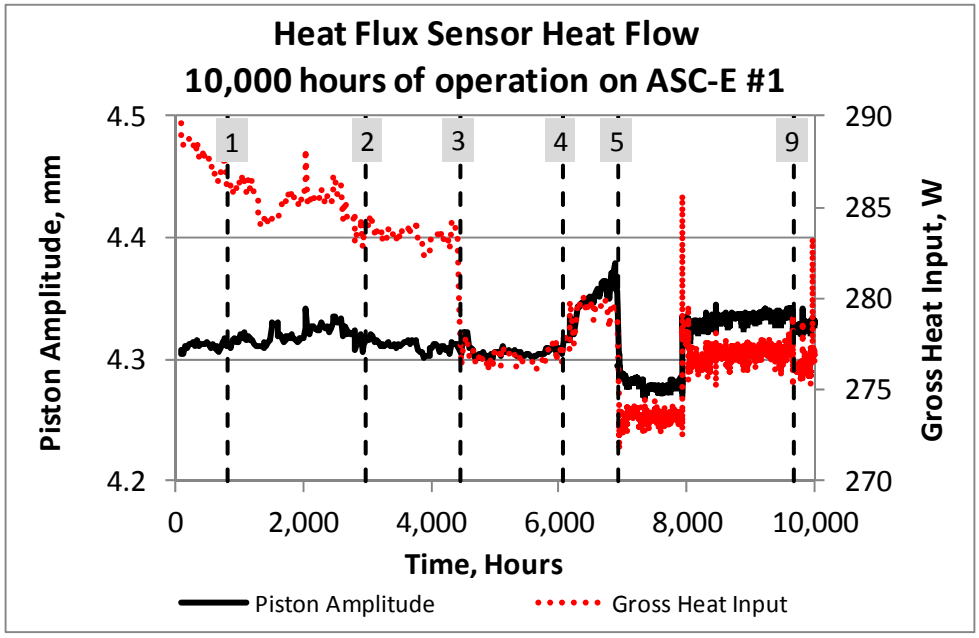

Figure A-7. ASC-E #1's Piston Amplitude & Gross Heat Input, 0-10,000 hr.

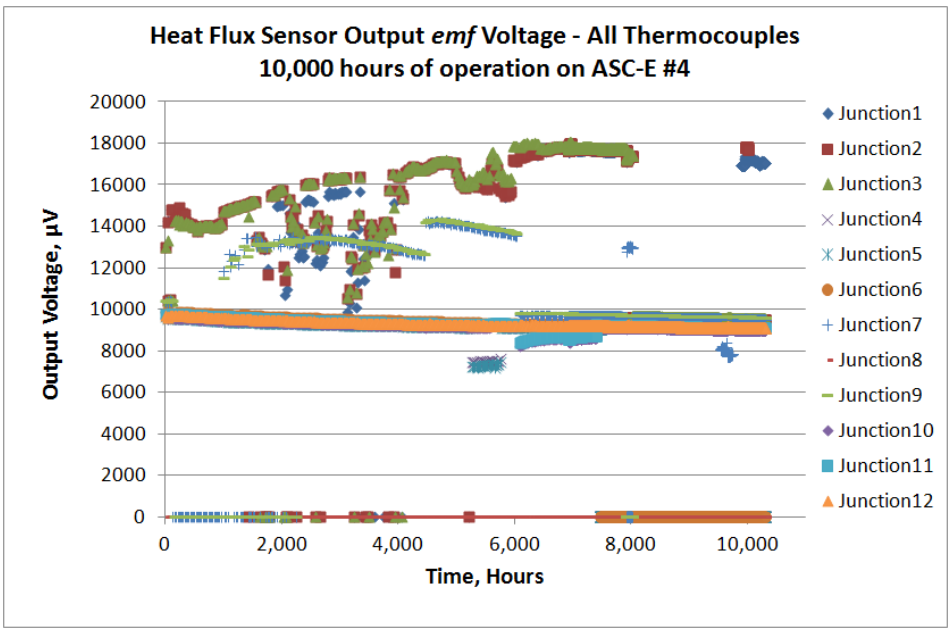

Figure A-8. ASC-E #4's Sensor Output Voltage, All Junctions, 0-10,000 hr.

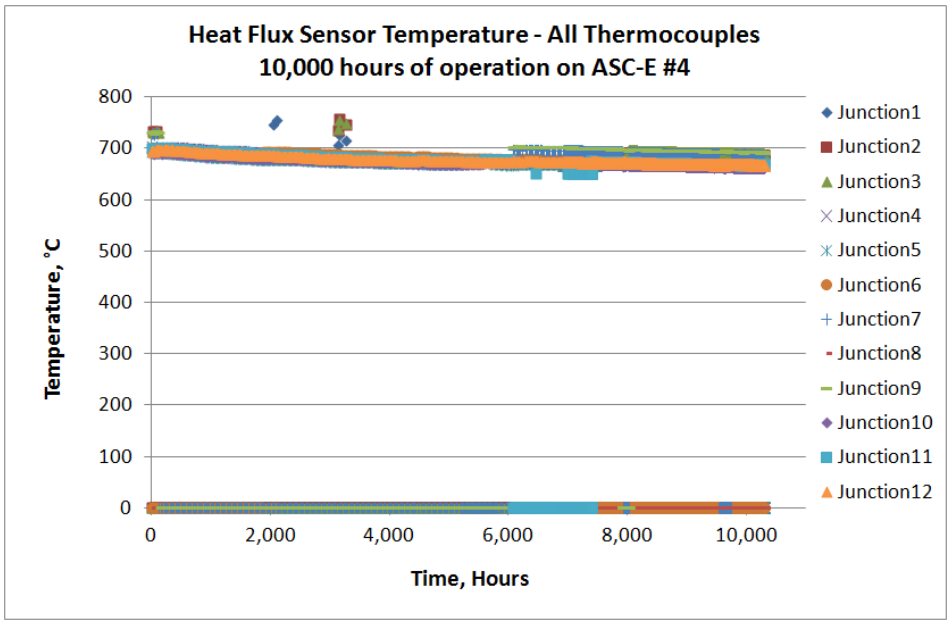

Figure A-9. ASC-E #4's Sensor Temperatures, All Junctions, 0-10,000 hr.

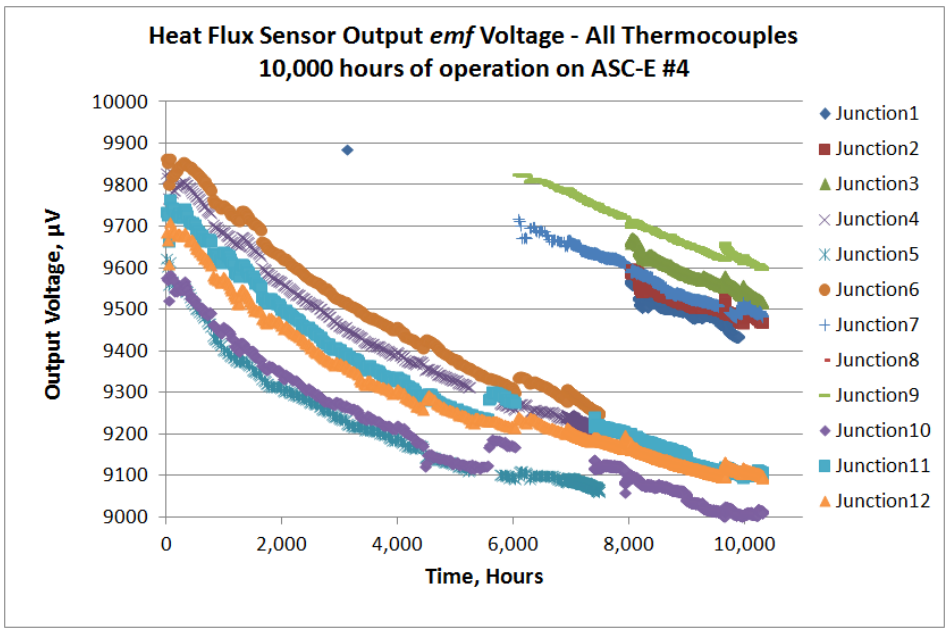

Figure A-10. ASC-E #4's Sensor Output Voltage, All Junctions, 0-10,000 hr.

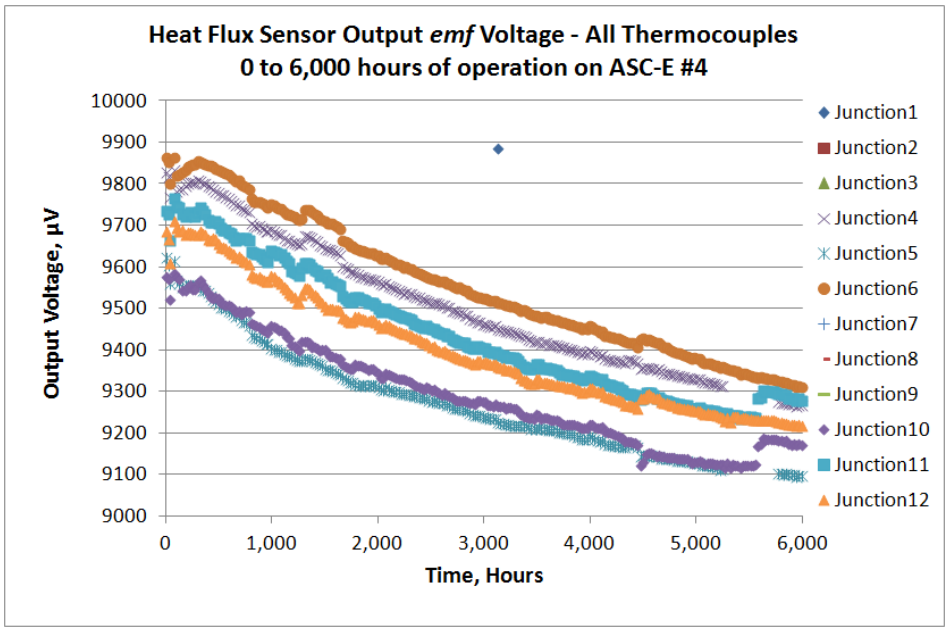

Figure A-11. ASC-E #4's Sensor Output Voltage, All Junctions, 0-6,000 hr.

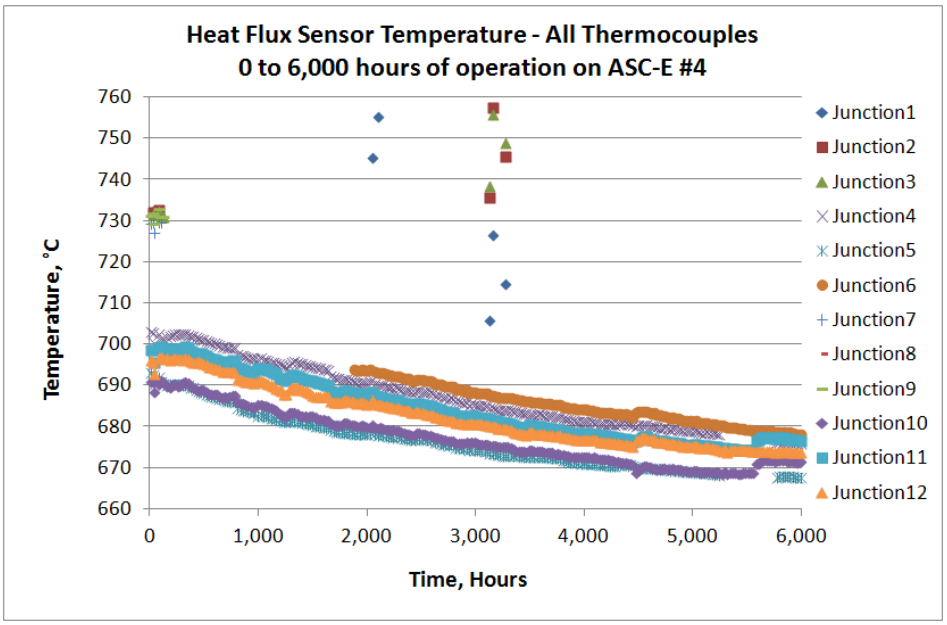

Figure A-12. ASC-E #4's Sensor Temperatures, All Junctions, 0-6,000 hr.

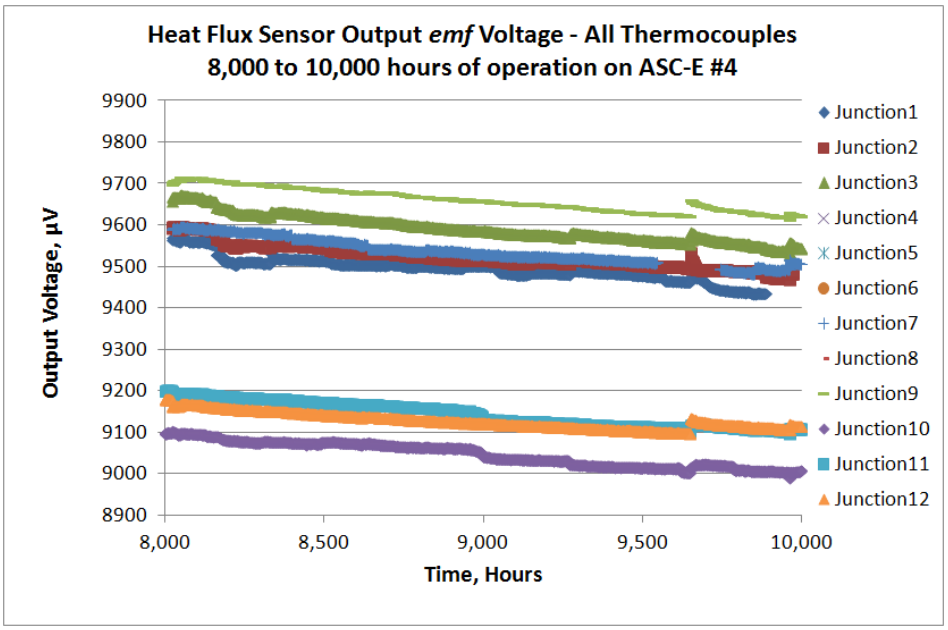

Figure A-13. ASC-E #4's Sensor Output Voltage, All Junctions, 8,000-10,000 hr.

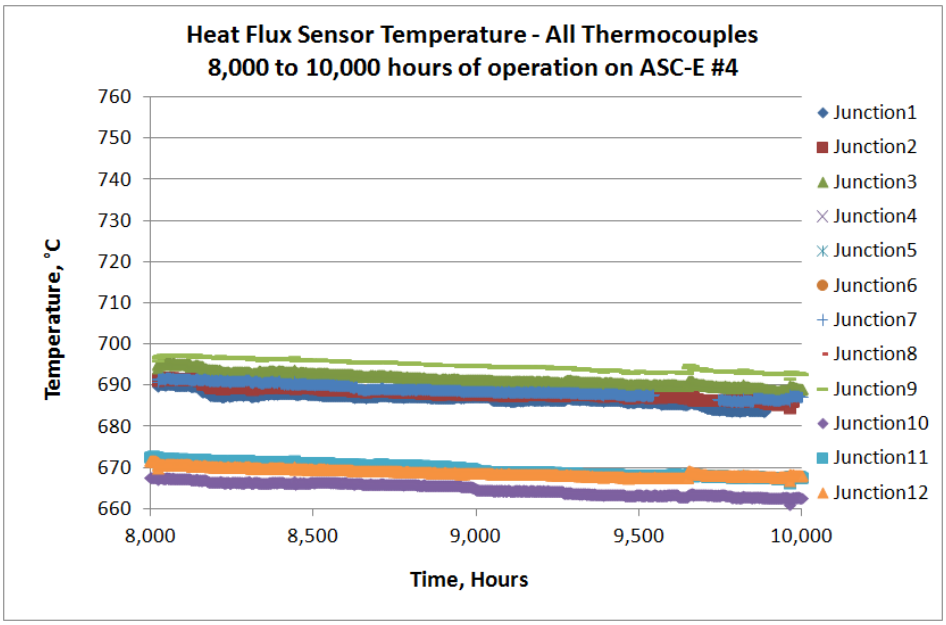

Figure A-14. ASC-E #4's Sensor Temperatures, All Junctions, 8,000-10,000 hr.

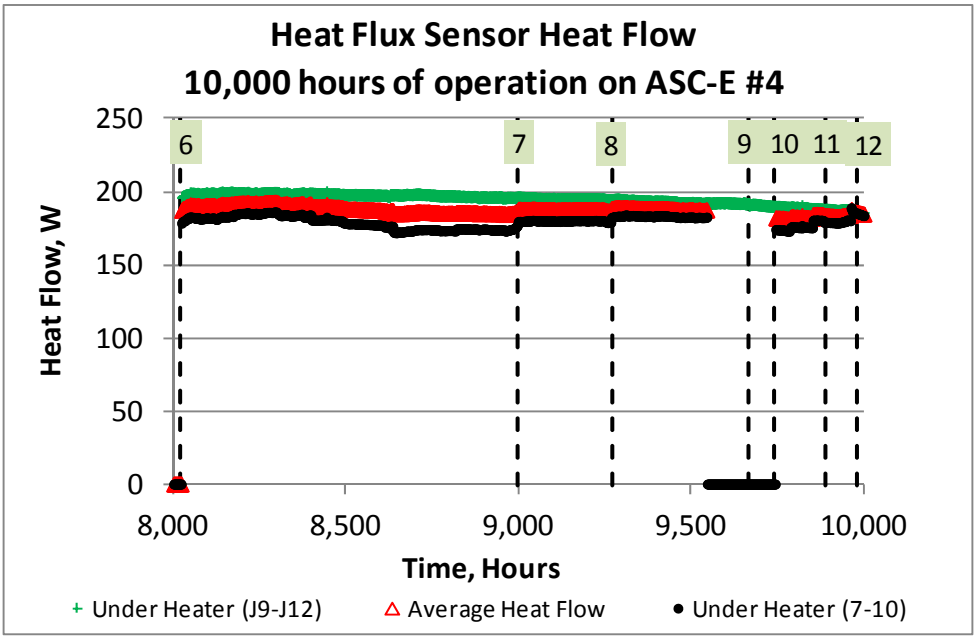

Figure A-15. ASC-E #4's Sensor Heat Flow, 8,000-10,000 hr.

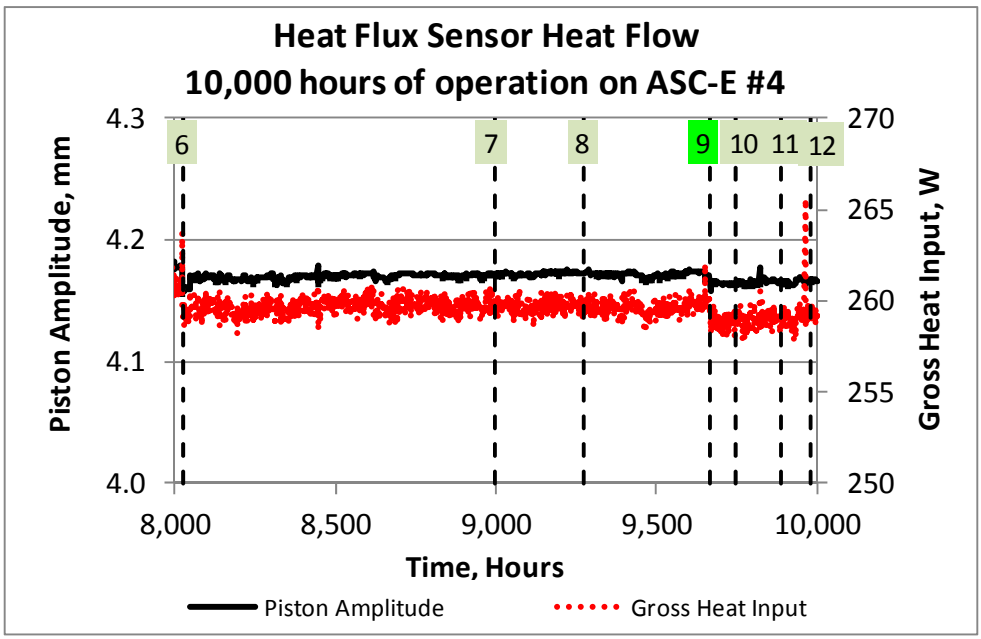

Figure A-16. ASC-E #4's Piston Amplitude & Gross Heat Input, 0-10,000 hr.